

**NASA Contractor Report 178409**

## **Composite Transport Wing Technology Development**

**Dr. Ram C. Madan**

Douglas Aircraft Company  
McDonnell Douglas Corporation  
Long Beach, CA 90846

**Contract NAS1-17970  
February 1988**

(NASA-CR-178409) COMPOSITE TRANSPORT WING  
TECHNOLOGY DEVELOPMENT (Douglas Aircraft  
Co.) 92 p CSCL 01C

**N89-26842**

**Unclas  
G3/05 0222714**



National Aeronautics and  
Space Administration

**Langley Research Center**  
Hampton, Virginia 23665

**NASA Contractor Report 178409**

## **Composite Transport Wing Technology Development**

**Dr. Ram C. Madan**

Douglas Aircraft Company  
McDonnell Douglas Corporation  
Long Beach, CA 90846

**Contract NAS1-17970  
February 1988**



National Aeronautics and  
Space Administration

**Langley Research Center**  
Hampton, Virginia 23665

## **ABSTRACT**

This report deals with design, fabrication, testing, and analysis of stiffened wing cover panels to assess damage tolerance criteria. The damage tolerance improvements were demonstrated in a test program using full-sized cover panel subcomponents. The panels utilized a "hard" skin concept with identical laminates of 44-percent 0-degree, 44-percent  $\pm 45$ -degree, and 12-percent 90-degree plies in the skins and stiffeners. The panel skins were impacted at midbay between the stiffeners, directly over the stiffener, and over the stiffener flange edge. The stiffener blades were impacted laterally. Impact energy levels of 100 ft-lb and 200 ft-lb were used. NASTRAN finite-element analyses were performed to simulate the nonvisible damage that was detected in the panels by nondestructive inspection. A closed-form solution for generalized loading was developed to evaluate the peel stresses in the bonded structure. Two-dimensional delamination growth analysis was developed using the principle of minimum potential energy in terms of closed-form solution for critical strain. An analysis was conducted to determine the residual compressive stress in the panels after impact damage, and the analytical predictions were verified by compression testing of the damaged panels.

**PRECEDING PAGE BLANK NOT FILMED**

## **FOREWORD**

This final report was prepared by Douglas Aircraft Company of the McDonnell Douglas Corporation, at Long Beach, California, under NASA Contract NAS1-17970. It covers work performed between July 1985 and May 1987. The program was sponsored by the National Aeronautics and Space Administration, Langley Research Center (NASA-LRC), Hampton, Virginia. Dr. Mark Shuart and Dr. J. G. Davis, Jr., were the NASA-LRC technical representatives for this project.

Uses of commercial products or names of manufacturers in this report do not constitute official endorsement of such products or manufacturers, either expressed or implied, by the National Aeronautics and Space Administration.

This report was prepared by the project manager, Dr. Ram C. Madan of Douglas Aircraft Company. The following Douglas personnel were principal contributors to the program:

### **Program and Technical Management**

Dr. H. C. Schjelderup  
M. Klotzsche

### **Project Manager**

Dr. R. C. Madan  
B. L. Bunin\*

### **Business Management**

T. E. Alvarado-Lee  
M. E. Eike

### **Stress Analysis**

J. O. Sutton  
K. A. Walker  
B. A. Hanson

### **Structural Design and Analysis**

Dr. R. C. Madan  
J. O. Sutton  
D. A. Barkey  
R. E. Sagui

### **Materials and Process Engineering**

M. F. Murphy

### **Structural Testing and Coordination**

M. F. Murphy  
Dr. R. C. Madan  
J. O. Sutton  
E. L. Hayman

### **Technical Advisors**

J. O. Sutton  
M. Ashizawa  
A. V. Hawley  
J. Genicki

\*Initially headed project.

PRECEDING PAGE BLANK NOT FILMED



# CONTENTS

Section	Page
1 INTRODUCTION .....	1
2 BASELINE WING DESIGN .....	3
2.1 Material Selection .....	3
2.2 Conceptual Design .....	7
3 TEST SPECIMENS AND PROCEDURES .....	13
3.1 Specimen Description .....	13
3.2 Specimen Fabrication .....	19
3.2.1 Stringer Fabrication .....	19
3.2.2 Skin Fabrication .....	20
3.2.3 Skin-Stringer Assembly .....	20
3.2.4 Demonstration Panels .....	21
3.3 Test Procedures .....	22
3.3.1 Ancillary Tests .....	22
3.3.2 Development Tests .....	24
3.3.3 Test Plan for Demonstration Panels .....	30
4 ANALYTICAL DEVELOPMENT .....	31
4.1 NASTRAN Model .....	31
4.1.1 Analysis .....	32
4.1.2 Refined Analysis .....	33
4.1.3 Specimen and Support Conditions .....	36
4.2 Delamination Growth — An Approximate Solution .....	36
4.3 Peel Stress Analysis .....	43
4.3.1 Analysis .....	43
4.3.2 Results .....	48
4.4 Residual Strength Analysis .....	52
4.4.1 Effect of a Finite-Width Panel .....	55
4.4.2 Stress Concentration Factor .....	55
4.4.3 Residual Strength .....	56
4.4.4 Analysis Method .....	57
5 TEST RESULTS AND DISCUSSION .....	59
5.1 Ancillary Tests .....	59
5.1.1 Tension and Compression Tests .....	59
5.1.2 Open-Hole Compression Tests .....	59
5.1.3 Compression-Bearing Tests .....	60
5.1.4 One-Dimensional Delamination Tests .....	60
5.1.5 Two-Dimensional Delamination Tests .....	61
5.1.6 Edge Delamination Test .....	62
5.1.7 Hinged Double Cantilever Beam Test .....	62
5.1.8 Compression-After-Impact Test .....	62
5.2 Development Test Specimens .....	65
5.2.1 Experimental Results .....	65
5.2.2 Predicted Strengths .....	72
5.3 Demonstration Panels .....	75
6 CONCLUSIONS .....	79
ACKNOWLEDGMENT .....	81
REFERENCES .....	81

## ILLUSTRATIONS

Figure	Page
1 D-3304-2 Baseline Aircraft .....	1
2 Baseline Wing Structural Arrangement .....	2
3 NASA ST-1 Tests — Residual Strength (Room Temperature, Dry) .....	4
4 NASA ST-1 Tests — Impact Damage Size (Room Temperature, Dry) .....	5
5 Damage After Impact (20-ft-lb Drop) for Composite Wing Material Selection .....	5
6 Wing Box Shear Stiffness Requirement .....	7
7 Wing Box Extensional Stiffness Requirement .....	8
8 Shear Stiffness Distribution .....	8
9 Extensional Stiffness Distribution .....	9
10 Extensional Stiffness Distribution in Skin and Stringers (7-inch Pitch) .....	9
11 Composite Wing Cover Panel Concept .....	11
12 Modified Concept for Blade Stringers .....	12
13 Typical Curing Cycle for Wing Skin and Stringer .....	13
14 Tension and Compression Bearing Test Specimen .....	16
15 Compression-Delamination Specimens .....	16
16 Peel (a) and Pull-Off (b) Specimen Configurations .....	17
17 Trial Impact Specimens .....	18
18 Damage Screening and Damage Tolerance Compression Panels .....	18
19 Stringer Tooling Concept .....	20
20 NDI of Panel D2 After Impact (Visible Damage — 100-ft-lb, 1/4-in. Impactor) .....	21
21 Demonstration Panel (Five-Stringer Panel) .....	22
22 One-Dimensional Delamination Coupon Test Setup .....	23
23 Unnotched Compression Test Setup .....	24
24 Support Conditions for Impact Tests .....	25
25 Impact Panel Configurations and Impact Locations .....	25
26 Strain Gage and Impact Locations on Panels .....	29
27 Compression Test Setup .....	30
28 Typical NASTRAN Model of Impact Panels .....	31
29 NASTRAN Model Analysis for Flange Edge Impact (100 ft-lb) .....	32
30 Comparison of Interlaminar Stresses in Thin (18-Ply) and Thick (36-Ply) Flange Blade Panels .....	34
31 Peel Moment Versus Pull-Off Load Failure Envelope for Delaminations in Skin at Stringer Interface .....	35
32 NASTRAN Model with Adhesive Layer .....	35
33 Interlaminar Tensile Stress Contours Derived from Refined NASTRAN Model .....	36
34 Elliptical Delamination Geometry .....	37
35 Variation of $G_a$ and $G_b$ with $a$ and $b$ .....	39
36 Sensitivity of $G_b$ to Material Property $G_{1c}$ .....	40
37 Sensitivity of Critical Delamination Growth Strain to the Material Property $G_{1c}$ .....	41
38 Sensitivity of Parameter $G_b$ to the Depth of the Delamination Plane .....	42
39 Model Used for Analysis .....	43
40 Peel Stress Distribution .....	49
41 Shear Stress in Adhesive Layer .....	49
42 Axial Stress in Skin (Upper Plate) .....	50
43 Out-of-Plane Deflection of Skin (Upper Plate) .....	50
44 Axial Displacement of Skin (Upper Plate) .....	51
45 Axial Displacement of Flange (Lower Plate) .....	51
46 Axial Stress in Flange (Lower Plate) .....	52

## ILLUSTRATIONS (Continued)

Figure	Page
47 Axial Stress Distribution for a Plate with a Hole and Characteristic Length, $d_o$ (Point Stress Criterion) .....	53
48 Critical Stress Intensity Factor and Inherent Flaw Size, $c_o$ , for Different Laminates ...	54
49 Residual Stress Distribution Versus Damage Size for Various Values of $d_o$ (Point Stress Criteria) at $K_T = 3.5$ .....	56
50 Stress Distribution for Stiffened Panel .....	57
51 1808I/IM6 Fracture Toughness .....	63
52 Three-Stringer Panel B1 After Compression Test (Midbay Impact) .....	68
53 Three-Stringer Panel C1 After Compression Test (Midbay 200 ft-lb, 1/4-Inch Impactor) .....	69
54 Compression-After-Impact Test — Three-Stringer Panels C1 and C1' .....	74
55 Five-Stringer Panel 5D-1 Compression-After-Impact Test .....	76

## TABLES

Table	Page
1 Materials Selection .....	4
2 Quality Control Test Data .....	6
3 Average Laminate Per Ply Thickness .....	6
4 Selection Criteria for Compression Panel Configuration .....	10
5 Composite Wing Technology Ancillary Tests .....	14
6 Composite Wing Technology Development Tests .....	15
7 Composite Wing Technology Demonstration Tests .....	15
8 Stiffened Panels .....	19
9 100-ft-lb Impact Tests and Results for Two-Stringer Panels .....	27
10 100-ft-lb Impact Tests and Results for B-Type Three-Stringer Panels .....	27
11 100-ft-lb Impact Tests and Results for C-Type Three-Stringer Panels .....	28
12 Tension and Compression Test Results .....	59
13 Open-Hole Compression Test Results .....	60
14 Compression Bearing Test Results .....	60
15 One-Dimensional Compression Delamination Test Results .....	61
16 Two-Dimensional Compression Delamination Test Results .....	62
17 ST-2 Edge Delamination Tension Test Data .....	63
18 ST-5 Hinged Double Cantilever Beam Test Data .....	64
19 Compression After Impact Test Data .....	64
20 Strain Gage Readings for Panel B1 .....	65
21 Strain Gage Readings for Panel B2 .....	66
22 Strain Gage Readings for Panel C1' .....	66
23 Strain Gage Readings for Panel C2 .....	67
24 Strain Gage Readings for Panel C3 .....	67
25 Strain Gage Readings for Panel C4 .....	68
26 Summary of Compression-After-Impact Test for Three-Stringer Panels .....	70
27 Residual Strength Analysis .....	78

## NOMENCLATURE

$a, b$	Semixaxis lengths of a delaminated idealized ellipse
$A_{di}$	Impact damage area detected by C-scan
$A_{ij}$	A, in-plane stress matrix; refer to delaminated plies
$A, B, D$	S-matrix of delamination
$B_{ij}$	B, coupling matrix; refer to delaminated plies
$C_{exp}$	Ratio of residual strengths of unstiffened and stiffened panel
$C_1'$	Constant represented by Equation 1
$c$	Half length of a notch
$c_o, d_o$	Characteristic zone length for inherent flaw and point stress criteria
$D_{ij}$	D, bending matrix; refer to delaminated plies where $i = j = 1, 2, 6$ for matrices A, B, and D
$D_1, D_2$	Bending rigidity of skin and stringer flange
$E$	Young's modulus of the original laminate
$EA$	Membrane stiffness
$E_c$	Young's modulus of adhesive layer
$E_1, E_2$	Young modulus of skin and stringers, respectively
$f_i$	Functions of matrices A, B, D, a, b, and $\nu$
$F_{cy}$	Yield strength of material in compression
$G_a$	Strain energy release rate with respect to $a$ when $b$ is constant
$G_b$	Strain energy release rate with respect to $b$ when $a$ is constant
$G_c$	Strain energy release rate
$G_{Ic}$	Strain energy release rate, Mode I
$K_c$	Critical stress intensity factor
$K_x, K_y, K_{xy}$	Bending curvatures
$K_Q$	Stress intensity factor
$K_T, K_T^\infty$	Stress concentration factor for finite and infinite width, respectively
$N_x$	Applied force per unit width in x direction
$P, M, F$	Applied shear force, bending moment, and axial force
$R$	Radius of a circular hole in a specimen
$S$	Total surface area including delaminated region

$t$	Thickness of laminate before any damage
$t_c$	Thickness of adhesive layer
$t_d$	Thickness of delaminated sublaminates
$t_1$	Skin thickness
$t_2$	Stringer flange thickness
$t_p$	Ply thickness
$T_1, T_2$	$(t_1 + t_c)/D_1, (t_2 + t_c)/D_2$
$u_1$	Axial displacement of skin
$u_2$	Axial displacement of stringer
$U$	Total strain energy of the region
$u, v, w$	Displacement components in x, y, and z directions, respectively
$w$	Width of the laminate or panel
$x, y, z$	Rectilinear coordinate axes
$Y$	Finite-width factor
$\alpha$	a/b aspect ratio
$\gamma_c$	Shear strain in adhesive layers
$\epsilon_c$	Failure strain
$\epsilon_{cr}$	Compressive strain before or after impact at failure
$\epsilon_{ox}$	Applied strain in x-direction
$\epsilon_{xcr}$	Critical compressive strain at onset of delamination
$\epsilon_x, \epsilon_y, \gamma_{xy}$	In-plane strain components
$\nu$	Poisson's ratio of the parent laminate
$\pi$	Total potential energy
$\sigma_{cr}$	Compressive stress before or after impact at failure
$\sigma_{cs}$	Compressive residual strength of stiffened panel
$\sigma_o, \sigma_N$	Ultimate strength of unnotched and notched specimen
$\tau_c$	Shear stress in adhesive
Subscripts 1, 2, c	Skin, stringer flange, and adhesive layer, respectively

## SECTION 1

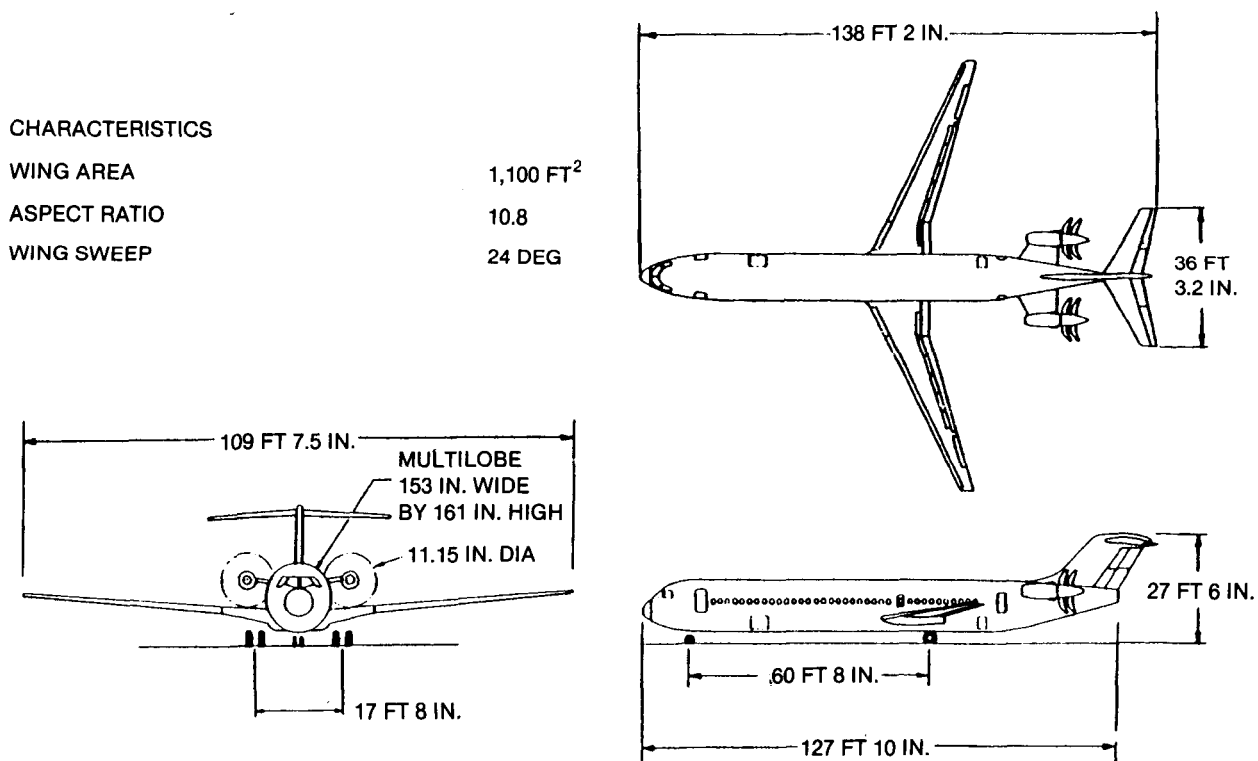
### INTRODUCTION

NASA programs have provided the aircraft manufacturer, the FAA, and the airlines with the experience and confidence needed for extensive use of composites in secondary and medium-primary structure in future aircraft. Secondary and control-surface structures made of composites are already in airline service on production aircraft, and composite medium-primary structures have been introduced for flight service evaluation.

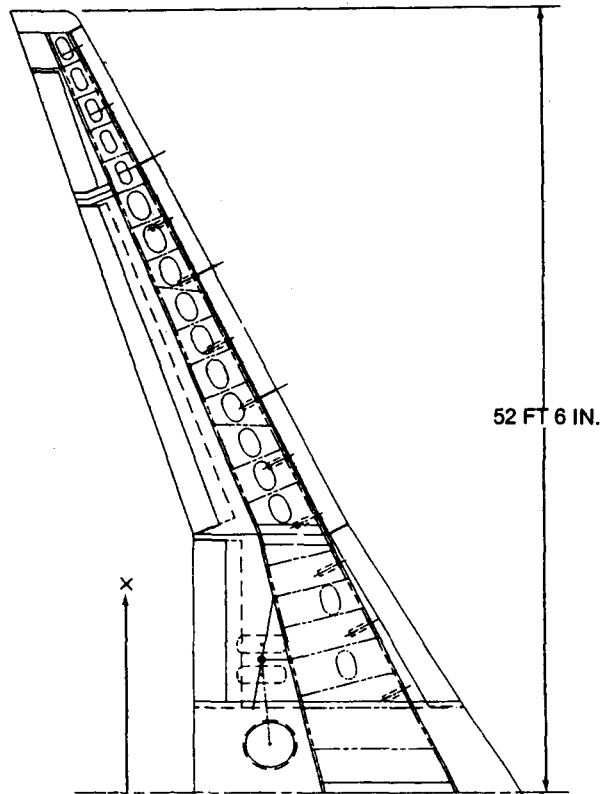
While these applications have produced worthwhile weight savings, the use of composite materials in wing and fuselage primary structures offers a far greater opportunity for saving weight since these structures comprise approximately 75 percent of the total structural weight of a large transport aircraft.

The specific objective of this Composite Transport Aircraft Wing Technology Development program was to design, manufacture, and test composite wing cover panel structure representative of a commercial transport aircraft that met all strength, aeroelastic, and damage tolerance requirements at the lowest possible cost.

Douglas selected a baseline transport aircraft (Figure 1) with the advanced engineering designation D-3304-2 for the composite wing technology development program. The vehicle considered is an intermediate-range, 150-passenger commercial transport aircraft with propfan engines, planned for introduction into airline service in the mid-1990s. Its high-technology wing (Figure 2) features a supercritical airfoil and a high-aspect ratio for low-drag performance. Design integration studies previously conducted by Douglas indicated that synergistic benefits can be achieved to reduce both drag and structural weight when high-aspect-ratio wings are constructed of lightweight advanced composite materials.



**Figure 1. D-3304-2 Baseline Aircraft**



**Figure 2. Baseline Wing Structural Arrangement**

The results of the Composite Transport Aircraft Wing Technology Development program are described in the following sections. Section 2 deals with material selection and conceptual design of the baseline composite wing. Section 3 provides details on specimen fabrication and test procedures; the impact-testing of the development specimens is also described. Section 4 gives an account of analytical developments, including the NASTRAN modeling of impact damage, a two-dimensional closed-form solution for delamination growth, a peel stress analysis, and a residual strength analysis. Section 5 discusses experimental and analytical results. Finally, Section 6 summarizes achievements resulting from this program.

## **SECTION 2**

### **BASELINE WING DESIGN**

The baseline wing for the composite wing technology program is the D-3304-2 being developed by the Douglas Advanced Engineering department. The D-3304-2 is an intermediate-range, 150-passenger, high-technology transport aircraft with propfan engines, designed for introduction into commercial service in the mid-1990s. The wing features a supercritical airfoil and a high aspect ratio for improved low-drag performance. A general arrangement of the D-3304-2 is shown in Figure 1. The structural arrangement of the wing box shown in Figure 2 indicates the location of spars and ribs, together with the principal external load attachment features. The internal substructure is not substantially changed for the composite design.

The structural arrangement, external loads, and criteria for damage tolerance, and fail-safe requirements were selected, based on the following overall design criteria for the baseline composite wing:

- **Damage Tolerance** — Ultimate load with Mil-A-Prime “just visible” damage.
- **Fail-Safety** — Limit load with visible damage (broken fibers).
- **Residual Strength (Completion of Flight)** — With penetration damage 2 inches in diameter, the aircraft should be able to complete the flight mission.
- **Wing Fuel Tankage** — All tankage: 9-g crash load. With this load, the front spar should be able to resist the pressure.
- **Access Doors** — 0-percent effective. The door will be designed to withstand all pressure and mechanical loads, while the adjoining structure will be designed in such a way that the door is not subjected to any load.

The damage tolerance criteria were selected for defining damage levels at the threshold of visibility and for obvious discrete source damage in accordance with FAR 25.571(e) and AC 20-107A. The new MIL-A-Prime specification for damage tolerance of composite structures, developed under U.S. Air Force contract, served as a guideline. The load requirements for the stiffened cover panel tests were based upon these criteria.

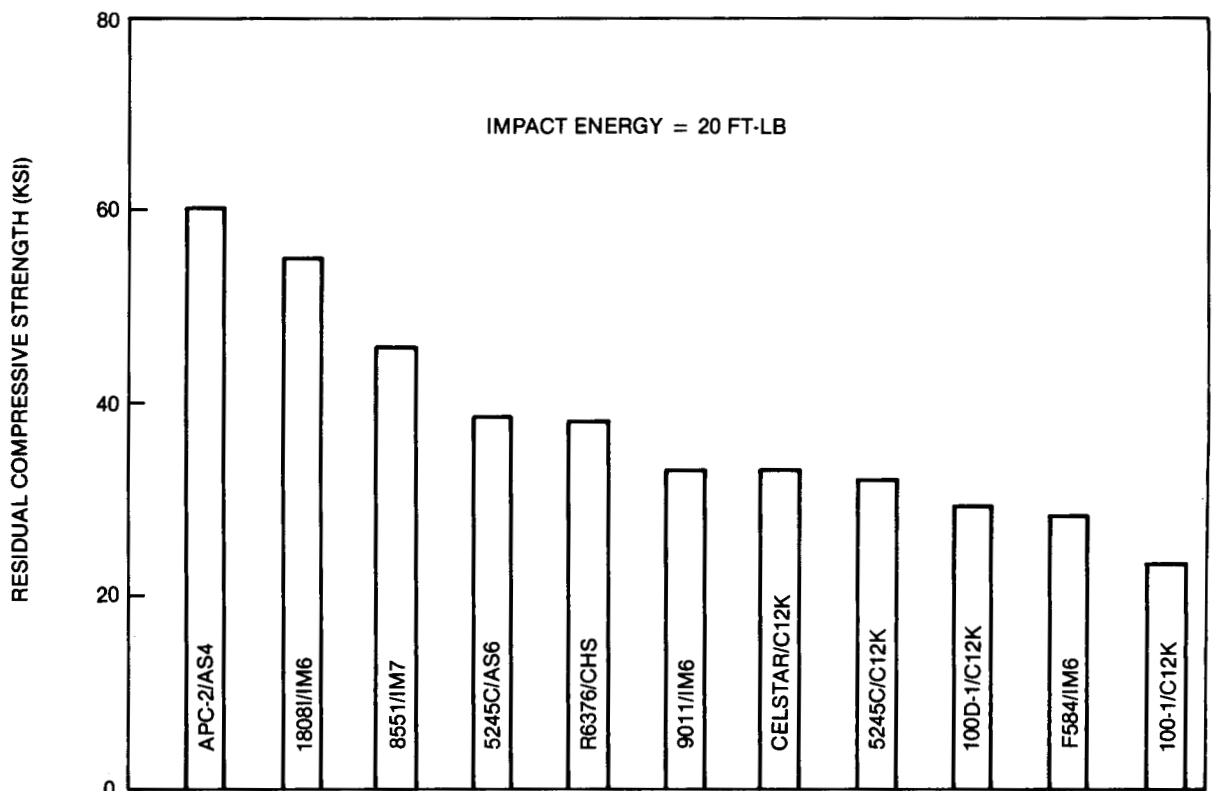
#### **2.1 MATERIAL SELECTION**

Extensive testing was conducted to evaluate candidate materials under Douglas in-house IRAD programs. Several materials (see Table 1) from different manufacturers were evaluated for damage tolerance. Many toughened resin/fiber systems introduced by many suppliers of preimpregnated materials have been evaluated. These systems match high-elongation fibers with toughened ductile-epoxy resins. The NASA ST-1 compression-after-impact test (see Reference 1) was conducted on 11 potential candidate material systems. The residual compressive strength and damage area after impact were determined for all of the materials. The results shown in Figures 3 and 4 indicate that, except for the APC-2/AS4 thermoplastic material, 1808I/IM6 is the most damage-resistant composite material system of currently available materials. The superior damage tolerance of the 1808I/IM6 system results from a thermoplastic adhesive layer (or interleaf) located between plies in the laminate. An example of this damage tolerance is illustrated in Figure 5. The cross sections of 1808I/IM6 and 3501-6/AS4 laminates following 20 ft-lb impacts are shown in the figure, and the 1808I/IM6 laminate is clearly less damaged than the 3501-6/AS4 laminate.



**Table 1**  
**Materials Selection**

• AMERICAN CYANAMID 1808I/IM6	• ICI APC-2/AS4
• FERRO 9011/IM6	• NARMCO 5245C/AS6
• NARMCO 5245C/C12K	• NARMCO CELSTAR/C12K
• NARMCO 100-1/C12K	• NARMCO 100D-1/C12K
• CIBA R636/CHS	• CIBA RX74-21-1/IM6
• HEXCEL F584/IM6	• HERCULES 8551/IM7
• UNION CARBIDE ERLX1962/T40	



**Figure 3. NASA ST-1 Tests — Residual Strength (Room Temperature, Dry)**

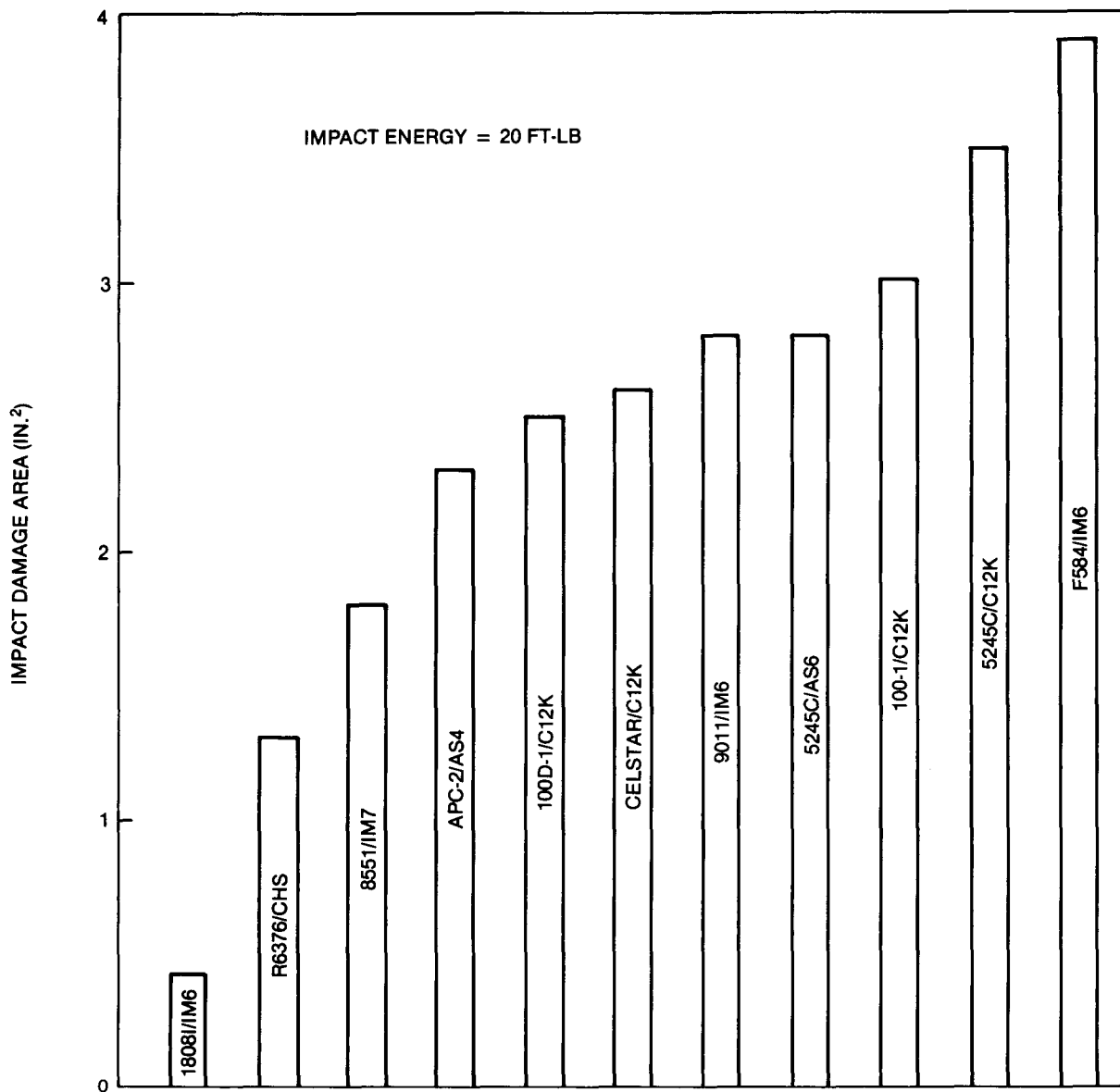
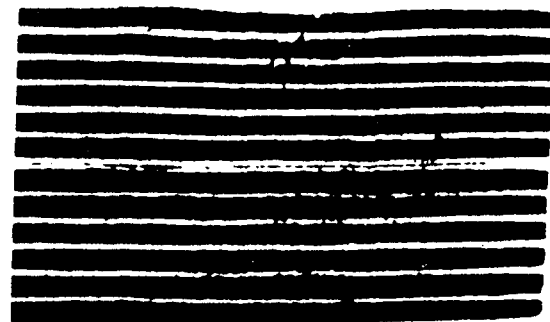


Figure 4. NASA ST-1 Tests — Impact Damage Size (Room Temperature, Dry)



HERCULES  
3501-6/AS4



AMERICAN CYANAMID  
1808I/IM6

Figure 5. Damage After Impact (20-ft-lb Drop) for Composite Wing Material Selection

Several observations have been made regarding the processing, handling, and overall quality of the 1808I/IM6 material. Mechanical and chemical quality control tests indicate that the material will meet the requirements of Douglas process specifications. Preliminary results indicate that the prepreg material seems to exhibit considerable variation from batch to batch, as indicated by the data in Tables 2 and 3. This is particularly the case for ply thickness, which is shown in Table 3 to range from 0.00613 to 0.00637 inch. Later, material supplied by the vendor to fabricate the skin for five-stringer panels resulted in plies that were each 0.0083 inch thick. This poses a design constraint on configurations for which structural components must rely on some laminate thickness tolerance. This material is not procured to a specific specification. The ply thickness would be more consistent if a specification were invoked.

**Table 2**  
**Quality Control Test Data**

ROLL NUMBER		B110	B111	B112	B113	B114
RESIN CONTENT (%)	1.	32.42	32.0	28.55	28.70	32.1
	2.	31.25	31.8	28.98	30.77	29.6
	3.	32.48	31.2	29.63	32.38	30.4
	AVG	32.05	31.7	29.05	30.62	30.7
VOLATILES (%)	1.	1.04	0.87	1.09	1.22	0.91
	2.	1.06	0.81	1.06	1.21	0.97
	3.	1.09	0.75	1.03	1.16	0.87
	AVG	1.06	0.81	1.06	1.20	0.92
THERMOPLASTIC CONTENT (%)	1.	—	8.0	6.67	7.39	6.00
	2.	—	7.7	6.57	6.26	7.20
	3.	—	7.4	5.61	6.72	7.3
	AVG	—	7.7	6.28	6.79	6.8
FIBER AREAL WEIGHT (gm/m <sup>2</sup> )	1.	—	145.4	153.7	150.1	148.4
	2.	—	146.0	151.5	150.7	148.2
	3.	—	149.2	151.6	146.7	147.6
	AVG	—	146.9	153.3	149.2	148.1
GEL TIME AT 350°F (MIN:SEC)	1.	12:55	14:00	11:12	6:57	13:56
	2.	16:32	13:10	7:50	8:56	12:14
	3.	—	13:39	9:41	11:00	12:45
	AVG	14:43	13:36	9:34	8:58	12:58

**Table 3**  
**Average Laminate Per Ply Thickness**

	THICKNESS/PLY (IN.)	ROLL NUMBER
16-PLY PSEUDO-ISOTROPIC	0.00634	B110
18-PLY WING-SKIN	0.00636	B110
24-PLY PSEUDO-ISOTROPIC	0.00637	B110
27-PLY WING-SKIN	0.00614	B112
45-PLY WING-SKIN	0.00626	B111
54-PLY WING-SKIN	0.00613	B112

Monolayer properties and strength of a lamina established for the test prediction (only) for the 1808I/IM6 carbon-epoxy composite material system at room temperature, dry, under an in-house IRAD program are given below.

Elastic Properties of a Lamina		Strength of a Lamina	
$E_L = 18.5 \times 10^6$ psi	$\nu_{LT} = 0.33$	$F_{LT} = 265$ ksi	$F_{TT} = 6.5$ ksi
$E_T = 1.09 \times 10^6$ psi	$t_P = 0.0062$ in.	$F_{LC} = 185$ ksi	$F_{TC} = 34$ ksi
$G_{LT} = 0.70 \times 10^6$ psi		$F_{Sh} = 18.4$ ksi	

## 2.2 CONCEPTUAL DESIGN

The stiffness distribution requirements for the high-aspect-ratio wing of the D-3304-2 are shown in Figures 6 and 7. For this stiffness-critical design, if aeroelastic effects are not considered, the structural weight is purely a function of the extensional modulus of the cover panels. Therefore, the cover skin stacking sequence was selected as the highest possible percentage of 0-degree plies that would not adversely affect the repairability of the structure. High percentages of 45-degree plies were also desirable to meet torsional stiffness requirements. Ultimately, a (0/45/0/-45/0/45/0/-45/90) pattern was selected as a baseline (see Figures 8, 9, and 10), and a design strain of 4,500  $\mu$ in./in. was established. These curves result from tailoring the laminate while keeping the approximate percentage of plies the same.

In general, stringer spacing is a function of extensional ( $E_t$ ) stiffness as shown in Figures 6 and 7. The stringer spacing of 7 inches was decided by realistic design constraints and resulted primarily from the requirement for large access doors along the span. Since the doors are roughly 12 inches wide, only one cut stringer at each door is required. A panel with wider spacing would not carry adequate load, while a panel with narrower spacing would require two cut stringers at each cutout.

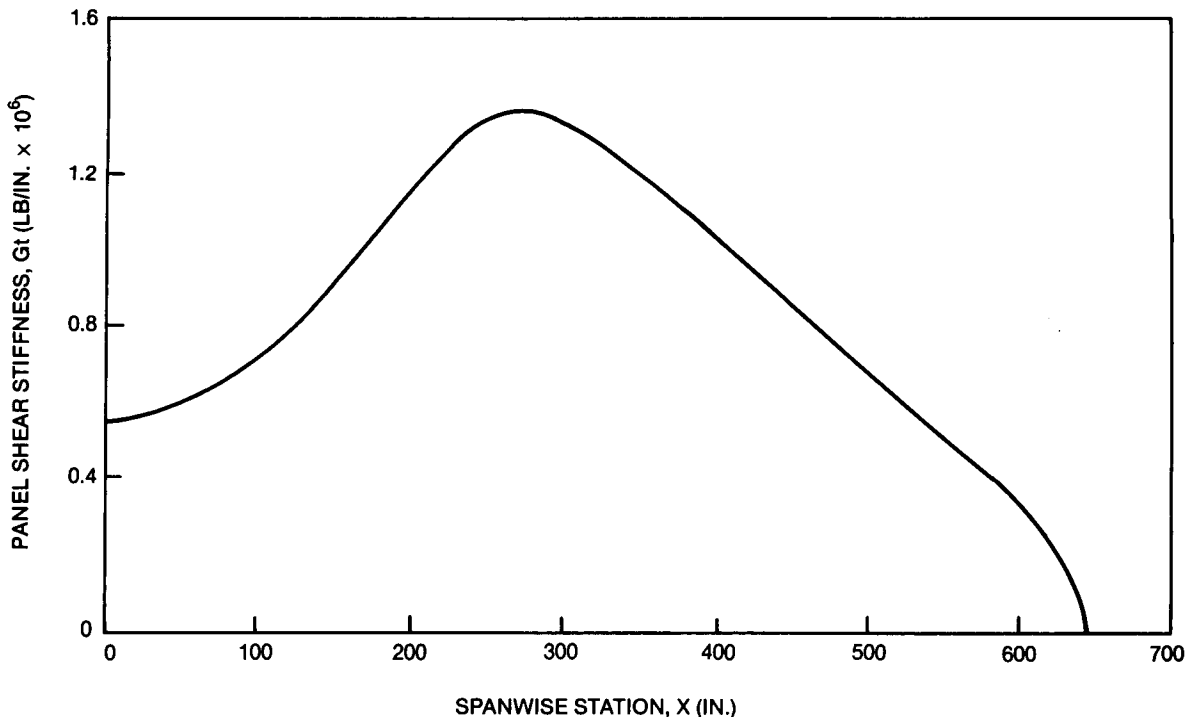
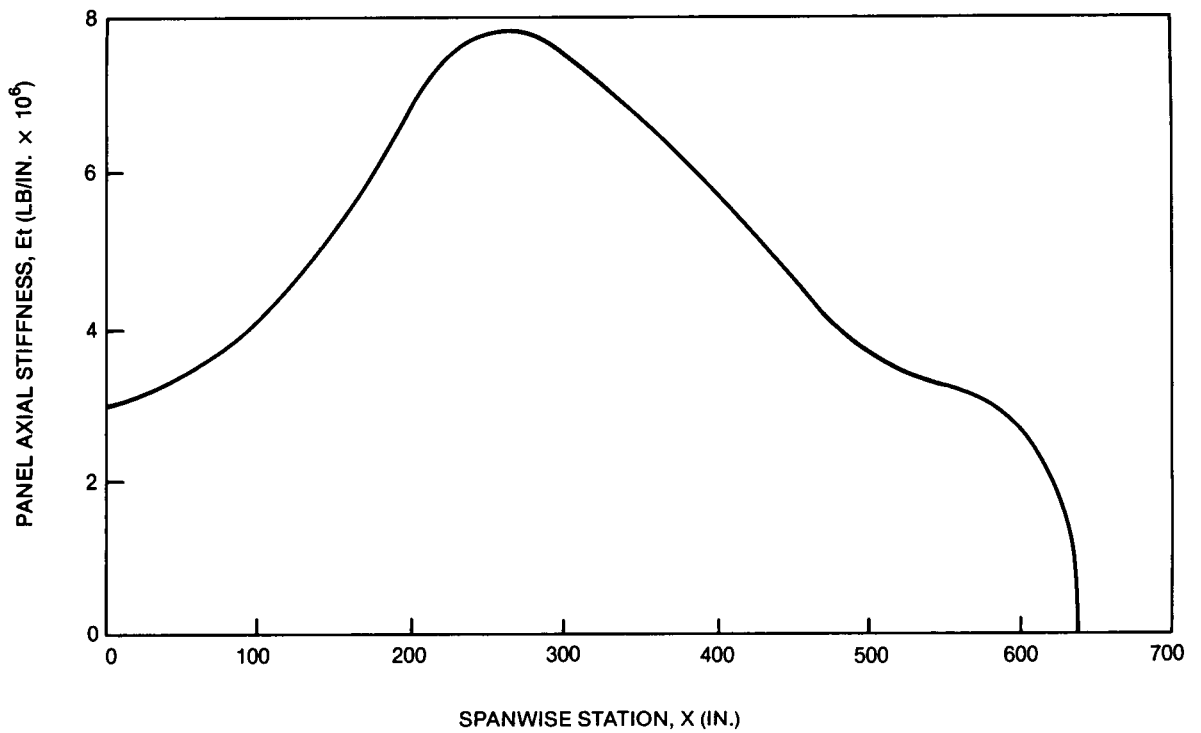
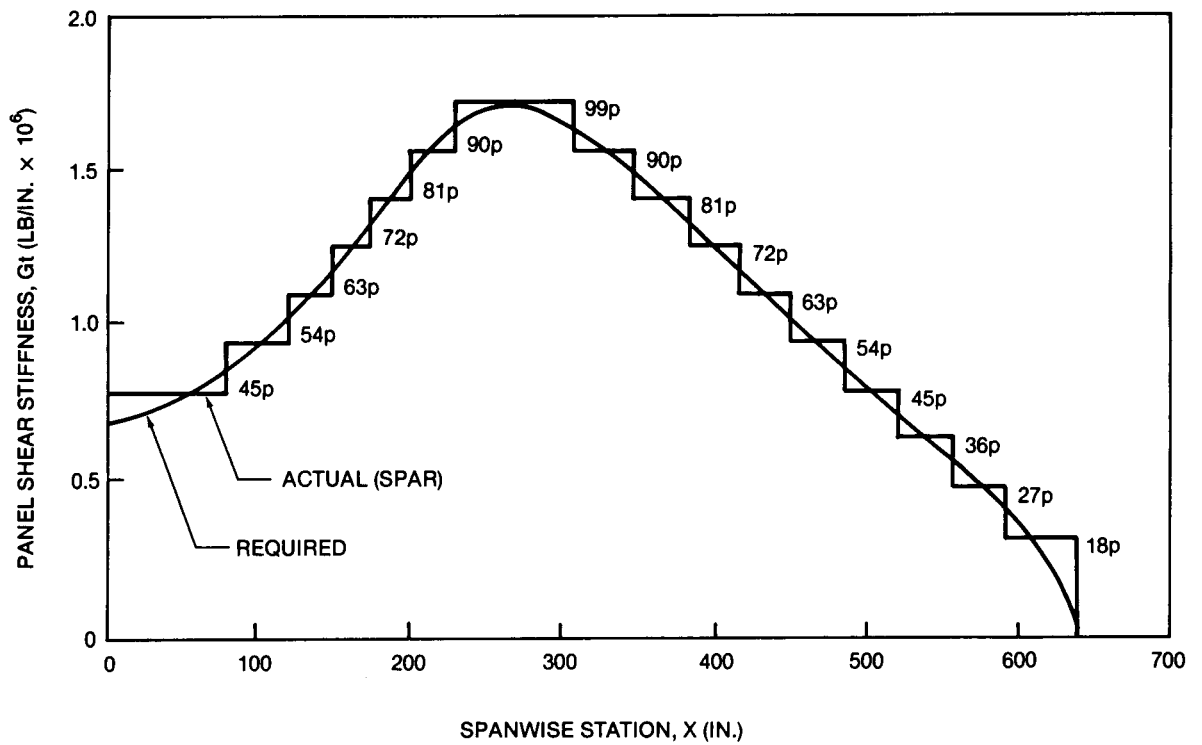


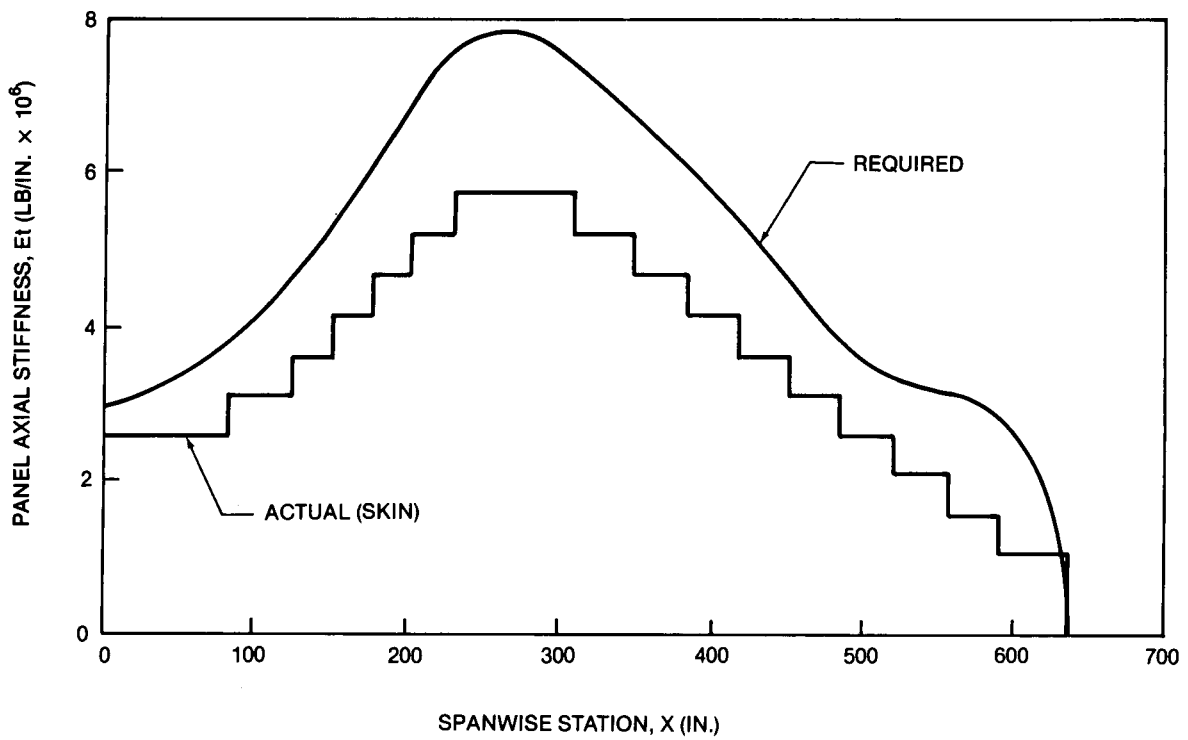
Figure 6. Wing Box Shear Stiffness Requirement



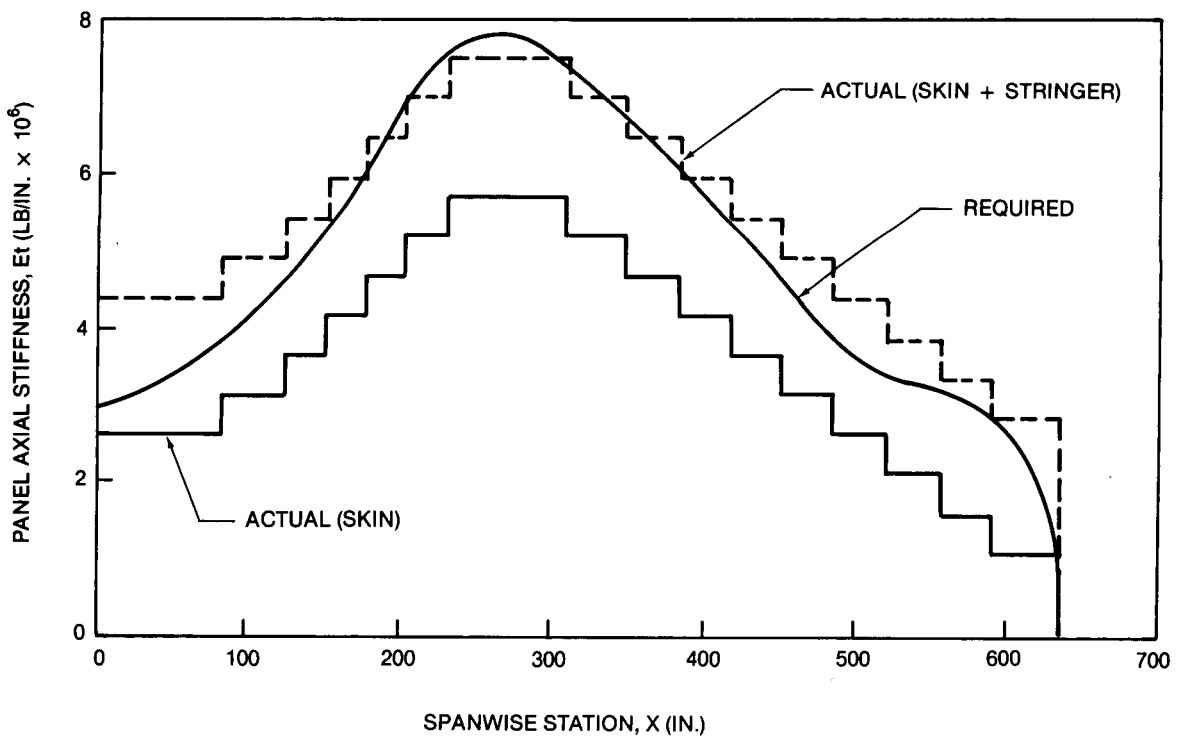
**Figure 7. Wing Box Extensional Stiffness Requirement**



**Figure 8. Shear Stiffness Distribution**



**Figure 9. Extensional Stiffness Distribution**

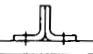
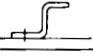

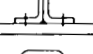
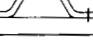
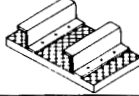
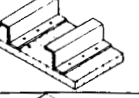

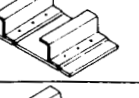
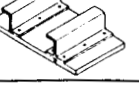


**Figure 10. Extensional Stiffness Distribution in Skin and Stringers (7-inch Pitch)**

The conceptual design effort for this program focused on the detailed design of the stiffened panel test specimens. Various concepts for the details of the stiffened panel design were developed and the most promising candidates were selected for further development. Variables such as configuration, stiffener type and spacing, rib spacing, etc., were considered. All concepts were evaluated in terms of structural efficiency, cost, durability, and repairability. Weight comparison was considered by comparing the selected composite design concept with a conventional aluminum baseline sized to the same load and stiffness requirements.

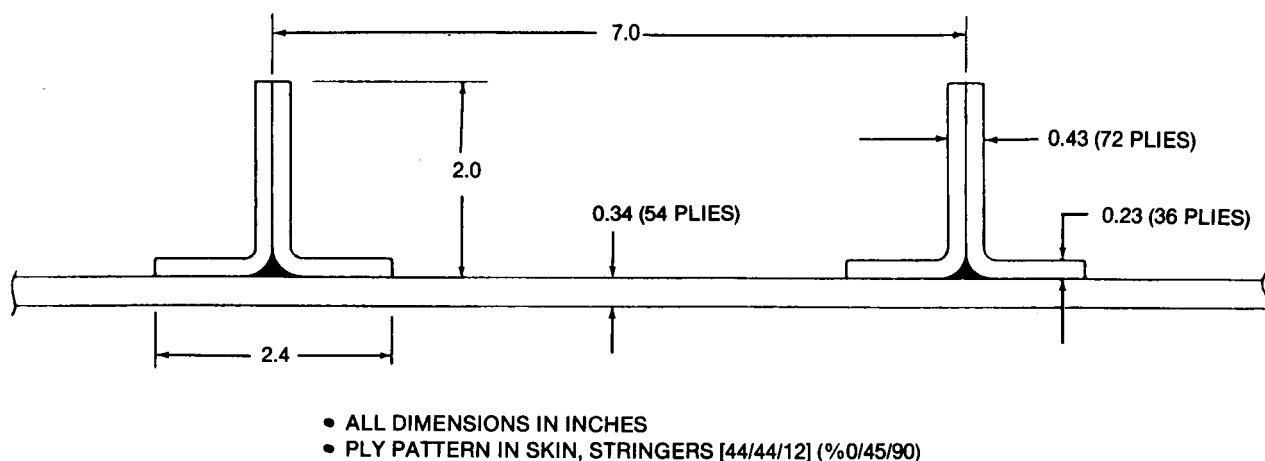
Given the internal loads and strain level limitations resulting from the stiffness-critical configuration of the baseline wing, various cover panel concepts were evaluated for their ability to meet all design requirements. Early evaluations of compression panel configurations shown in Table 4 studied the relative

**Table 4**  
**Selection Criteria for Compression Panel Configuration**

	CONFIGURATION	FABRICABILITY AND SERVICE	STRUCTURAL EFFICIENCY	PREFERRED CONCEPT
ASSEMBLY TYPE	PRECURSED ELEMENTS STRINGERS BOLTED, BONDED, BOLTED/BONDED, OR STITCHED	EASY TO TOOL. LESS RISK OF CURE FAILURE. EASY TO REPAIR. STITCHING IS DIFFICULT FOR PRODUCTION. BONDING REQUIRES GOOD SURFACE PREPARATION.	GOOD STRENGTH AND STABILITY. BOLTED/BONDED ATTACHMENT PREFERRED. BOLTS REQUIRED FOR FUEL PRESSURE.	PRECURSED STRINGERS BOLTED/BONDED TO PRECURSED SKIN USING NORMAL LAYUP PROCEDURE
	COCURED SKIN/STRINGER PANEL REQUIRES THE ADDITION OF FASTENERS TO ATTACH STRINGERS OF THIS SIZE	MORE DIFFICULT TOOLING. ONLY ONE CURE CYCLE REQUIRED. DIFFICULT TO REPAIR. NO MATCHING-FIT PROBLEM.	GOOD STRENGTH AND STABILITY. EQUAL TO BOLTED/BONDED STRINGERS.	
	INTEGRALLY WOVEN ELEMENTS/PANEL CUSTOM WEAVING	REQUIRES CUSTOM WEAVING DEVELOPMENT. +45-DEGREE LAYERS MUST BE ADDED. THICKNESS CHANGES ARE DIFFICULT. REDUCED LAYUP TIME.	GOOD STRENGTH AND STABILITY. WILL NOT COMPLETELY ELIMINATE DELAMINATION UNLESS TOTAL LAYUP CAN BE INTERWOVEN.	
STIFFENER TYPE	BLADE 	EASY TO TOOL. TWO ROWS OF FASTENERS. EASY RIB ATTACH.	STRUCTURALLY INEFFICIENT. IMPROVED PULLOFF	ZEE STRINGERS
	ZEE 	VERY EASY TO TOOL. SINGLE ROW OF FASTENERS. EASY RIB ATTACH.	STRUCTURALLY VERY EFFICIENT.	
	J 	MORE DIFFICULT TO TOOL. TWO ROWS OF FASTENERS. EASY RIB ATTACH/LARGER CUTOUT.	STRUCTURALLY EFFICIENT. IMPROVED PULLOFF.	
	I 	MORE DIFFICULT TO TOOL. TWO ROWS OF FASTENERS. DIFFICULT RIB ATTACH.	STRUCTURALLY EFFICIENT. IMPROVED PULLOFF.	
	HAT 	VERY EASY TO TOOL. TWO ROWS OF FASTENERS. LESS ROOM FOR RIB/SKIN ATTACH. INSPECTION AND FUEL VOLUME PROBLEMS.	STRUCTURALLY VERY EFFICIENT. IMPROVED PULLOFF.	
	ISOGRID	DIFFICULT TO FABRICATE.	STRUCTURALLY EFFICIENT.	
DAMAGE ARRESTMENT TECHNIQUES	SOFT SKIN PREDOMINANTLY +45 DEGREES SOME 0-DEGREE AND 90-DEGREE LAYERS FOR BOLTED REPAIRS 	EASY TO FABRICATE. EASY TO REPAIR.	GOOD STRENGTH AND STABILITY. DAMAGE ARRESTMENT CAPABILITY UNKNOWN.	COMBINED DAMAGE TOLERANCE AND FAIL SAFE APPROACH USING BOTH "SOFT SKIN (B)" AND "PLANKED SKIN (B)" CONCEPTS
	STITCHED SKIN CLOSELY SPACED STITCHING 	DIFFICULT FOR PRODUCTION.	DOUBTFUL WHETHER STITCHING WILL ENHANCE DAMAGE TOLERANCE FOR A TOUGH RESIN SYSTEM.	
	BUFFER STRIPS ZEBRA CLOTH PREFERRED TO HAND LAYUP OF STRIPS 	EASY TO FABRICATE.	BUFFER STRIPS WILL NOT AVOID PROPAGATION OF DELAMINATION.	
	PLANKED SKIN (A) 	EASY TO FABRICATE. FAIRLY EASY TO REPAIR. EXTENSIVE FILLING OF EXTERIOR SURFACE.	FAIL SAFE APPROACH. POSITIVE DAMAGE ARRESTMENT.	
	PLANKED SKIN (B) 	EASY TO FABRICATE. EASY TO REPAIR.	FAIL SAFE APPROACH. POSITIVE DAMAGE ARRESTMENT. EXTENT OF DAMAGE LIMITED BY PLANK WIDTH.	

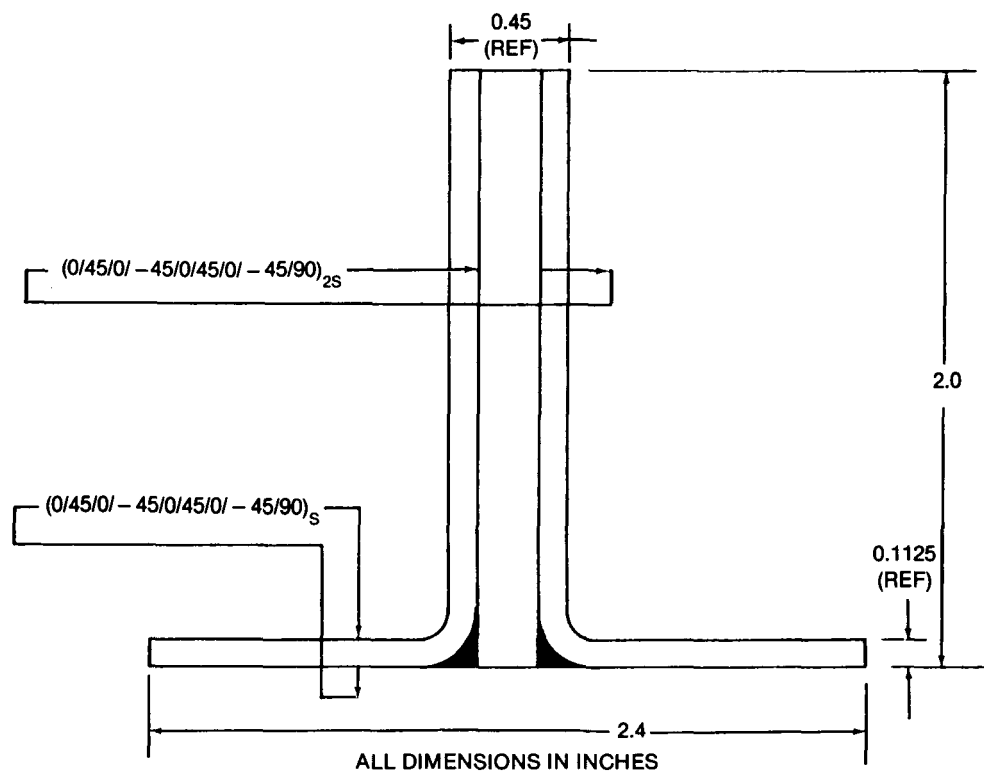
merits of several different concepts. Initial studies were centered on a "soft skin" concept (i.e., low axial stiffness) for enhanced damage tolerance, similar to the approach developed and adopted by McCarty and Whitehead (Reference 2). However, the relatively low stiffness (EA) of these concepts resulted in a substantial weight penalty for the baseline wing structure. Thus, with the strain level limitations imposed for aileron effectivity and with some of the promising properties demonstrated by new material systems, a "hard skin" approach (i.e., high axial stiffness) was selected. The concept shown in Figure 11 represents the baseline wing cover panel design. Several stringer sections were considered, but the various concepts resulted in roughly equal cover panel weights for the stiffness-critical design while maintaining adequate resistance to local and general instabilities. The blade section stringer was selected on the basis of minimum complexity and lower manufacturing costs. The stringers were bonded to the wing skins for cost effectiveness. It was initially assumed that stringers would be secondarily bonded to the skin and that stitching or bolts would only be added when absolutely necessary. The bond line interface is subjected to transverse tension forces due to fuel pressure and other effects. It was found that severe impact loads caused the stringers to separate from the skin in some cases. This problem was resolved by modifying the stringer to incorporate thinner flanges, as shown in Figure 12.

The costs associated with developing, fabricating, and assembling composite aircraft structures are of major, if not primary, importance to a production commitment for primary structure applications. This program develops the technology for a wing cover panel structure that would be readily adaptable to automated, low-cost manufacturing methods, without sacrificing structural integrity.



**Figure 11. Composite Wing Cover Panel Concept**





**Figure 12. Modified Concept for Blade Stringers**

### SECTION 3

#### TEST SPECIMENS AND PROCEDURES

Specimens were fabricated from 1808I/IM6 using the manufacturer's recommended procedures. A typical autoclave cure cycle is shown in Figure 13. Tooling for large composite wing parts was considered in terms of tooling materials and tool design and fabrication. Tool material selection was based on dimensional stability, durability, and a predictable tool life to establish acceptable recurring and overall costs.

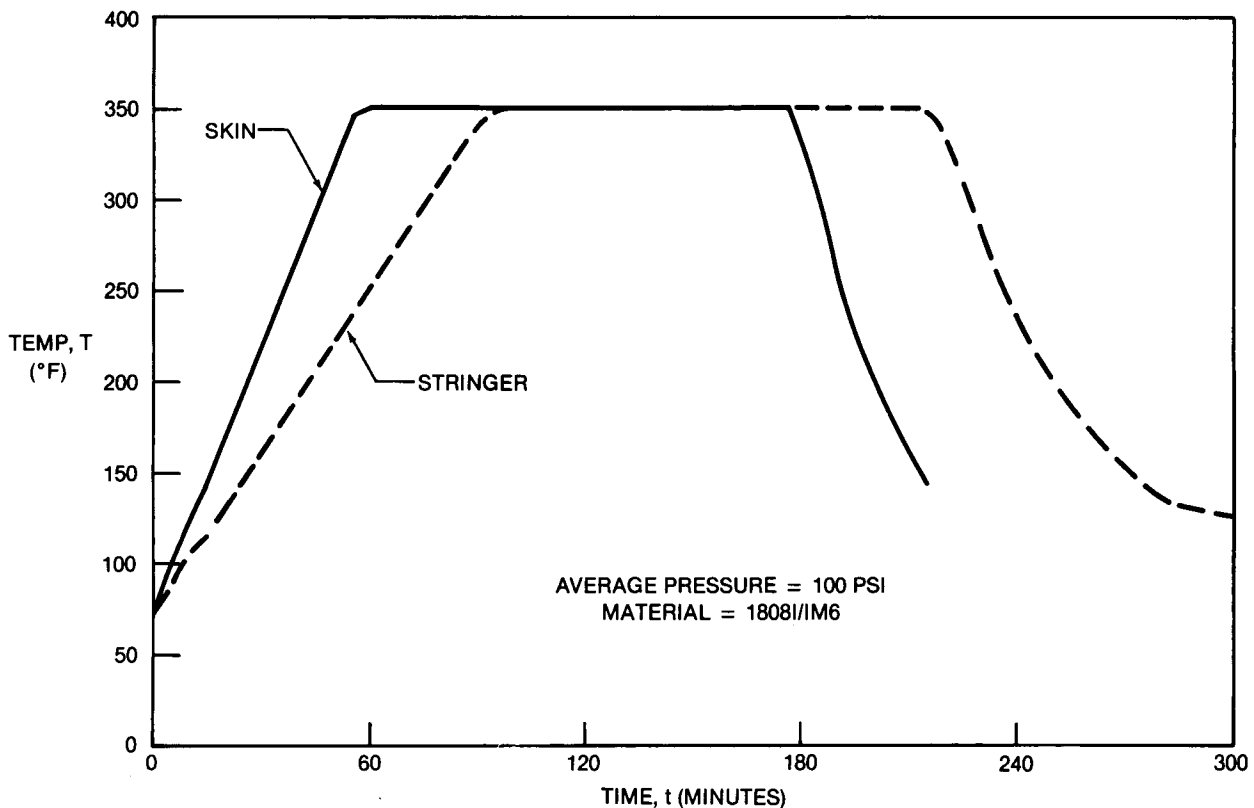


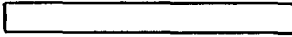
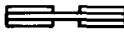

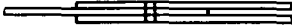
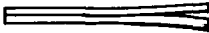

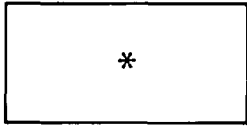
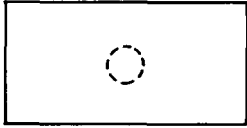

Figure 13. Typical Curing Cycle for Wing Skin and Stringer

#### 3.1 SPECIMEN DESCRIPTION

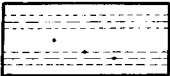

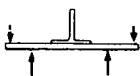
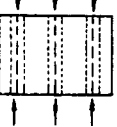
Tables 5, 6, and 7 summarize all the tests performed under this program. Specimens were divided into three categories as given in each table. Ancillary test coupons shown in Table 5 were designed to determine the elastic properties (tension and compression), bearing, toughness characteristics (compression-after-impact, double cantilever beam, edge delamination), and delamination onset stresses (one- and two-dimensional delamination) of the laminates. The dimensions and lay-up of NASA test specimens are given in Reference 1. Bearing and delamination test coupon dimensions and lay-up are shown in Figures 14 and 15, respectively.

Where holes were required in specimens, they were drilled using carbide-tipped twist drills and were reamed to tolerance at low speeds. During the drilling process, the thermoplastic material melted and filled the flutes of the drill bit. However, this was not a serious problem, even for the very thick laminates. It is interesting to note that, when the laminates were drilled with the interleaf material on the back surface, the thermoplastic worked quite well as a backup ply, aiding in the prevention of delamination on the back surface.

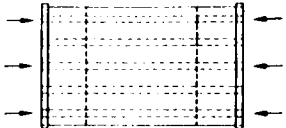

**Table 5**  
**Composite Wing Technology**  
**Ancillary Tests**

TYPE OF TEST		NO. SPECIMENS	
UNNOTCHED TENSION		3	REFERENCE 1
UNNOTCHED COMPRESSION		5	REFERENCE 1
OPEN HOLE COMPRESSION		3	REFERENCE 1
COMPRESSION-BEARING		3	FIGURE 14
DOUBLE CANTILEVER BEAM		3	REFERENCE 1
EDGE DELAMINATION		6	REFERENCE 1
COMPRESSION-AFTER-IMPACT		5	REFERENCE 1
2-D DELAMINATION		3	FIGURE 15
1-D DELAMINATION		18	FIGURE 15

**Table 6**  
**Composite Wing Technology**  
**Development Tests**

PANEL TYPE		NUMBER OF SPECIMENS	TYPE OF TEST
TRIAL IMPACT		2	TRIAL IMPACT DAMAGE NDI AND EVALUATION
CRIPPLING SPECIMEN		3	COMPRESSION STRENGTH
STRINGER PEEL TEST		3	PEEL TEST
SCREENING TESTS WITH SELECTED LEVELS OF IMPACT DAMAGE		5	RESIDUAL COMPRESSION STRENGTH

**Table 7**  
**Composite Wing Technology**  
**Demonstration Tests**

PANEL TYPE		NO. SPECIMENS	TYPE OF TEST
DISCRETE SOURCE DAMAGE		1	RESIDUAL COMPRESSION STRENGTH
VISIBLE IMPACT DAMAGE		1	RESIDUAL COMPRESSION STRENGTH

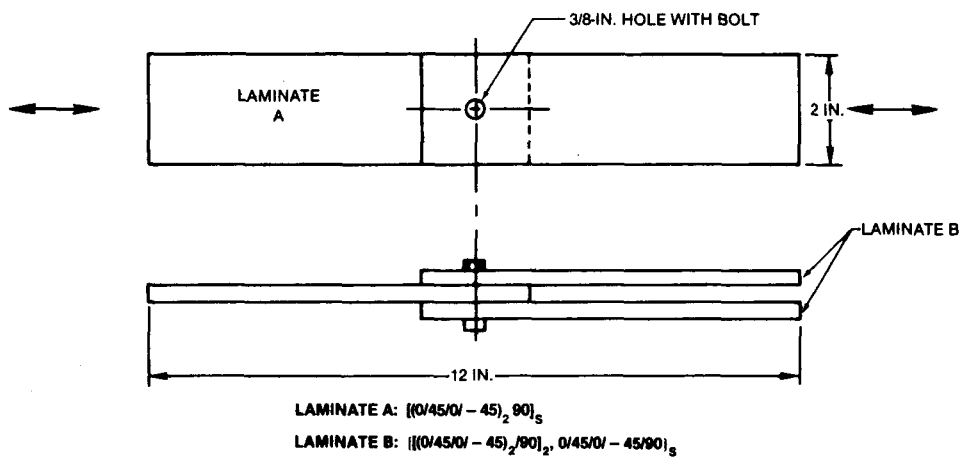


Figure 14. Tension and Compression Bearing Test Specimen

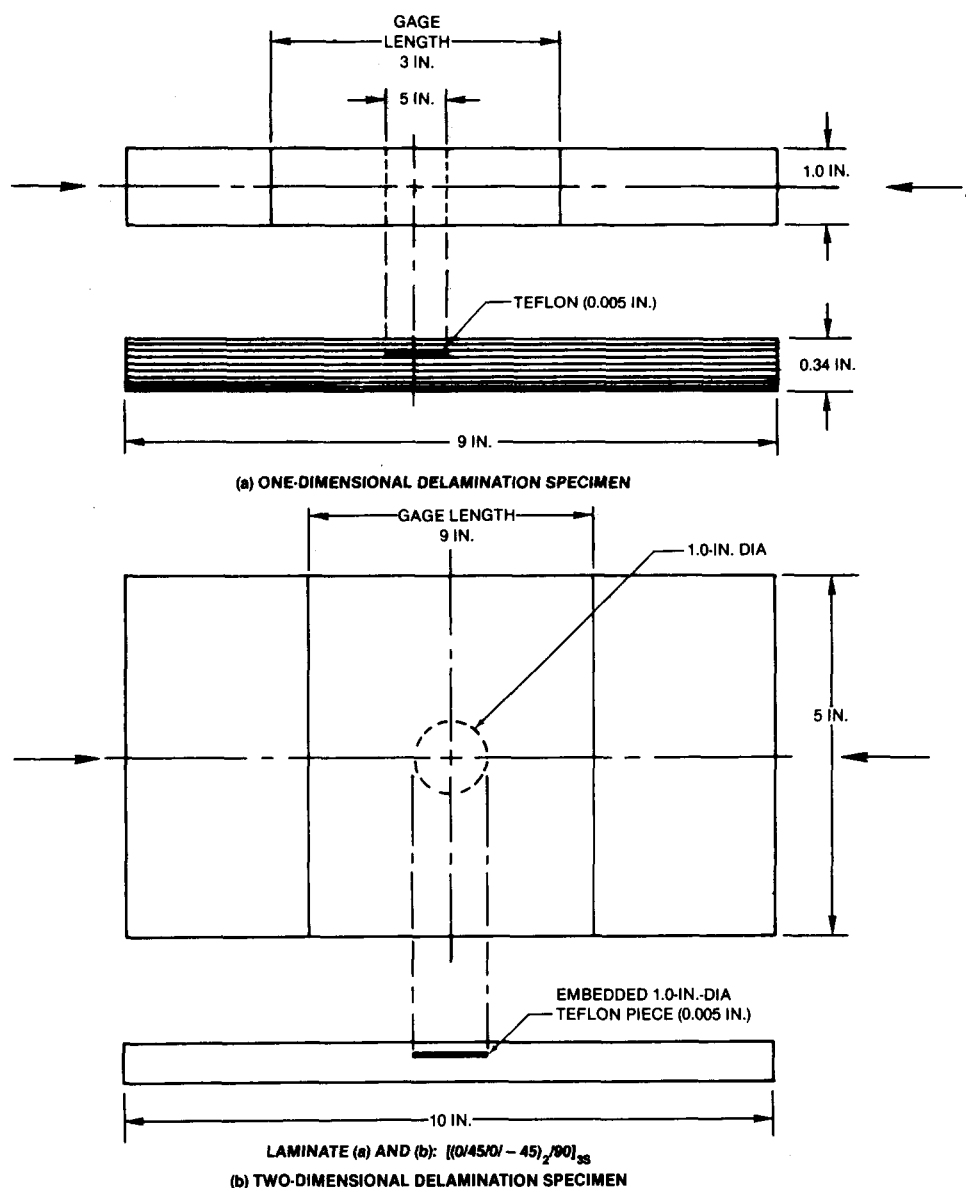


Figure 15. Compression-Delamination Specimens

Table 6 summarizes the development tests, and Figures 16, 17, and 18 show the dimensions (see Table 8) of test specimens. These trial impact, compressive strength, and residual compressive strength tests were designed to determine the residual strength for various impact damages. The peel stress tests gave interlaminar stresses in the adhesively bonded structure. The demonstration panel specimens are given in Table 7. These panels were fabricated and impact-damaged at Douglas, and then shipped to NASA where the compression-after-impact tests were conducted.

Attachments to or through the stringer blades were avoided because of the bonded assembly of skins and stringers on the baseline composite wing. This approach was adopted in order to minimize the possibility of developing critical interlaminar tension stresses at the bond line interface. The most critical load conditions that will produce interlaminar tension stresses between skins and stringers result from internal fuel pressure in combination with some other load case. This phenomenon is described in Figure 16, where the tension pull-off test is compared to the actual conditions found in the baseline design.

After evaluating several different concepts for this specimen, two configurations shown in Figure 16 were selected. The test consisted of a single-stringer panel, roughly square in plan view, which was loaded in a four-point bending with the loads applied on the skin side of the panel. The deflections induced under these loads were similar to those resulting from internal fuel tank pressures in the actual wing. The tensile stresses developed at the interface were not load-induced, but were deflection-induced, and resulted in critical peel stresses at the edge of the stringer flange.

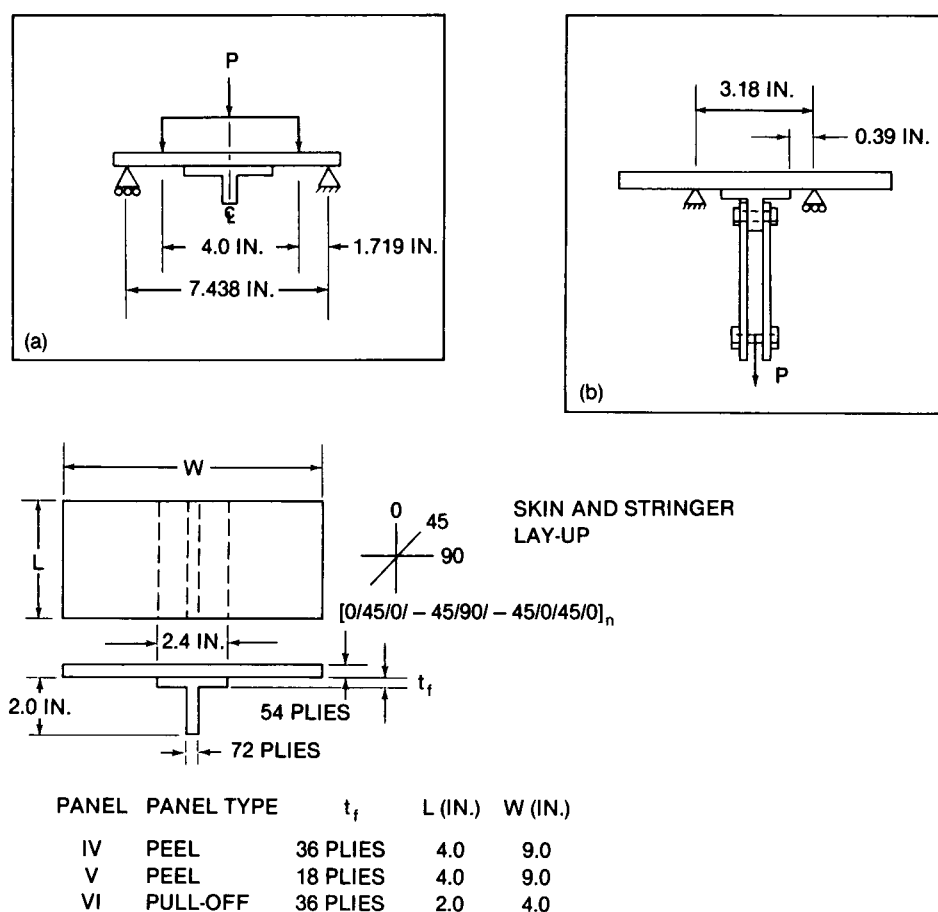
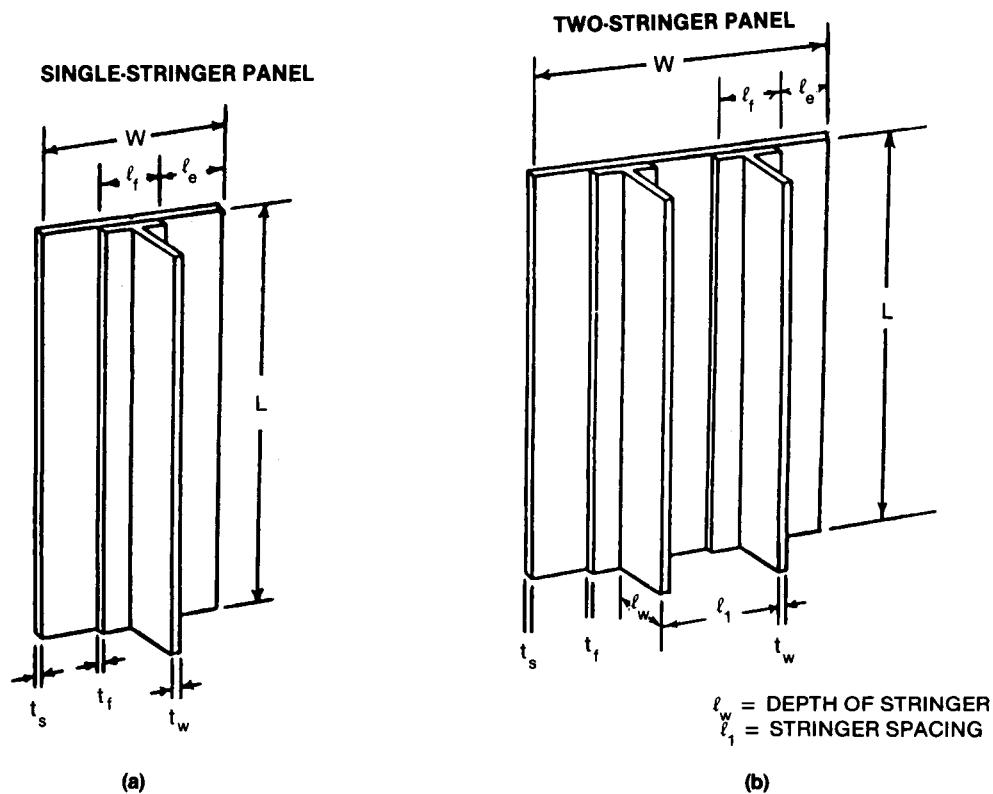


Figure 16. Peel (a) and Pull-Off (b) Specimen Configurations



SEE TABLE 8 FOR DIMENSIONS

Figure 17. Trial Impact Specimens

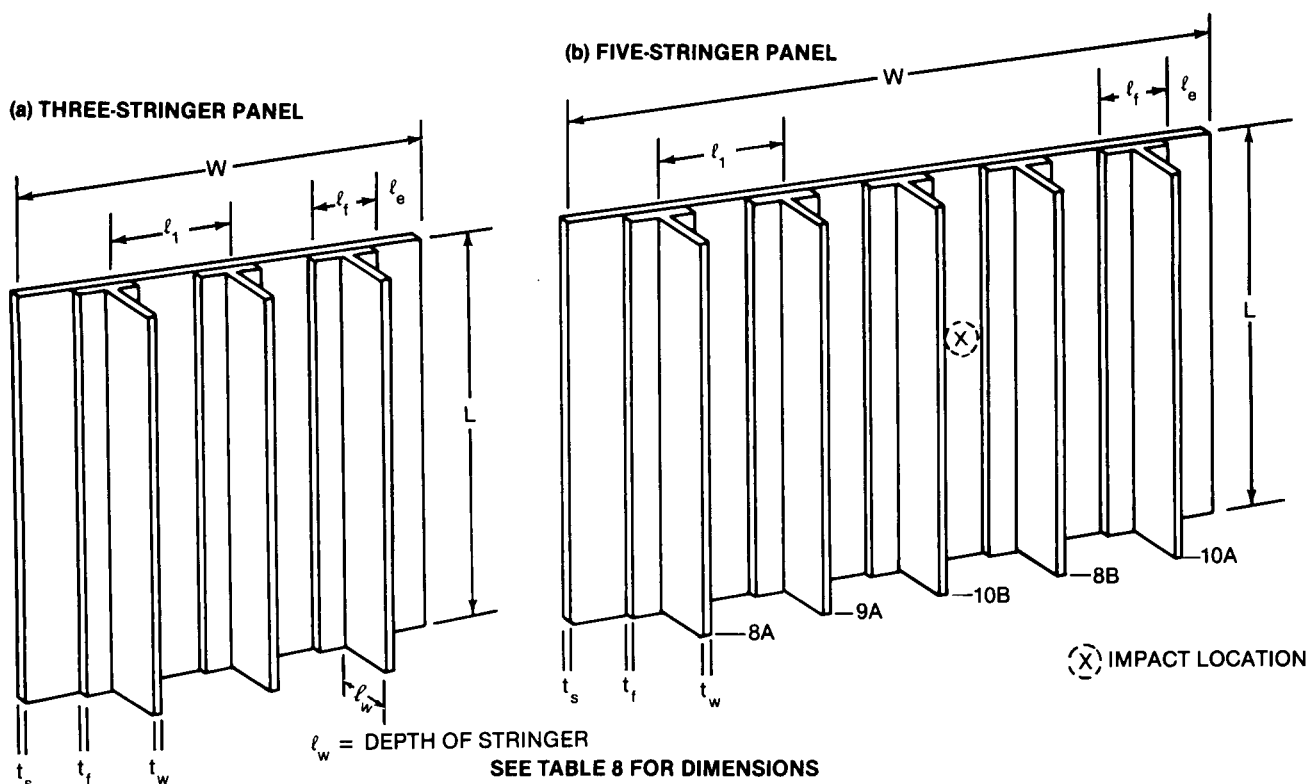


Figure 18. Damage Screening and Damage Tolerance Compression Panels

**Table 8**  
**Stiffened Panels**  
(Nominal Dimensions in Inches)

DIM.	DESCRIPTION	3-STRINGER		NUMBER OF STRINGERS		
		C-TYPE	B-TYPE	1	2	5
W	PANEL WIDTH	20.0	21.0	5.0	14.0	33.0
L	PANEL LENGTH	18.0	15.0	20.0	36.0	56.0
$\ell_w$	STRINGER DEPTH	2.0	2.0	2.0	2.0	2.0
$\ell_f$	FLANGE LENGTH	2.4	2.4	2.4	2.4	2.4
$\ell_1$	STRINGER SPACINGS	7.0	7.0	—	7.0	7.0
$\ell_e$	STRINGER EDGE DISTANCE	2.5	3.0	1.3	2.3	2.5
$t_f$	FLANGE THICKNESS	0.11	0.23	0.11	0.23	0.11
$t_w$	STRINGER WEB THICKNESS	0.46	0.46	0.46	0.46	0.43
$t_s$	SKIN PANEL THICKNESS	0.35	0.35	0.35	0.35	0.43

### 3.2 SPECIMEN FABRICATION

Techniques for fabricating stringer and skins, and for assembling all the test specimens are given in detail in this section.

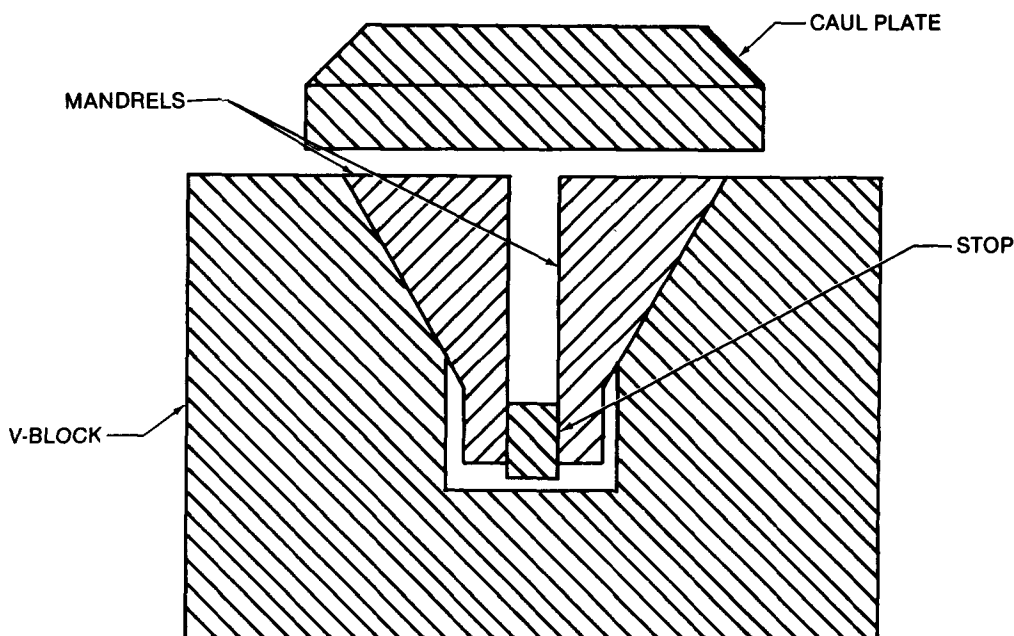
#### 3.2.1 Stringer Fabrication

A tooling concept for the fabrication of blade stringers (see Figures 17 and 18) was selected, based on in-house tooling concept development. The selected approach, illustrated in Figure 19, uses matched metal tooling made from 6061-T6 aluminum. The parts consist of a V-block, two matched mandrels, blade stops, and an upper caul plate. During in-house development work, stringer sections made with this tooling demonstrated accurate section geometry, excellent dimensional stability, and a superior surface finish. In addition, this concept may be used in either a press or autoclave cure.

The composite lay-up takes place directly on the mandrels with the stringer section in halves. The part is debulked, chilled, and released from the tool surface. Release film is applied at the interface between the tool and the part, which is then placed between the mandrels with the required blade thickness set by the mechanical stops. The mandrels are linked vertically by a set of pins, which pass through the stop. The mandrels are placed in the V-block, the upper caul plate is fitted into place, and the entire upper surface of the tool is sealed with a vacuum bag. During cure, autoclave pressure forces down the upper caul plate, which in turn forces the mandrels further into the V-block. This transfers pressure into the blade section of the stringer until the stop gap has been reached.

All the stringers for single-stringer and multistringers panels were fabricated using the above tooling concepts. The fabrication of 6-foot stringer tools for use in fabricating the large five-stringer cover panel specimens was completed, and the stringers were subsequently bonded to the skin panels. The nominal dimensions of all the stiffened panels are given in Table 8, and those of the compression test and trial impact panels are shown in Figure 17. Flanges were constructed from 36 plies of 1808I/IM6 material for





**Figure 19. Stringer Tooling Concept**

single-, double-, and three-stringer panels (see Figure 11). Later, however, an 18-ply flange (Figure 12) was used for the five-stringer panels. This concept was superior to the 36-ply-flange concept in resisting impacts without disbonding of the skin.

### 3.2.2 Skin Fabrication

Skin panels for single- and multistringers were fabricated with 54 plies of 1808I/IM6 material as given in Table 8. Except for the five-stringer panels, the thickness of the skins was 0.35 inch with  $[(45/0/-45/0)_2/90]_{3S}$  laminate configurations. The five-stringer panels were 0.43 inch thick because the interleaf film material received from CYCOM was thicker than that received earlier. The skin for all panels was manually laid up and cured with the standard curing cycle and was within the maximum allowable porosity level of 2 percent.

### 3.2.3 Skin-Stringer Assembly

When the stringers were placed over the skin panel in order to bond them together, gaps of different sizes were found between the stringers and skin along the centerline normal to the stringers (see Figure 18b). The gap was 0.03 inch for stringer 8A, 0.018 inch for stringer 9A, 0.019 inch for stringer 10B, and 0.012 inch for stringer 10A. Such gaps at full pressure would produce areas of undesirable porosity in the bond line. A special nonadhering epoxy film, FM641, known as Verifilm Green has been developed to check for the presence of gaps at full pressure and temperature. A single ply of the 0.015-inch-thick FM641 was sandwiched between the two plies of 0.001-inch-thick Mylar. The usual bagging procedure was employed using the FM641 instead of the FM300.

All bond lines were sealed using 1-inch aluminum foil tape, which was faired up to 90 degrees from the skin, over the flange of the stringer. A Coreprene dam was placed over this foil to mate with and soften the flange edges. Once the panel was on the caul plate, four layers of Coreprene dam with the foil were laid on the ends of the stringers. All dams were sealed to the part with the pressure-sensitive Mylar tape.

Before the Verifilm was applied to the panel, quite a few tests at the coupon level were conducted. These tests demonstrated that the presence of the FM641 layer improved the bond line strength to 4,911 psi, while the through-ply arrangement of FM300 gave 2,919 psi. After bagging, the panel was cured at 290°F and 50 psi for 15 minutes, and then cooled down to 150°F for inspection. The bond lines measured 0.013-0.015 inch for 8A, 0.014-0.016 inch for 9A, 0.013-0.014 inch for 10B, 0.012-0.015 inch for 8B, and 0.012-0.014 inch for 10A. In all cases, the Verifilm was uniform across the bond lines except where pressure was lost directly under the blade in three separate 1.5-inch areas. The Verifilm determines the size of gaps to be closed by adhesives and is not an adhesive itself.

### 3.2.4 Demonstration Panels

Two five-stringer panels have been fabricated using the same cure cycle. The skin panels were made from a recently procured material with a thickness of 0.0083 inch per ply. These large panels, which were impact-damaged at Douglas, were compression-tested at NASA Langley. The test plan sent to NASA shows that one panel will have visible damage and the other will have discrete source impact damage at midbay. To achieve visible damage, several trial impact tests were conducted on several undamaged parts of already impacted two-stringer panels. Finally, both five-stringer panels were impacted at midbay with 100 ft-lb of impact energy using a 17-inch support span. No NDI-detectable damage was produced when the first panel was impacted with a 1-inch-diameter impactor. The second panel was impacted with a 1/4-inch-diameter impactor, and visible damage resulted. The C-scan for this panel is shown in Figure 20. Both panels were impacted using a 17-inch center support span to compare the

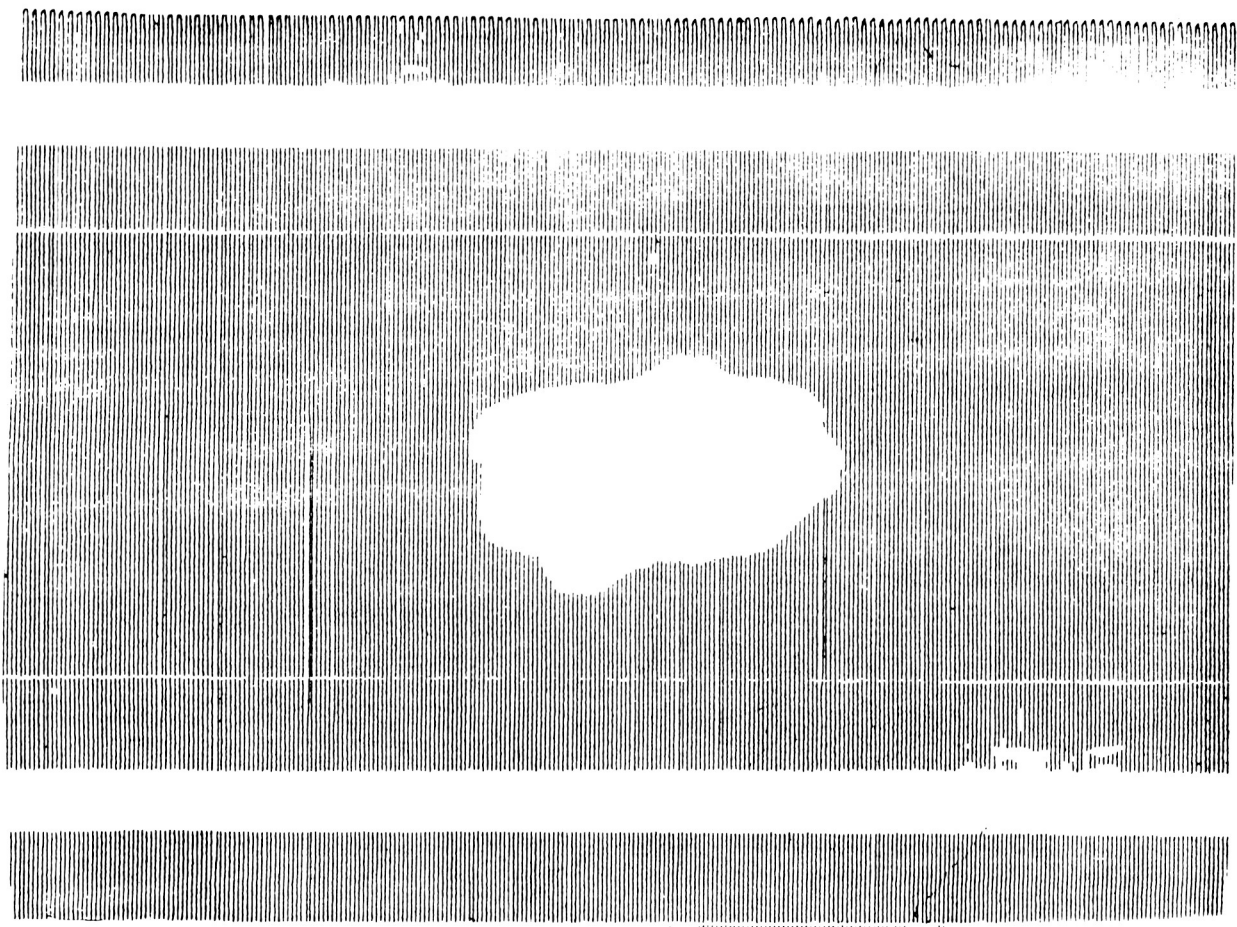
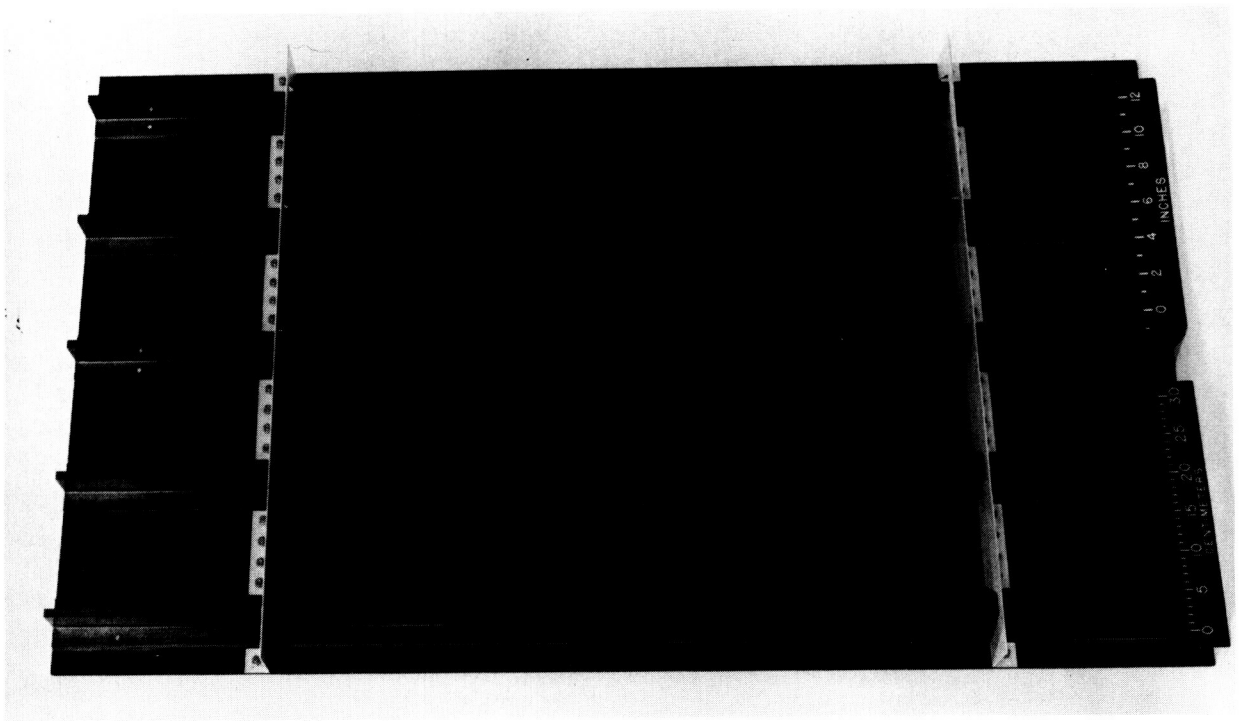


Figure 20. NDI of Panel D2 After Impact (Visible Damage — 100-ft-lb, 1/4-in. Impactor)



**Figure 21. Demonstration Panel (Five-Stringer Panel)**

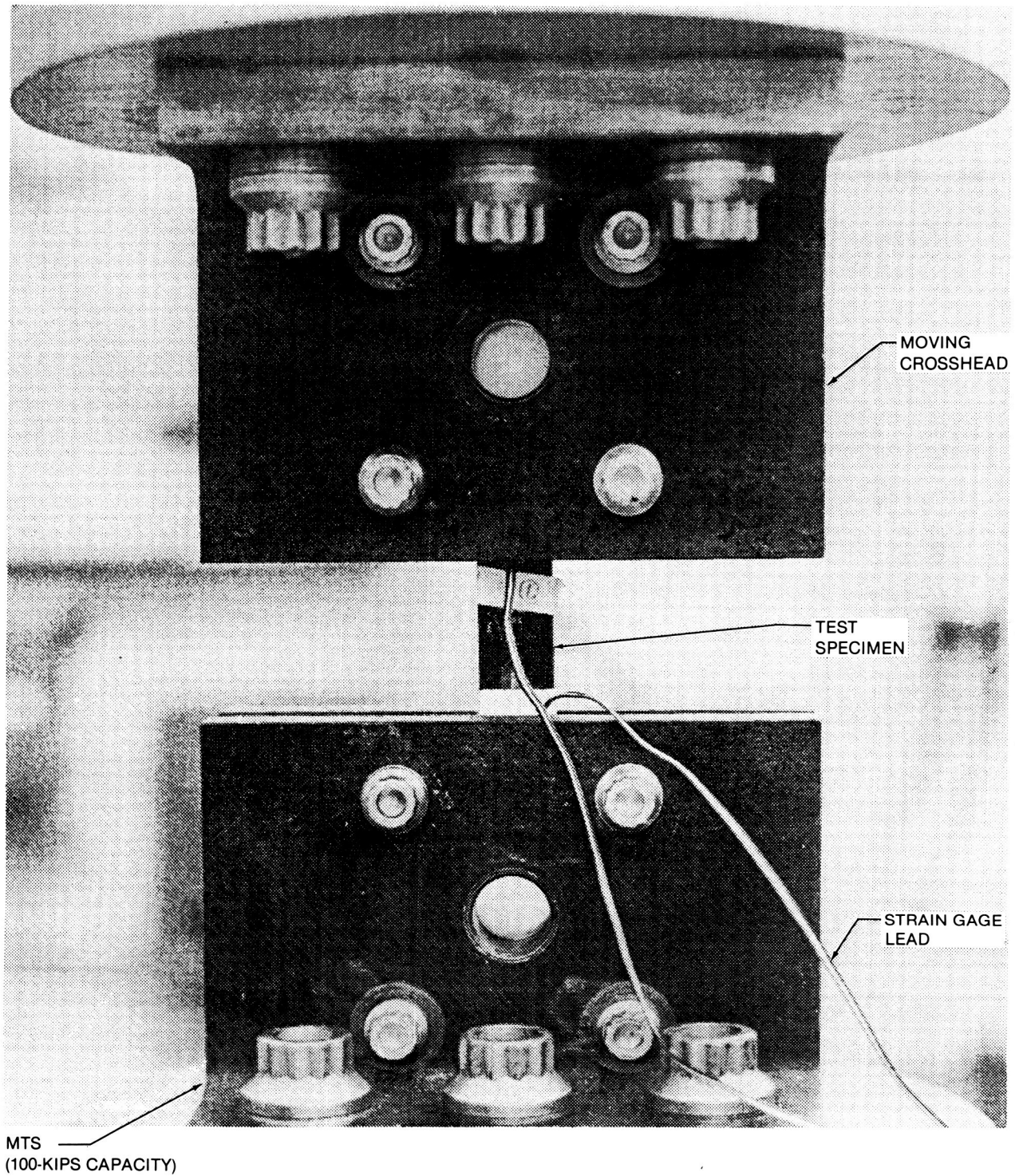
results with the three-stringer panels. The 1/4-inch impactor penetrated halfway into the skin. Two aluminum ribs were fabricated from angle sections for each panel and attached to the skin with bolts at 37-inch center spans (see Figure 21). The panels only differed from each other by about 1/4 inch in length. All other dimensions are the same for both panels, as shown in Table 8.

### **3.3 TEST PROCEDURES**

#### **3.3.1 Ancillary Tests**

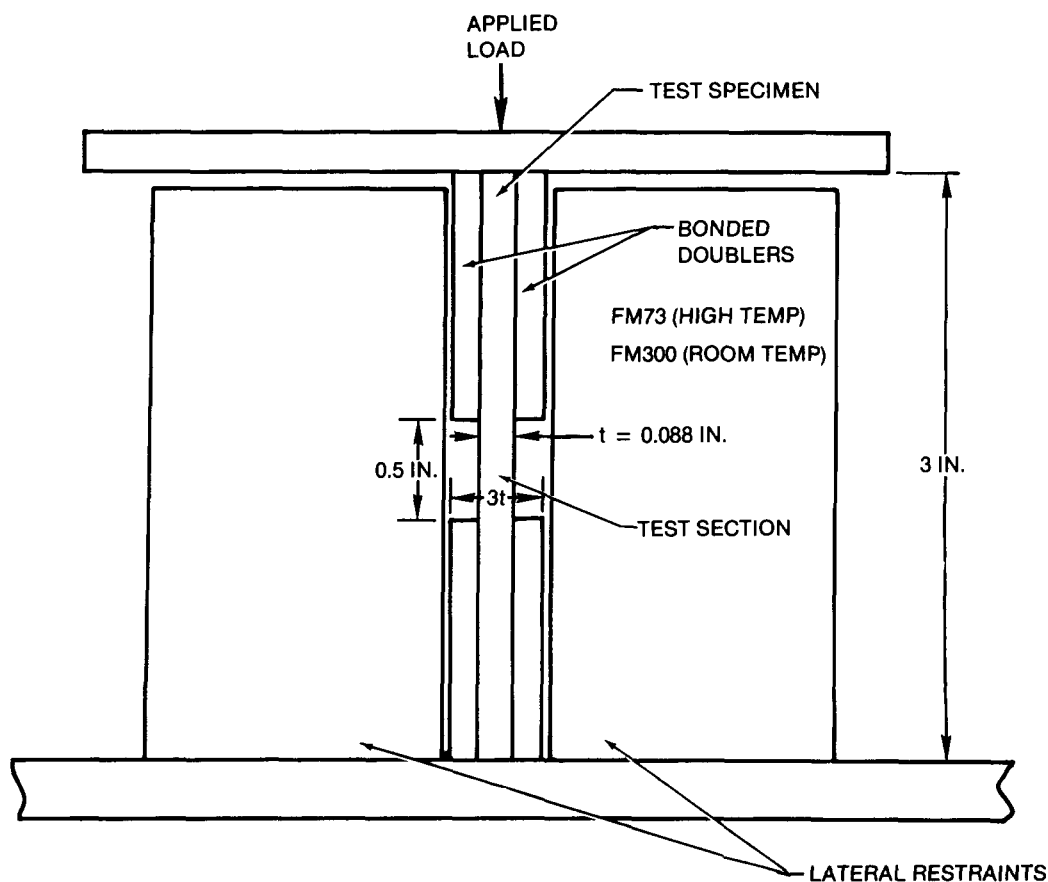
All the tests except compression-delamination and bearing tests were conducted in accordance with Reference 1. Each part of the specimens was C-scanned before and after assembly. The specimens were instrumented with strain gages before testing. These tests were performed in a 1.1-million-pound-capacity machine with a 0.05-in./min controlled stroke. The compression test was conducted in the setup shown in Figure 22. All the test specimen ends and sides were kept parallel to each other to within a 0.005-inch tolerance. Thickness and width of the test coupon parts were recorded by taking the average of more than seven places on the part using a micrometer. Strain measurements, where applicable, were recorded at different load increments. Load-deflection history and failure load were recorded for each specimen. Depending on the test, the specimens were C-scanned after the test to determine the extent of the damage.

Two-dimensional compression delamination specimens were tested in the ST-1 (Reference 1) fixture with antibuckling plates. One-dimensional delamination tests were performed in a setup similar to that shown in Figure 23.



**Figure 22. One-Dimensional Delamination Coupon Test Setup**

ORIGINAL PAGE  
BLACK AND WHITE PHOTOGRAPH



**Figure 23. Unnotched Compression Test Setup**

### 3.3.2 Development Tests

The development tests concentrated on three areas. The first test in this group involved impacting two-stringer panels at midbay, stringer flange, stringer blade, and laterally on the stringer blade. These panels were impacted at various energy levels ranging from 20 to 100 ft-lb. After impact damage was inflicted, the panels were nondestructively inspected to determine the severity of damage. The results were used to determine the amount of impact to be applied to three-stringer panels. All of these panels were supported at their opposite edges similar to the configuration shown in Figure 24a.

Stringer pull-off tests were also conducted. These tests were designed to simulate wing skin flexing due to aerodynamic loads or pressurization of the fuel tank. The tests examined the strength of the bond between the stringer and the skin. Four-point beam bending loads were applied in such a manner that the stringer flanges were peeled from the skin without the application of direct tension of the stringer blade.

The impact locations of two- and three-stringer panels are shown in Figure 25. The structural test plan was drafted with NASA consultation to test three-stringer damage tolerance panels after they were impact-damaged with 100 ft-lb of energy at different locations. One of the panels was impacted with 200 ft-lb of energy, which resulted in visible damage.

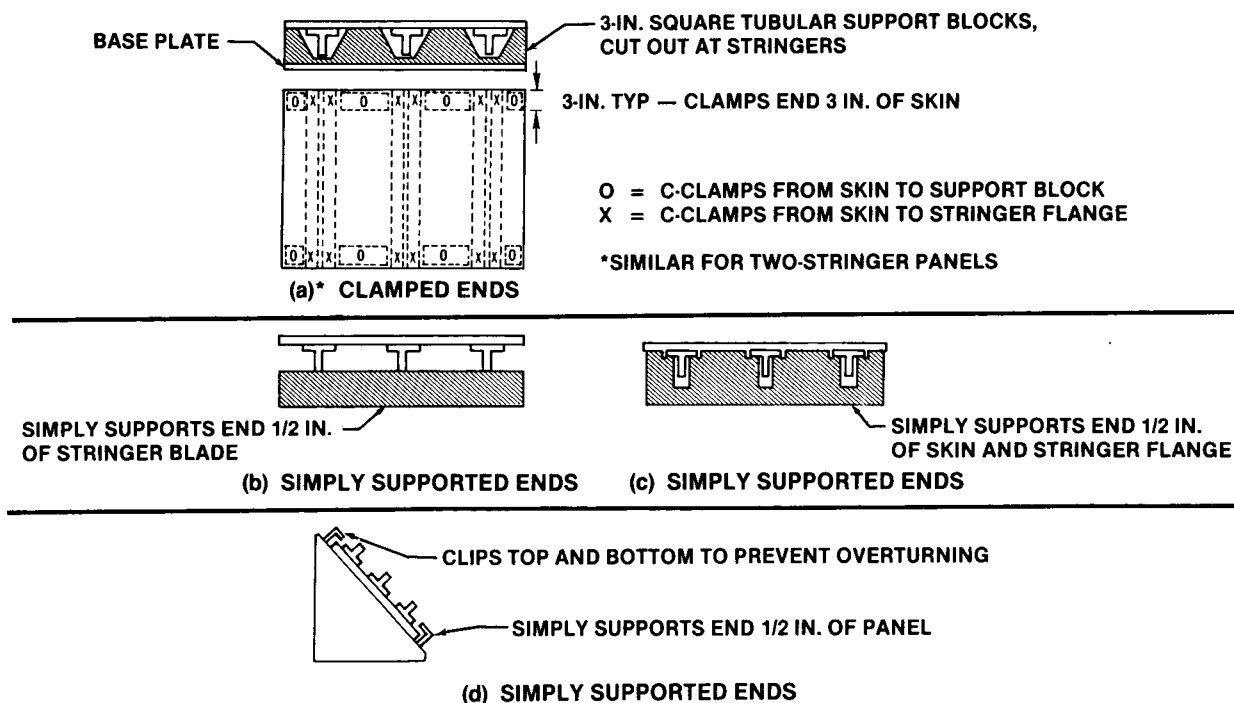
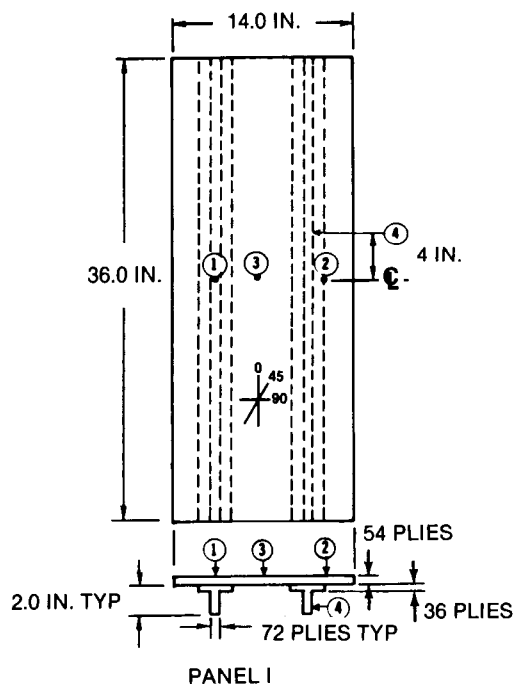


Figure 24. Support Conditions for Impact Tests



135.6 N-m (100 FT-LB) IMPACT LOCATIONS	
1. OVER BLADE	2-STRINGER PANELS
2. OVER FLANGE EDGE	2-STRINGER PANELS
3. MIDBAY	2-STRINGER PANELS
4. LATERAL BLADE	2-STRINGER PANELS
5. OVER BLADE	3-STRINGER PANELS
6. OVER FLANGE EDGE	3-STRINGER PANELS
7. MIDBAY	3-STRINGER PANELS
8. 45-DEG LATERAL BLADE	3-STRINGER PANELS
ALL SKIN AND STRINGER LAY-UPS [0/45/0/- 45/0/45/0/- 45/90] <sub>n</sub> (SYM)	

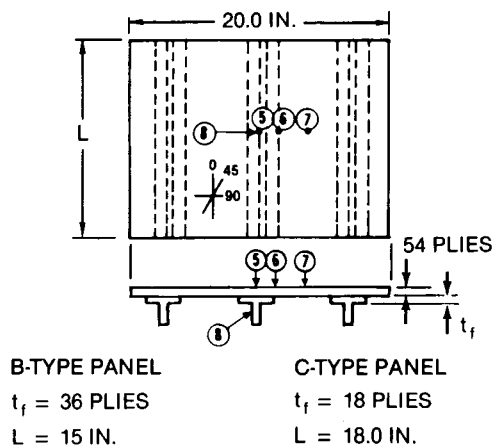


Figure 25. Impact Panel Configurations and Impact Locations



**3.3.2.1 Impact Tests** — The impact test requirements currently proposed under AFWAL contract (Reference 2) call for ultimate strength to be maintained following an impact level that just causes visual damage, up to a maximum of 100 ft-lb. The laminates fabricated with interleaved material had no visual damage when tested below the maximum impact energy level. Therefore, all panels were impacted at 100 ft-lb. This impact was attained by dropping a 1-inch-diameter impactor (attached to a 21.8-pound weight) from a height of 55 inches.

Locations for external skin impacts were midbay between stringers, over the blade, and over the stringer flange edge. Internal impact tests were applied laterally on the stringer blade. Tables 9 through 11 describe each test individually, while Figures 16, 24, and 25 detail the associated impact locations and test boundary conditions.

The test panels were inspected by C-scan. Panels that were impacted midbay between stringers had only local skin delaminations directly beneath the impact. Panels impacted over the blade or over the flange edge were more likely to delaminate in the first few plies of the skin adjacent to the stringer interface. Such delaminations occurred at the stringer either beneath the impact or near the panel supports. The C-scans of the lateral blade impacts showed delaminations that were strictly confined to the central region of the stringer by the blade, beneath the lateral impact site. In all cases, C-scan aberrations were attributed to delaminations of the composite and not adhesive bond failure.

The smaller peel and pull-off interaction specimens were tested statically until failure. Failure was ultimately caused by skin delamination beneath the edge of the flange.

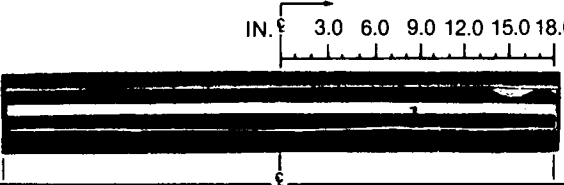

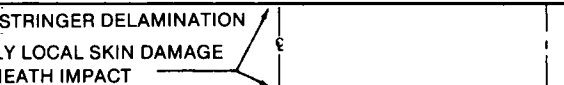
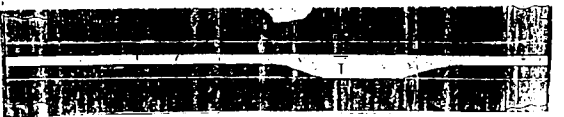
**Two-Stringer Panels** — The two-stringer panel impact results are summarized in Table 8. In test 1A, the delamination occurred in the first few plies at the base of the stringer, above the adhesive layer. This result was not anticipated, because the damage to the panel was sustained at each end, while the impact site was relatively unaffected. It was obvious that the delaminations were caused by excessive interlaminar normal forces generated at each end of the panel. The test setup indicated that the manner in which the panel was supported was conducive to this type of failure under the bending loads resulting from the impact.

**Three-Stringer Panels** — The impact results for three-stringer panels with a flange thickness of 0.23 inch are given in Table 10(B-type). These panels were impacted at midbay and at the middle of the panel over the centerline of the stringer from the cover side. In this case, the panels were supported at the two ends just like clamped edges. In the case of the midbay impact, more damage resulted than for the two-stringer panel. Midstringer impact unexpectedly disbonded the stringer from the skin with peeling of two plies from the skin. Approximately 60 percent of the bonded stringer was separated from the skin. This damage was caused because of the stiffer blade and the rigid boundary conditions.

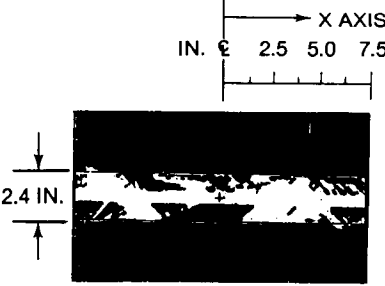
Four three-stringer C-type specimens (Table 11) were impact-tested, and the damage status of the panels was as follows:

1. Panel C1 was impacted over the middle of the center stringer at the outer surface of the panel with 100 ft-lb of energy. The panel was simply supported at the outer edges of the blades as shown in Figure 24b. In this panel, no damage was found either by visual or NDI techniques. To demonstrate the effect of visible (front surface) impact damage on compressive strength, panel C1 was subsequently impacted at 45 degrees with 200 ft-lb of energy using a 1/4-inch-diameter impactor and was redesignated as panel C1'. No trace of any delamination or disbonding was found. The impact with this impactor at midbay caused the desired visible damage, penetrating into the skin.

**Table 9**  
**100-ft-lb Impact Tests and Results for Two-Stringer Panels**

TEST ID	PANEL CONFIGURATION	IMPACT LOCATION	SUPPORT CONDITIONS	C-SCAN OF CENTER STRINGER
1A	REF FIG. 25	REF FIG. 25	REF FIG. 24	
	2-STRINGER, 36-PLY FLANGE	1 OVER- BLADE IMPACT	A CLAMPED ENDS	
2A	2-STRINGER, 36-PLY FLANGE	2 OVER- FLANGE EDGE IMPACT	A CLAMPED ENDS	
3A	2-STRINGER, 36-PLY FLANGE	3 MIDBAY IMPACT	A CLAMPED ENDS	<ul style="list-style-type: none"> <li>• NO STRINGER DELAMINATION</li> <li>• ONLY LOCAL SKIN DAMAGE BENEATH IMPACT</li> </ul> 
4A	2-STRINGER, 36-PLY FLANGE	4 LATERAL BLADE IMPACT	A CLAMPED ENDS	

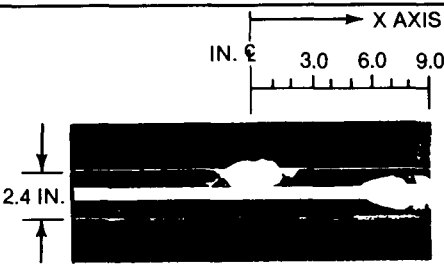
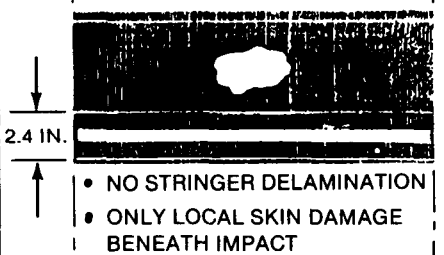
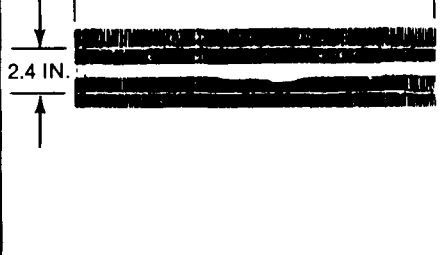
**Table 10**  
**100-ft-lb Impact Tests and Results for B-Type Three-Stringer Panels**

TEST ID	PANEL CONFIGURATION	IMPACT LOCATION	SUPPORT CONDITIONS	C-SCAN OF CENTER STRINGER
B1	REF FIG. 25	REF FIG. 25	REF FIG. 24	
	3-STRINGER, 36-PLY FLANGE	5 OVER-BLADE IMPACT	A CLAMPED ENDS	
B2	3-STRINGER, 36-PLY FLANGE	7 MIDBAY IMPACT	A CLAMPED ENDS	<ul style="list-style-type: none"> <li>• NO STRINGER DELAMINATION</li> <li>• ONLY LOCAL MATRIX DAMAGE BENEATH IMPACT (SIMILAR TO 3A AND C2)</li> </ul>

ORIGINAL PAGE  
BLACK AND WHITE PHOTOGRAPH



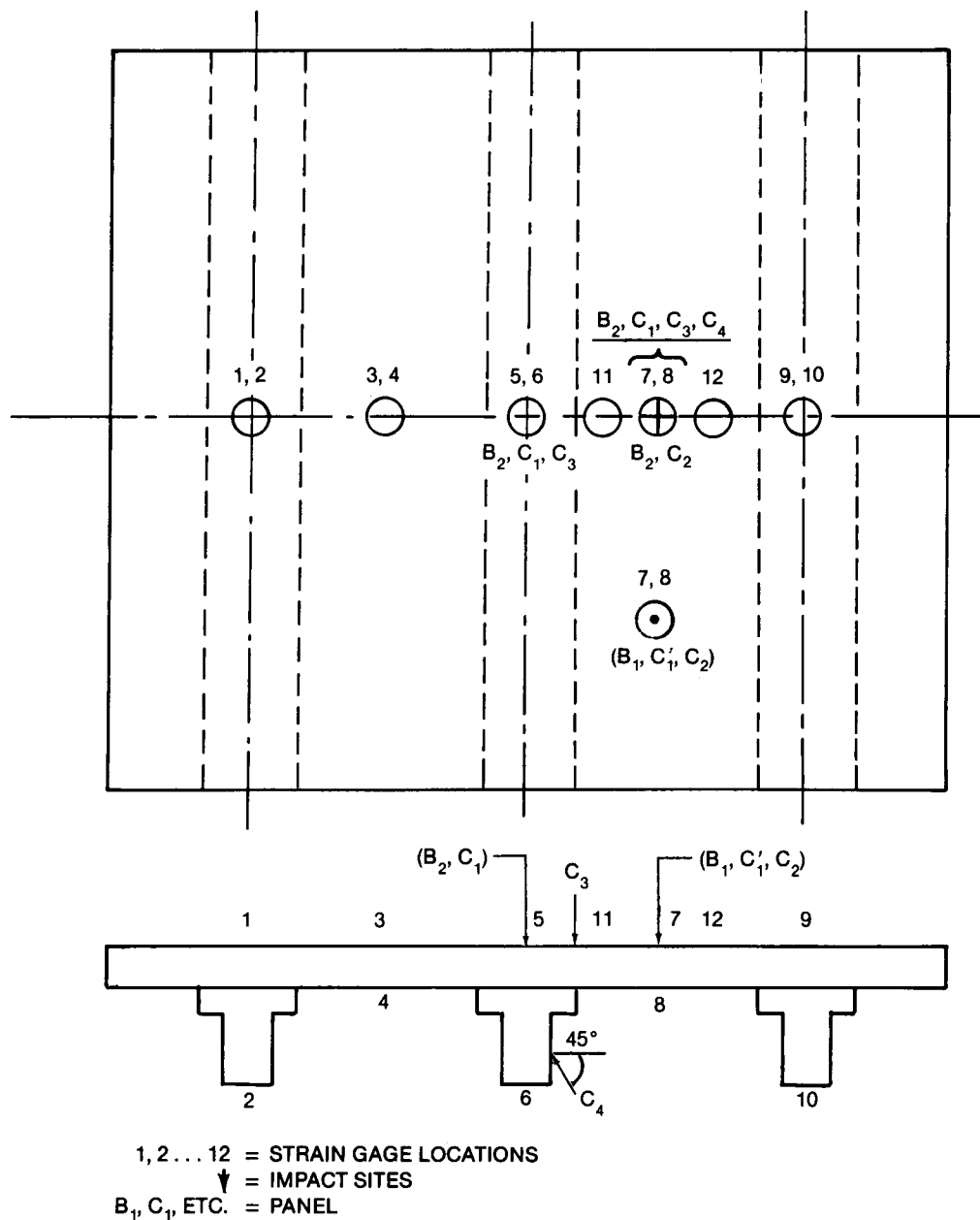
**Table 11**  
**100-ft-lb Impact Tests and Results for C-Type Three-Stringer Panels**

TEST ID	PANEL CONFIGURATION FIG. 25	IMPACT LOCATION FIG. 25	SUPPORT CONDITIONS FIG. 24	C-SCAN OF CENTER STRINGER
C1	3-STRINGER, 18-PLY FLANGE	5 OVER-BLADE IMPACT	B SIMPLE SUPPORT	NO DAMAGE
C3	3-STRINGER, 18-PLY FLANGE	6 OVER- FLANGE EDGE IMPACT	C SIMPLE SUPPORT	
C2	3-STRINGER, 18-PLY FLANGE	7 MIDBAY IMPACT	C SIMPLE SUPPORT	 <ul style="list-style-type: none"> <li>• NO STRINGER DELAMINATION</li> <li>• ONLY LOCAL SKIN DAMAGE BENEATH IMPACT</li> </ul>
C4	3-STRINGER, 18-PLY FLANGE	8 45-DEG LATERAL BLADE IMPACT	D SIMPLE SUPPORT	
C1'	— DO —	MIDBAY IMPACT	C SIMPLE SUPPORT	VISIBLE DAMAGE FIG. 26

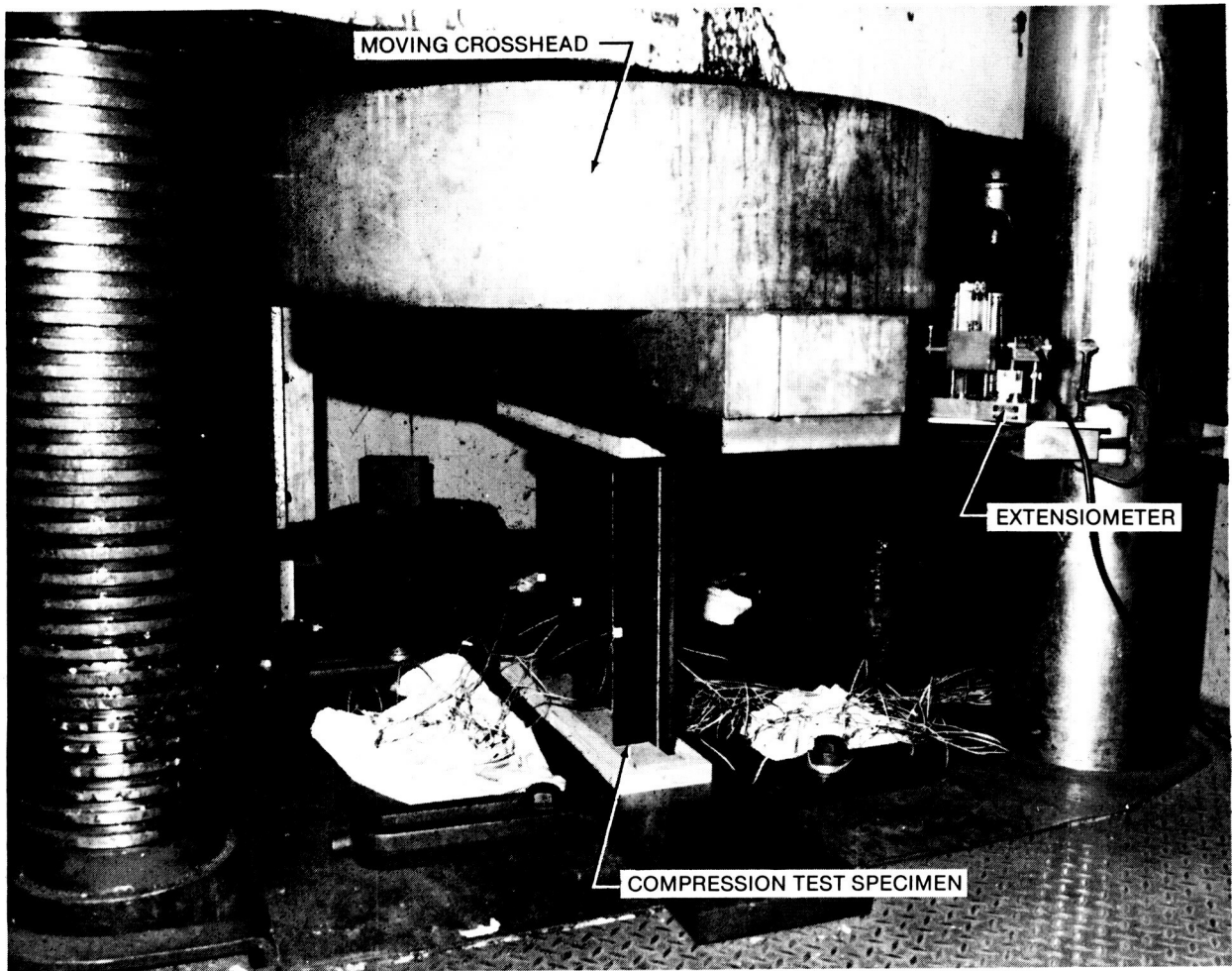
- Panel C2 was impacted at midbay with 100 ft-lb of energy and supported as shown in Figure 24c. There was a visible 2-square-inch delamination on the far side of the panel.
- Panel C3 was impacted at the outer side of the panel near the edge of the middle stringer flange. The panel was supported as shown in Figure 24c. The impact energy of 100 ft-lb produced an approximately 1-1/2-inch delamination and peeling of the flange from the skin near its edge.
- Panel C4 was impacted at the middle of the blade of the center stringer in an inclined (45-degree) fixture, as shown in Figure 24d. The panel was simply supported on its two sides. The panel was also retained at two top corners in the direction normal to the panel to prevent any overturning at the time of impact. The three-stringer panel was impacted at 45 degrees with 200 ft-lb of energy. The panel was debonded about 3.5 inches along the skin and stringer bond line.

**3.3.2.2 Mechanical Tests** — The strain gage and impact locations of all six panels are shown in Figure 26. The locations of gages around the damage areas are offset from the centerline to avoid interference. Three major types of damage (disbonding of inner plies, delamination, and separation of the stringer from the skin) were observed on these panels.

The tests for six three-stringer damage tolerance screening specimens were conducted in the Baldwin test machine (Figure 27) with its capacity of 1.1 million pounds and by uniform end shortening at a rate of 0.02 inch per minute. The data from all strain gages were recorded simultaneously. The results are discussed in Section 5.



**Figure 26. Strain Gage and Impact Locations on Panels**



**Figure 27. Compression Test Setup**

### **3.3.3 Test Plan for Demonstration Panels**

Both panels were impact-tested, and aluminum ribs were attached. The damage was evaluated, and the panels were shipped to NASA Langley, where they were tested.

The panels were potted and machined to correct sizes at the NASA facility. NASA applied 40 gages to the panel with nonvisible damage and 46 gages to the panel with visible damage. The panels were tested under compression to their ultimate strength. The strain gage data acquisition was performed by NASA personnel using a multichannel computer.

ORIGINAL PAGE  
BLACK AND WHITE PHOTOGRAPH

## SECTION 4

### ANALYTICAL DEVELOPMENT

Considerable effort was devoted to developing analytical techniques in the areas of interlaminar stress, delamination growth, peel stress, and residual strength. To understand the disbonding due to impact on stiffened panels for a composite wing, a NASTRAN finite-element model was created, and the interlaminar stresses due to impact loading were determined. The NASTRAN analysis with experimental results has been used to improve the blade flange design.

Delamination due to impact loading and disbonding of the adhesively bonded skin/stringer in the stiffened panel is the vital phenomenon observed in the experimental studies. It is imperative to investigate the delamination growth mechanism under compressive loading and to explore the peel stresses in the skin/stringer interface. A two-dimensional closed-form solution was developed to predict delamination growth using the principle of minimum potential energy. Most of this work was accomplished under an in-house IRAD program. In this case, elliptical delamination was assumed and general plate theory, including bending-extensional coupling, was applied to determine the strain energy release rate components. The effects of various parameters on these components were studied.

A peel stress analysis technique was developed to determine closed-form solutions for peel stress, axial, and out-of-plane displacements. A method based on the point stress criteria was developed to determine the residual strength of an impact-damaged stiffened panel.

#### 4.1 NASTRAN MODEL

For the case of the impact panels studied here, NASTRAN models were created to determine the resulting internal peel moments and pull-off loads. A typical model is illustrated in Figure 28 and is relatively simple. Figure 29 shows a flange edge impact NASTRAN model. The flange and skin are

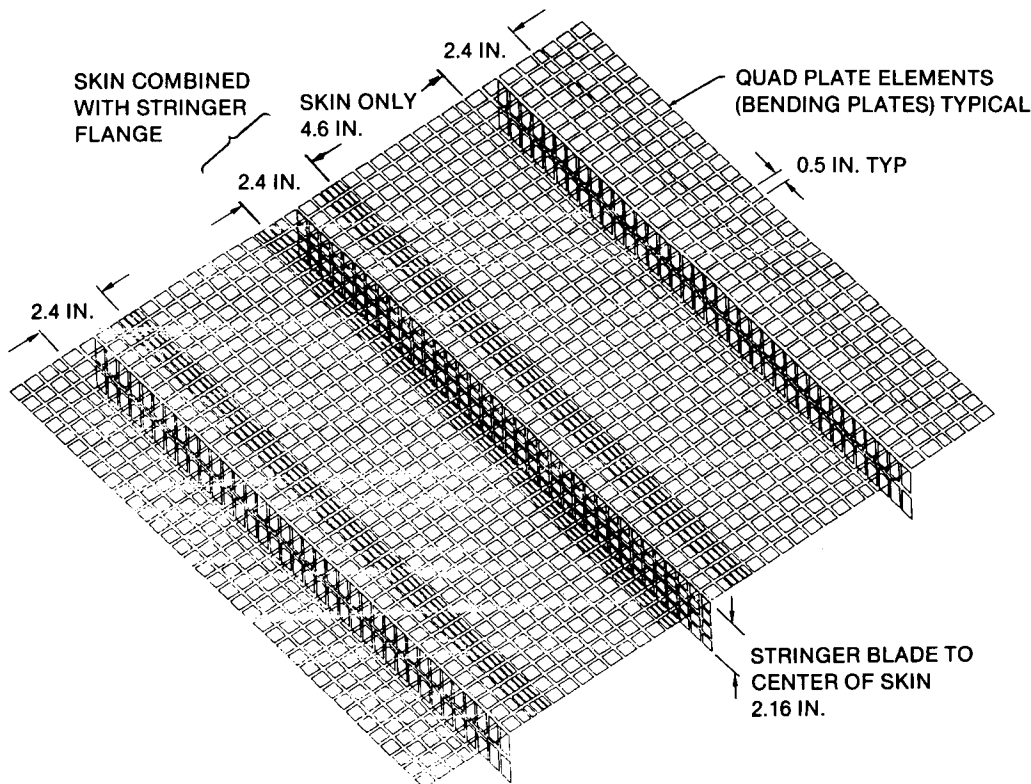
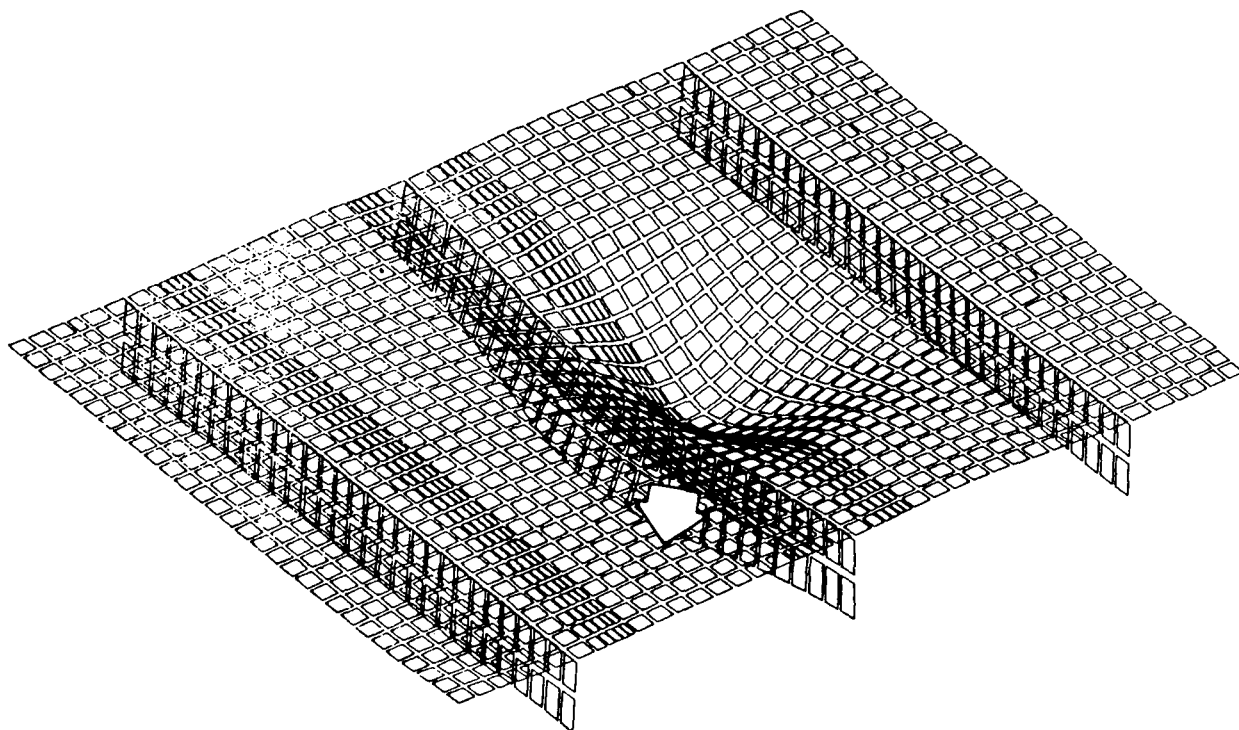


Figure 28. Typical NASTRAN Model of Impact Panels



**Figure 29. NASTRAN Model Analysis for Flange Edge Impact (100 ft-lb) — See Table 10, Test ID C3**

modeled as one element, thereby making no allowance for the bond line. These models were intended to produce internal loads resulting from the beam action of the stringer resisting the applied impacts.

The impact loads were simulated in NASTRAN by using an equivalent static load (Reference 3). This load was determined by the following equation, where  $w$  is the actual weight dropped from height,  $h$ , onto a panel with stiffness,  $k$ .

$$\text{Equivalent Static Load} = [1 + (1 + 2hk/w)^{1/2}]w$$

The stiffness,  $k$ , was determined by first analyzing a unit load case for the NASTRAN models, from which  $k = (\text{unit load})/(\text{deflection for unit load})$  at the impact location. The equivalent static loads were then calculated and used for stress analysis by NASTRAN.

The NASTRAN models were validated by comparing the NASTRAN deflection predicted for two-stringer panel impact test to that measured during a high-speed motion picture of the test. The NASTRAN model predicted a 0.19-inch out-of-plane deflection, which compares well to the 0.21-inch deflection actually measured from the film.

#### **4.1.1 Analysis**

**Failure Mechanism** — There are two types of failure mechanisms — concussive damage and stringer delamination.

**Concussive Damage** — The first type of impact damage seen is the local matrix cracking associated with the direct absorption of the impact energy. This occurred during the midbay impacts, where skin alone had to absorb the impact force. For the impacts over the flange and over the blade, the flange and skin acted together to provide a greater thickness for absorbing the direct impact energy. Therefore, delaminations due to energy absorption did not occur at those locations.

**Stringer Delamination** — This section focuses on the stringer delaminations caused by the internal loads acting in the panel during flexure. These delaminations are seen at various locations along the stringer (Tables 9 through 11).

The analysis of stringer delamination requires identification of the loads and their interactions. The skin delaminations are caused by interlaminar tension stress at the stringer and skin interface. The load that would cause this interfacial tension is a direct pull-off load applied from the stringer blade and a peel moment applied from the skin (Reference 4). A secondary mode of delamination may occur in the radius of the stringer elbow. The responsible load here is primarily the lateral moment at the root of the stringer blade. These loads and their effect on interlaminar stresses are illustrated in Figure 30.

From the NASTRAN internal loads output, pull-off loads and peel moments were determined. Graphs were constructed plotting peel moment versus pull-off load at half-inch intervals along the length of the critical stringer. By considering the separation of delaminated and undamaged data points, an interaction between peel moment and pull-off load was determined. This data point became the intercept for the peel moment axis.

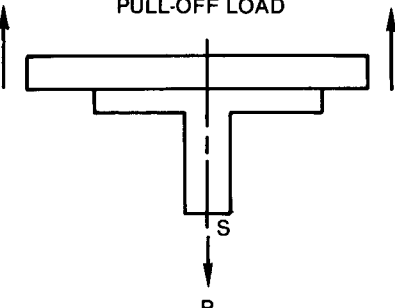
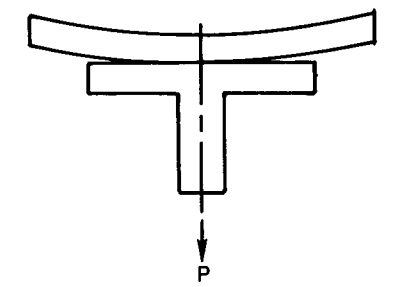
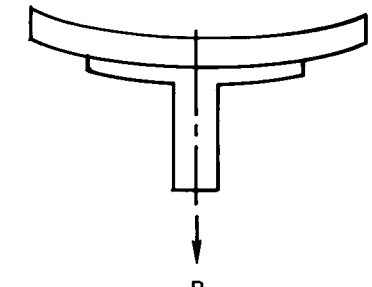
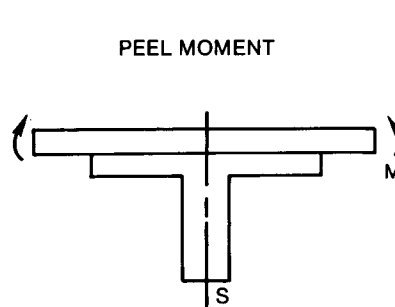
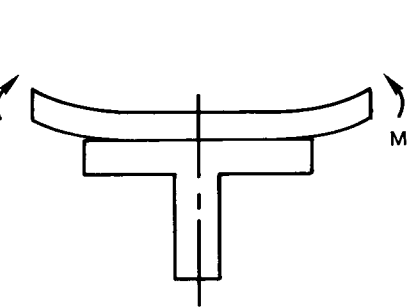
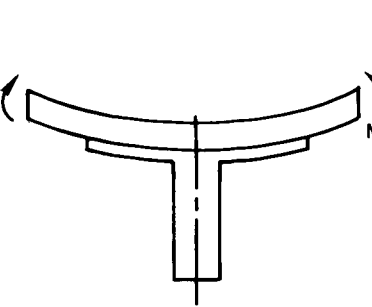
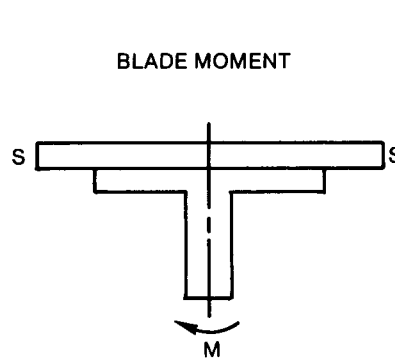
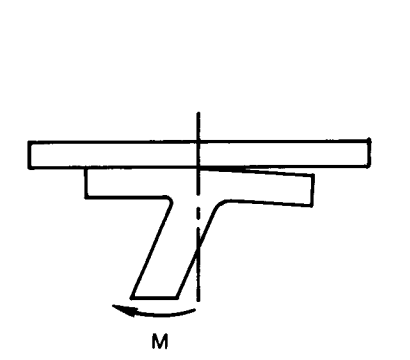
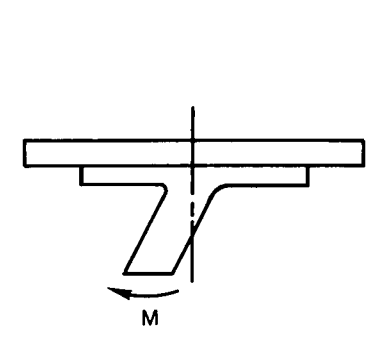
The peel and pull-off behavior identified in Figure 30 provides insight into the shape of the failure envelope. The pull-off load causes high interlaminar stresses beneath the stringer blade, while the peel moment has negligible effect there. Thus, a failure line predicting delamination beneath the blade should be horizontal, involving only pull-off. At the flange edge, however, both the pull-off load and the peel moment have an effect. Thus, a second failure line predicting delamination beneath the flange edge should be sloped to indicate an interaction. The slope should illustrate decreasing pull-off strength with increasing peel stress. (This shape is in accordance with Reference 5.)

The shape of the failure envelope varies with the geometry of the cross section, as shown in Figure 30. (This is supported by Reference 6.) The data were therefore divided into two groups to define separate envelopes for the 36-ply flange and the 18-ply flange cross sections. The delaminated data points identified on the peel versus pull-off charts, and their C-scans were used to help determine whether the delaminations initiated at the flange edge or beneath the blade. The final envelopes derived are shown in Figure 31.

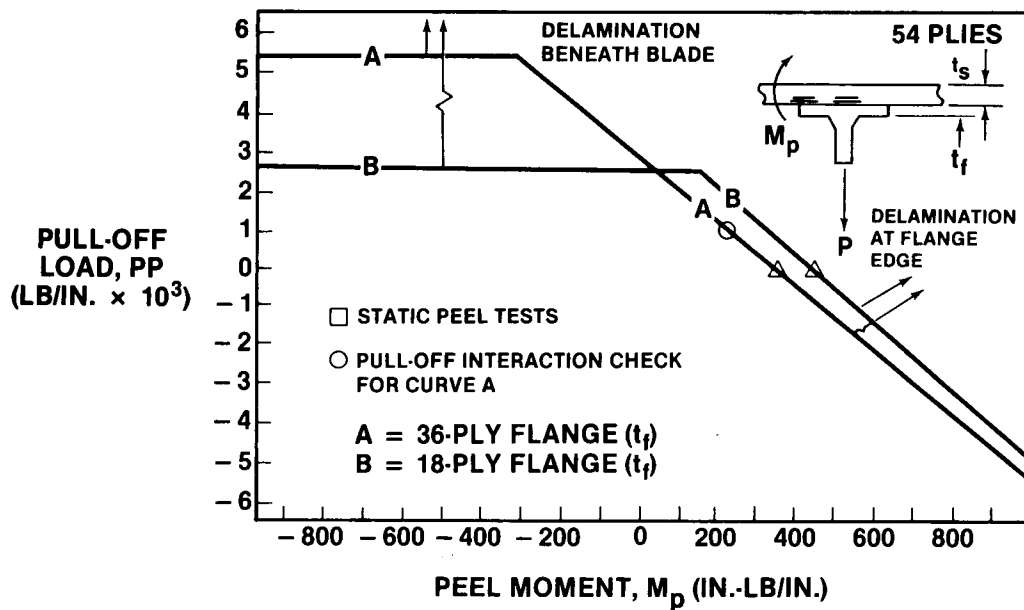
#### **4.1.2 Refined Analysis**

As an additional method to support the trends presented here, a much more detailed set of NASTRAN models was created (Figure 32). These models separated the skin and stringer flange into separate plate elements, connecting them by a model of the adhesive layer. To model the adhesive, a series of shear panels containing shear properties were interspersed with rod elements containing tensile properties. The tensile stresses predicted by these adhesive rods also represent the interlaminar tension in the first few plies adjacent to the adhesive. The magnitudes of the tensile stresses are based on approximate adhesive properties and therefore may be inaccurate, but they qualitatively reinforce the trends previously discussed.

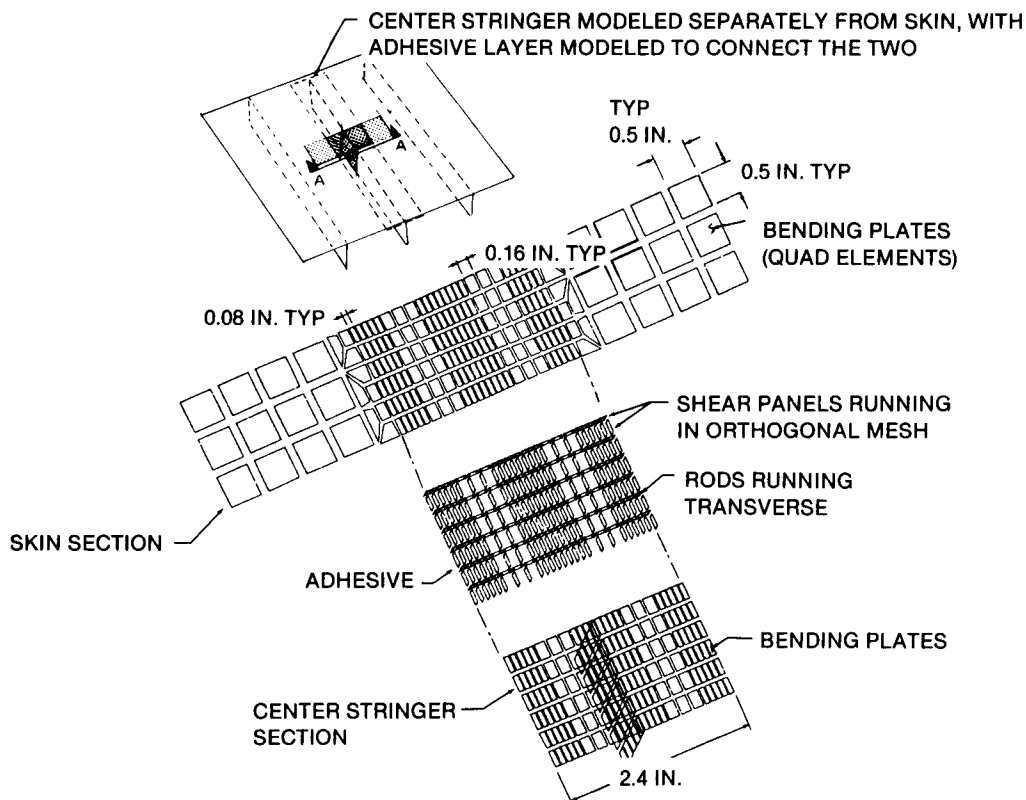
Examples of the NASTRAN interlaminar tensile stress solutions are shown in Figure 33. They correlate well with the critical stress locations given by the peel versus pull-off analysis method, either peaking at

INTERNAL LOAD	EFFECT OF A UNIFORMLY STIFF FLANGE	EFFECT OF A UNIFORMLY FLEXIBLE FLANGE
<p>PULL-OFF LOAD</p>  <p>S: SUPPORTS</p>	 <p>HIGH INTERLAMINAR TENSION UNDER BLADE AT FLANGE EDGE</p>	 <p>HIGHER INTERLAMINAR TENSION UNDER BLADE ONLY</p>
<p>PEEL MOMENT</p>  <p>S: SUPPORTS</p>	 <p>HIGH INTERLAMINAR TENSION AT FLANGE EDGE</p>	 <p>REDUCED INTERLAMINAR TENSION AT FLANGE EDGE SINCE FLEXIBLE FLANGE ATTRACTS LESS LOAD</p>
<p>BLADE MOMENT</p>  <p>S: SUPPORTS</p>	 <p>HIGH INTERLAMINAR RADIAL TENSION IN THE ELBOW</p>	 <p>SIMILAR RESPONSE CAUSING RADIAL ELBOW TENSION</p>

**Figure 30. Comparison of Interlaminar Stresses in Thin (18-Ply) and Thick (36-Ply) Flange Blade Panels**



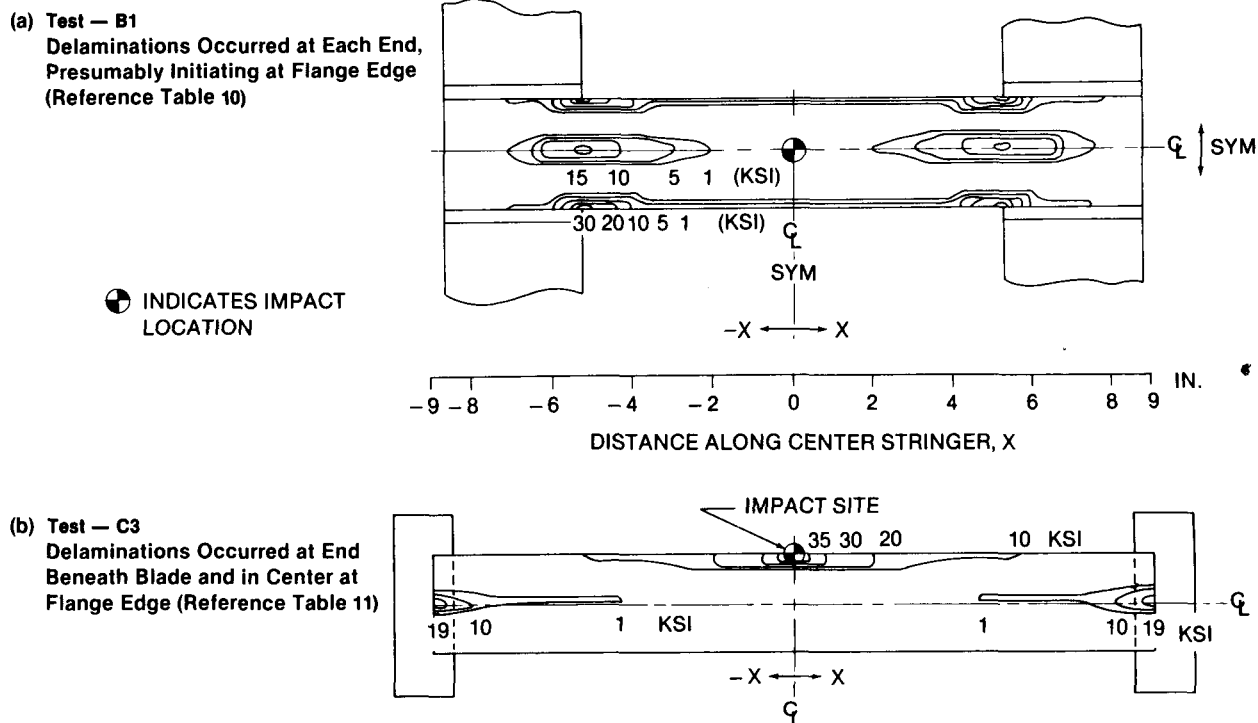
**Figure 31. Peel Moment Versus Pull-Off Load Failure Envelope for Delaminations in Skin at Stringer Interface**



87-DP-8210

**Figure 32. NASTRAN Model with Adhesive Layer**





**Figure 33. Interlaminar Tensile Stress Contours Derived from Refined NASTRAN Model (Reference Figure 32)**

the flange edge or beneath the blade. The highest interlaminar tension stresses also occur in the regions that failed during testing. A series of such models suggests that 18,850 psi would be the interlaminar tension strength for the panels modeled here. The details of the analysis can be found in Reference 7.

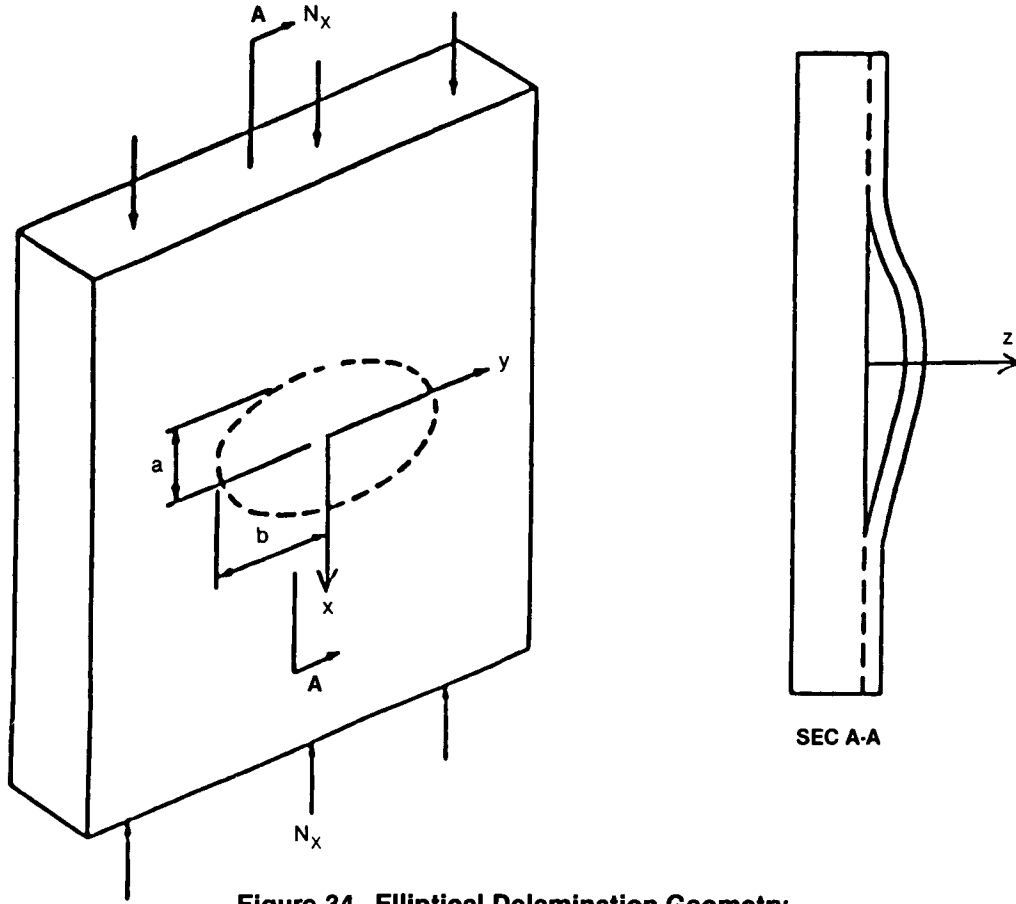
#### 4.1.3 Specimen and Support Conditions

A simplified NASTRAN investigation of the specimen's bending response, and that of the wing structure, indicated that the test support conditions (Figure 24a) were unreasonably overrestrained. The joint bending rigidity offered by the rib supports is quite small in the actual aircraft structure, with less than half of the fixed-end moment being restrained. An investigation of the design revealed that the most rigid (shortest) rib bay could be simulated with a pin-ended specimen 17 to 18 inches long between supports, depending on the impact location. The three-stringer screening specimens were redesigned based on this information.

From NASTRAN analytical investigations, it was clear that the bending stiffness of the flange bonded to the skin plays an important role in the skin/stringer disbonding mechanism. From the results of trial impact tests and NASTRAN models, it was decided to reduce the blade flange thickness from 36 plies (Figure 11) to 18 plies (Figure 12).

## 4.2 DELAMINATION GROWTH — AN APPROXIMATE SOLUTION

This work is based on a thin-film model that has a delamination with an elliptical clamped boundary (Figure 34). As the delamination grows, it maintains its elliptical shape, but with a different aspect ratio. The delamination portion of the laminate on the sublaminates is thin compared with the parent laminate;



**Figure 34. Elliptical Delamination Geometry**

i.e., the parent laminate does not bend. The in-plane deflections at the boundary of the delamination are determined by the strains in the parent laminate. The out-of-plane deflection of the elliptical plate is expressed as:

$$w = a C'_1 (1 - \bar{x}^2 - \bar{y}^2)^2 \quad (1)$$

where

$$\bar{x} = x/a, \bar{y} = y/b, \text{ and } C'_1 \text{ is an arbitrary constant.}$$

The in-plane displacements are given by:

$$dx = \epsilon_{ox} ra \quad \text{where} \quad [r = (1 - \bar{y}^2)^{1/2}] \quad (2)$$

$$dy = \epsilon_{oy} sb \quad \text{where} \quad [s = (1 - \bar{x}^2)^{1/2}]$$

$\epsilon_{ox}$  = critical buckling strain of ellipse.

$$\epsilon_{oy} = -\nu \epsilon_{ox}$$

The in-plane membrane deflections  $u$  and  $v$  are functions of  $w$ .

$$u = (\epsilon_{ox} + C_1^2 r^6) xa$$

$$v = (-\nu \epsilon_{ox} + C_1^2 \alpha^2 s^6) yb \quad \text{where } \alpha = a/b \quad (3)$$

The total strain energy U of the region S is

$$U = \frac{1}{2} \int_{-1}^1 \int_{-r}^r (\epsilon^T A \epsilon + 2\epsilon^T B K + K^T D K) dx dy + (S - \pi ab) (A_{11} - 2\nu A_{12} + \nu^2 A_{22}) \epsilon_{ox}^2 \quad (4)$$

where

$$\begin{aligned} \epsilon^T &= (u_{,x}, v_{,y}, u_{,y} + v_{,x}) \\ K^T &= (-w_{,xx}, -w_{,yy}, -2w_{,xy}) \end{aligned} \quad (5)$$

A, B, and D refer to the constituent matrices of the delaminated sublaminates. S is the total area of the laminate including delamination.

The strain energy release rate for changes in the a and b dimensions of the ellipse are defined as

$$G_a = -\frac{1}{\pi b} \frac{\delta U}{\delta a} \text{ and } G_b = -\frac{1}{\pi a} \frac{\delta U}{\delta b} \quad (6)$$

for i = a, b

$$\begin{aligned} G_i &= \frac{i}{\pi ab} \left[ \frac{1}{2} C_1^4 f_{4,i} + 2 C_1^3 f_4 C_{1,i} + C_1^3 f_{3,i} + 3 C_1^2 f_3 g_i \right. \\ &\quad \left. + C_1^2 (f_{2,i} \epsilon_{ox} + f_{1,i}) + 2 C_1 (f_2 \epsilon_{ox} + f_1) C_{1,i} \right] \end{aligned} \quad (7)$$

$$\begin{aligned} C_{1,i} &= \frac{\partial C_1}{\partial i} = [-3 f_{3,i} + 9 f_3 f_{3,i} - 8 f_{4,i} (f_2 \epsilon_{ox} + H) \\ &\quad - 8 f_4 (f_{2,i} \epsilon_{ox} + f_{1,i})] f_4 / f + f_{4,i} (3 f_3 - g) / 4 f_4^2 \end{aligned} \quad (8)$$

where

$$g = [9 f_3^2 - 16 f_4 (f_2 \epsilon_{ox} + f_1)]^{1/2} \quad (9)$$

$$\begin{aligned} U &= \frac{C_1^4}{2} f_4 + C_1^3 f_3 + C_1^2 (f_2 \epsilon_{ox} + f_1) + \frac{1}{2} f_0 \epsilon_{ox}^2 \\ &\quad + \frac{1}{2} (S - \pi ab) (A_{11} - 2\nu A_{12} + \nu^2 A_{22}) \epsilon_{ox}^2 \end{aligned} \quad (10)$$

$$C_1' = 1.28 C_1$$

$$f_0 = \pi ab (A_{11} - 2\nu A_{12} + \nu^2 A_{22}) \quad (11)$$

$$f_1 = 20.617 (D_{11} + 0.667 \alpha^2 D_{12} + \alpha^4 D_{22} + 1.333 \alpha^2 D_{66}) / \alpha \quad (12)$$

$$f_2 = 1.718 ab [A_{11} - \nu \alpha^2 A_{22} + (\alpha^2 - \nu) A_{12}] \quad (13)$$

$$f_3 = 14.085 a \alpha (B_{12} - 2B_{66}) \quad (14)$$

$$f_4 = ab [1.31624 (A_{11} + \alpha^4 A_{22}) + 1.6684 \alpha^2 A_{12} + 3.883 \alpha^2 A_{66}] \quad (15)$$

Minimum potential energy is obtained by differentiating Equation (4) with respect to  $C_1'$  and setting the resulting relation to zero. This relation is the characteristic equation that is used to calculate the critical compressive strain,  $\epsilon_{xcr}$

$$\epsilon_{xcr} = \frac{9f_3^2}{16f_2f_4} - \frac{f_1}{f_2} \quad (16)$$

$$C_1 = 0.32(g - 3f_3)/f_4 \quad (17)$$

Plots of  $G_a$  and  $G_b$  for a typical laminate (Figure 35) show that for near-circular delaminations  $G_b$  is greater than  $G_a$ , i.e., the tendency for the delamination to progress laterally is greater than its tendency to progress in the direction of the load. Also note that for small delaminations, as  $b/a$  increases beyond 2,  $G_a$  becomes greater than  $G_b$ , which tends to recircularize the delamination. But at the same time, as  $a$  (or the size of the delamination) becomes larger,  $G_a$  approaches zero and  $G_b$  approaches a constant value. Thus, the delamination growth is stable.

The effect of the material  $G_{IC}$  on the parameter  $G_b$  and on the critical strain at which the delamination will propagate is shown in Figures 36 and 37. Clearly, it is advantageous to have a high value of  $G_{IC}$  in the laminate.

The sensitivity of the parameter  $G_b$  to the depth of the delamination plane is shown in Figure 38. The effects can vary depending on the size of the initial delamination. However, for the size of impact damage likely to occur in the new toughened system, the deeper delaminations are generally less critical than those toward the surface.

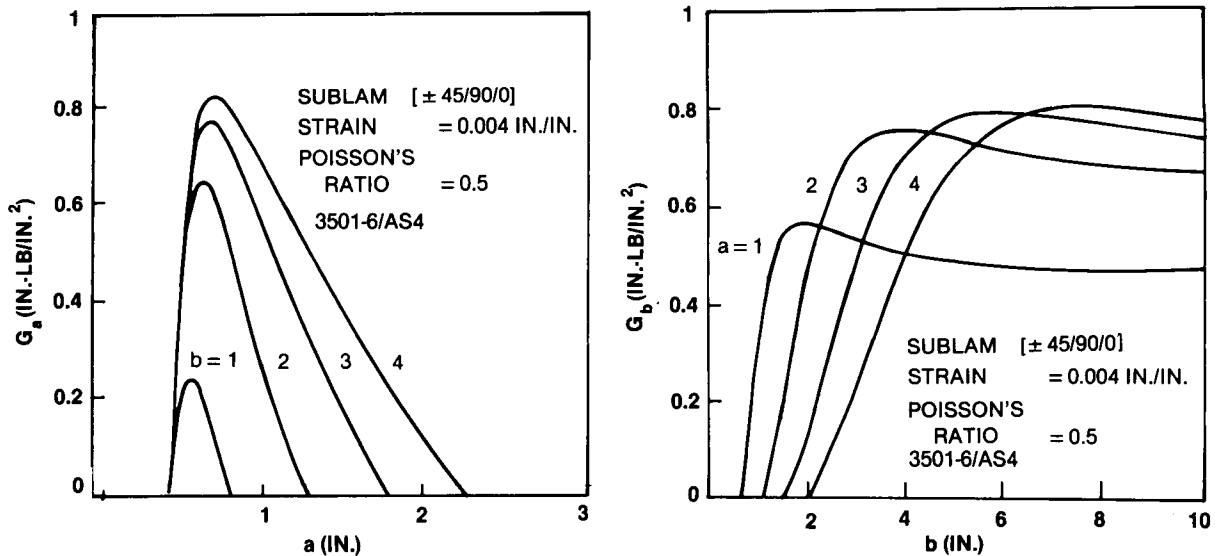


Figure 35. Variation of  $G_a$  and  $G_b$  with  $a$  and  $b$

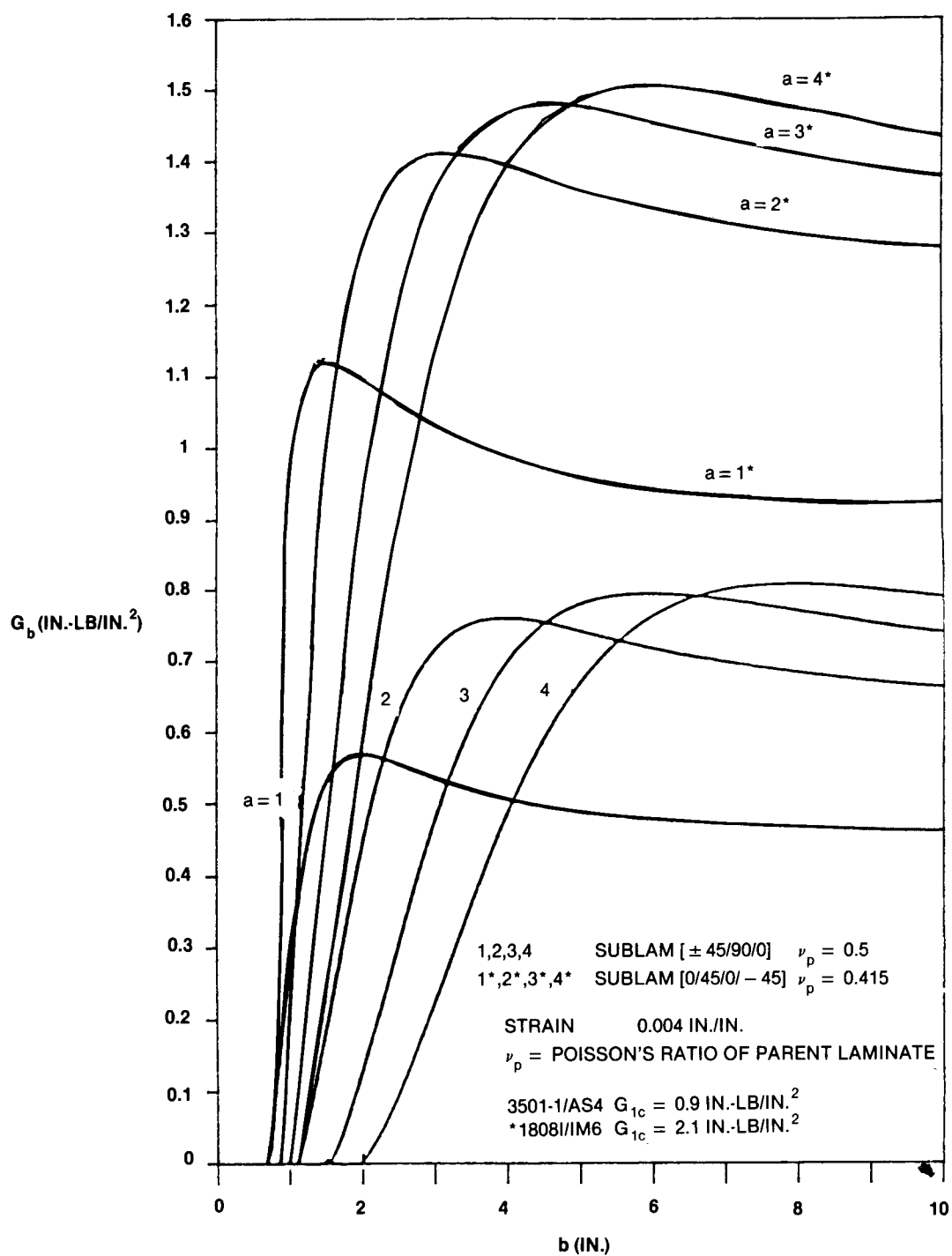


Figure 36. Sensitivity of  $G_b$  to Material Property  $G_{1c}$

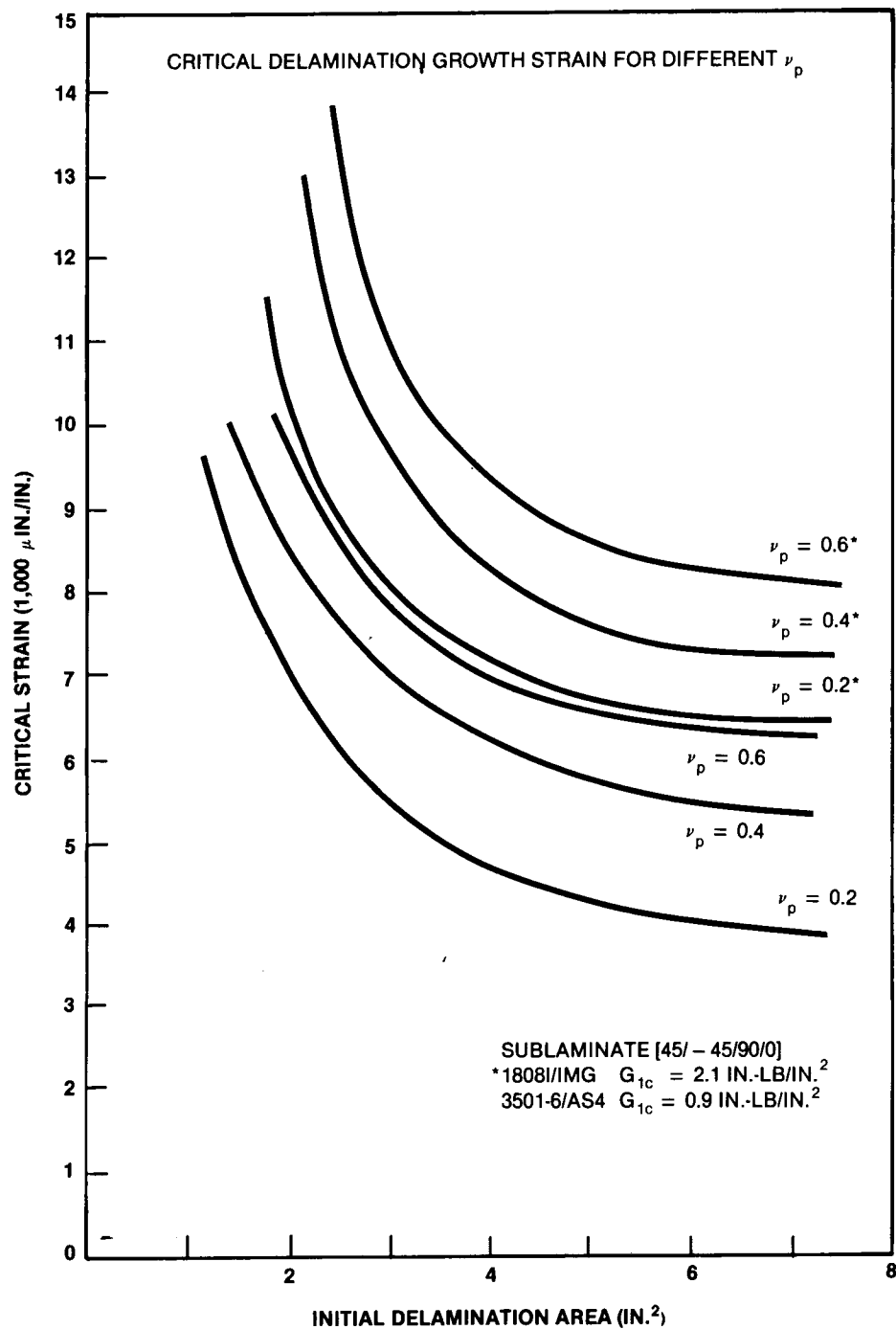


Figure 37. Sensitivity of Critical Delamination Growth Strain to the Material Property  $G_{1c}$

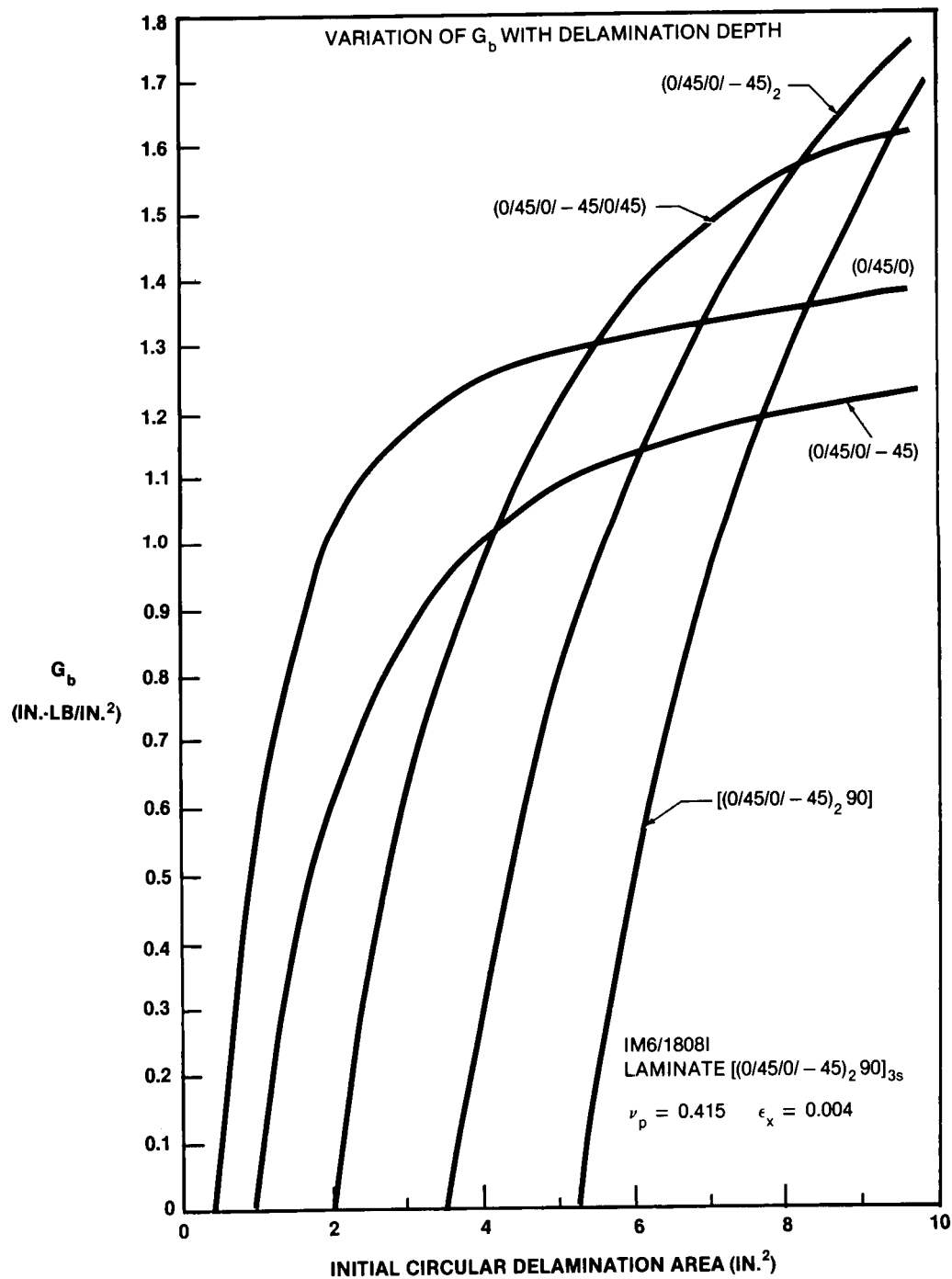


Figure 38. Sensitivity of Parameter  $G_b$  to the Depth of the Delamination Plane

### 4.3 PEEL STRESS ANALYSIS

Bonded stiffened panels are being used more widely in the aerospace industry because of their lighter weight and fewer parts. Various authors have developed methods for analyzing the stresses in the adhesive between two bonded plates (References 8 and 9). However, a simpler method was needed to calculate these stresses in bonded stiffened panels, so that the designer could evaluate the relative importance of adhesive and adherend properties in determining the stresses.

Under this program, a closed-form solution was obtained for the stresses and displacements of two bonded beams. A system of two fourth-order and two second-order differential equations with the associated boundary equations was determined using a variational work approach. A FORTRAN computer program was devised to solve for the eigenvalues and eigenvectors of this system and calculate the coefficients from the boundary conditions. The results were then compared with NASTRAN finite-element solutions and were shown to agree closely.

#### 4.3.1 Analysis

The model analyzed is shown in Figure 39. The upper and lower members are beams of unit width, and the effect of the stringer blade is disregarded. In this analysis, subscripts 1 and 2 refer to upper and lower beams, respectively, and subscript c refers to the adhesive. In addition to assuming beam behavior and small deflections, the adhesive is assumed to be linearly elastic and of constant thickness. The restraint on the adhesive provided by the two beams prevents Poisson's contraction, making the assumption of linear elasticity a reasonable one.

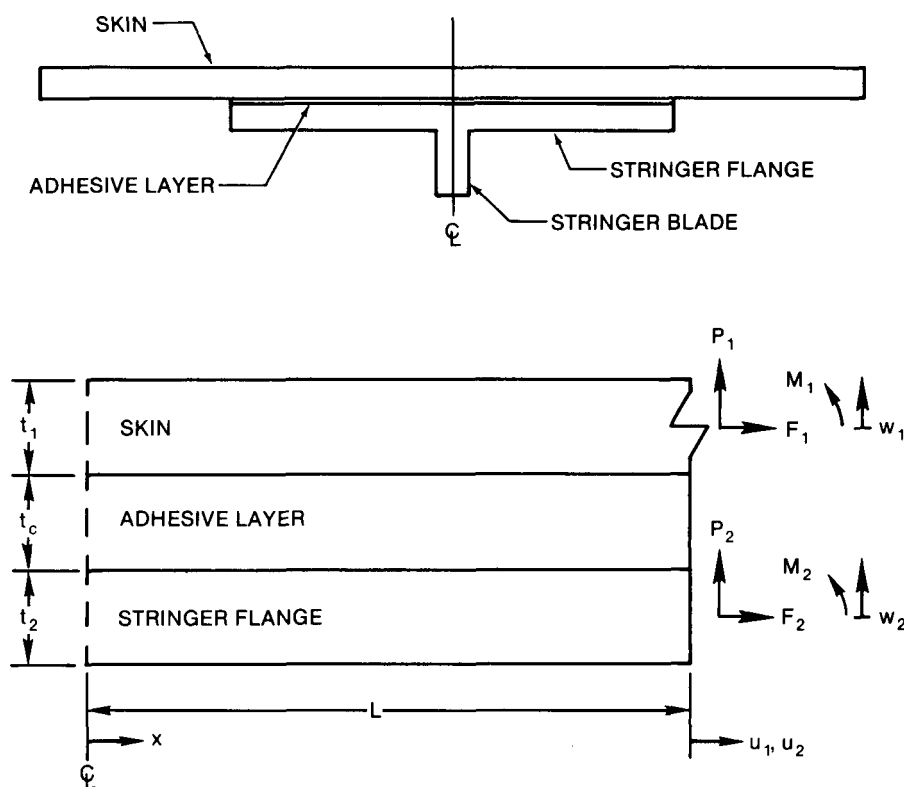


Figure 39. Model Used for Analysis



An expression for shear stress in the adhesive,  $\tau_c$ , which takes into account the differences in rotation and elongation between the two beams, is:

$$\tau_c = G_c[2(u_1 - u_2) + D_1 T_1 dw_1/dx + D_2 T_2 dw_2/dx]/2t_c \quad (18)$$

where

$$T_1 = (t_1 + t_c)/D_1 \quad T_2 = (t_2 + t_c)/D_2$$

Using this expression, strain energy of the adhesive shear ( $U_G$ ) can be added to the contributions of strain energies of adhesive stretching ( $U_E$ ), beam stretching of skin and stringer ( $U_{S1}$ ,  $U_{S2}$ ), and beam bending of skin and stringer ( $U_{B1}$ ,  $U_{B2}$ ).

$$U = U_G + U_E + U_{S1} + U_{S2} + U_{B1} + U_{B2} \quad (19)$$

For total potential energy:

$$V = - (P_1 w_1 + P_2 w_2 + M_1 dw_1/dx + M_2 dw_2/dx + F_1 u_1 + F_2 u_2)|_{x=L} + 1/2 \int_0^L (F_1 (dw_1/dx)^2 + F_2 (dw_2/dx)^2) dx \quad (20)$$

$$\pi = U + V \quad (21)$$

Using the principle of minimum potential energy:

$$\delta\pi = \delta U + \delta V = 0 \quad (22)$$

Substituting  $\bar{w}_1 = w_1 D_1$ ,  $\bar{w}_2 = w_2 D_2$ ,  $\bar{u}_1 = u_1 E_1 t_1$ , and  $\bar{u}_2 = u_2 E_2 t_2$  yields the following expression for  $\delta\pi$ :

$$\begin{aligned} \delta\pi = \int_0^L & \left[ (G_c/2t_c) \{ 2(\bar{u}_1/\bar{E}_1 - \bar{u}_2/\bar{E}_2) + T_1 d\bar{w}_1/dx + T_2 d\bar{w}_2/dx \} \right. \\ & \cdot \delta(\bar{u}_1/\bar{E}_1 - \bar{u}_2/\bar{E}_2) + E_c/t_c \cdot (\bar{w}_1/D_1 - \bar{w}_2/D_2) \\ & \cdot \delta(\bar{w}_1/D_1 - \bar{w}_2/D_2) + (G_c/4t_c) \{ 2(\bar{u}_1/\bar{E}_1 - \bar{u}_2/\bar{E}_2) + T_1 d\bar{w}_1/dx + T_2 d\bar{w}_2/dx \} \\ & \cdot \delta(T_1 d\bar{w}_1/dx + T_2 d\bar{w}_2/dx) + 1/\bar{E}_1 \cdot d\bar{u}_1/dx \cdot \delta(d\bar{u}_1/dx) \cdot d\bar{u}_1/dx \cdot \delta(d\bar{u}_1/dx) \\ & + 1/\bar{E}_2 \cdot d\bar{u}_2/dx \cdot \delta(d\bar{u}_2/dx) + F_1/D_1^2 \cdot d\bar{w}_1/dx \cdot \delta(d\bar{w}_1/dx) \\ & + F_2/D_2^2 \cdot d\bar{w}_2/dx \cdot \delta(d\bar{w}_2/dx) \\ & + 1/D_1 \cdot d^2\bar{w}_1/dx^2 \cdot \delta(d^2\bar{w}_1/dx^2) + 1/D_2 \cdot d^2\bar{w}_2/dx^2 \cdot \delta(d^2\bar{w}_2/dx^2) \Big] dx \\ & - [P_1/D_1 \cdot \delta\bar{w}_1 + P_2/D_2 \cdot \delta\bar{w}_2 + M_1/D_1 \cdot \delta(d\bar{w}_1/dx) + M_2/D_2 \cdot \delta(d\bar{w}_2/dx) \\ & + F_1/\bar{E}_1 \cdot \delta\bar{u}_1 + F_2/\bar{E}_2 \cdot \delta\bar{u}_2] |_{x=L} \end{aligned} \quad (23)$$

where

$$\bar{E}_1 = \bar{E}_1 t_1, \bar{E}_2 = E_2 t_2$$

Integration by parts to eliminate differentials from the variational terms and grouping according to variational terms yield 12 boundary conditions and a system of two fourth-order and two second-order differential equations.

### Boundary Conditions

At the centerline ( $x = 0$ ), the stringer flange is clamped while the skin is free to translate but not rotate. At the free edge of the skin and stringer flange, the applied forces and moments are related to displacement as follows:

$$\begin{aligned} d\bar{u}_1/dx = F_1 \quad d\bar{u}_2/dx = F_2 \quad d^2\bar{w}_1/dx^2 = M_1 \quad d^2\bar{w}_2/dx^2 = M_2 \end{aligned} \quad (24)$$

$$\begin{aligned} G_c T_1 D_1 [T_1 d\bar{w}_1/dx + T_2 d\bar{w}_2/dx + 2(\bar{u}_1/\bar{E}_1 - \bar{u}_2/\bar{E}_2)]/4t_c \\ + F_1/D_1 \cdot d\bar{w}_1/dx - d^3\bar{w}_1/dx^3 = P_1 \end{aligned} \quad (25)$$

$$\begin{aligned} G_c T_2 D_2 [T_1 d\bar{w}_1/dx + T_2 d\bar{w}_2/dx + 2(\bar{u}_1/\bar{E}_1 - \bar{u}_2/\bar{E}_2)]/4t_c \\ + F_2/D_2 \cdot d\bar{w}_2/dx - d^3\bar{w}_2/dx^3 = P_2 \end{aligned} \quad (26)$$

### System of Differential Equations

$$\begin{aligned} A (\bar{w}_1/D_1 - \bar{w}_2/D_2) - G_c T_1 [T_1 d^2\bar{w}_1/dx^2 + T_2 d^2\bar{w}_2/dx^2 \\ + 2(d\bar{u}_1/dx \cdot 1/\bar{E}_1 - d\bar{u}_2/dx \cdot 1/\bar{E}_2)]/4t_c - F_1/D_1 \cdot d^2\bar{w}_1/dx^2 + 1/D_1 \cdot d^4\bar{w}_1/dx^4 = 0 \end{aligned} \quad (27)$$

$$\begin{aligned} -B(\bar{w}_1/D_1 - \bar{w}_2/D_2) - G_c T_2 [T_1 d^2\bar{w}_1/dx^2 + T_2 d^2\bar{w}_2/dx^2 \\ + 2(d\bar{u}_1/dx \cdot 1/\bar{E}_1 - d\bar{u}_2/dx \cdot 1/\bar{E}_2)]/4t_c - F_2/D_2 \cdot d^2\bar{w}_2/dx^2 + 1/D_2 \cdot d^4\bar{w}_2/dx^4 = 0 \end{aligned} \quad (28)$$

$$E [T_1 d\bar{w}_1/dx + T_2 d\bar{w}_2/dx + 2(\bar{u}_1/\bar{E}_1 - \bar{u}_2/\bar{E}_2)] - d^2\bar{u}_1/dx^2 = 0 \quad (29)$$

$$E [T_1 d\bar{w}_1/dx + T_2 d\bar{w}_2/dx + 2(\bar{u}_1/\bar{E}_2 - \bar{u}_2/\bar{E}_2)] + d^2\bar{u}_2/dx^2 = 0 \quad (30)$$

Differentiating Equations (29) and (30) once with respect to  $x$  and substituting  $\bar{u}_3 = d\bar{u}_1/dx$ ,  $\bar{u}_4 = d\bar{u}_2/dx$ ,  $\bar{w}_3 = d^2\bar{w}_1/dx^2$ , and  $\bar{w}_4 = d^2\bar{w}_2/dx^2$  gives a system of six second-order equations, which can be written in matrix form:

$$\begin{bmatrix} 0 & 0 & 1 & 0 & 0 & 0 \\ 0 & 0 & 0 & 1 & 0 & 0 \\ -A & B & CT_1 + F_1/D_1 & CT_2 & CF & -CG \\ A & -B & DT_1 & DT_2 + F_2/D_2 & DF & -DG \\ 0 & 0 & ET_1 & ET_2 & EF & -EG \\ 0 & 0 & -ET_1 & -ET_2 & -EF & EG \end{bmatrix} \begin{bmatrix} \bar{w}_1 \\ \bar{w}_2 \\ \bar{w}_3 \\ \bar{w}_4 \\ \bar{u}_3 \\ \bar{u}_4 \end{bmatrix} = \begin{bmatrix} d^2\bar{w}_1/dx^2 \\ d^2\bar{w}_2/dx^2 \\ d^2\bar{w}_3/dx^2 \\ d^2\bar{w}_4/dx^2 \\ d^2\bar{u}_3/dx^2 \\ d^2\bar{u}_4/dx^2 \end{bmatrix} \quad (31)$$

where

$$\begin{aligned} A &= E_c/t_c D_1 & B &= E_c/t_c D_2 & C &= G_c T_1 D_1/4t_c \\ D &= G_c T_2 D_2/4t_c & E &= G_c/2t_c & F &= 1/\bar{E}_1 \\ G &= 1/\bar{E}_2 \end{aligned}$$

The characteristic equation for this system is defined by  $|M - \lambda I| = 0$ , where  $M$  is the matrix of coefficients of the system and  $I$  is the identity matrix. For this case, the characteristic equation is:

$$\begin{aligned} 0 &= \lambda^4 - [CT_1 + DT_2 + F_1/D_1 + F_2/D_2 + E(F + G)]\lambda^3 \\ &+ [A + B + CT_1 F_2/D_2 + DT_2 F_1/D_1 + F_1/D_1 \cdot F_2/D_2 \\ &+ E(F + G)(F_1/D_1 + F_2/D_2)]\lambda^2 - [(A + B + F_1/D_1 \cdot F_2/D_2)E(F + G) \\ &+ (C + D)(AT_2 + BT_1) + BF_1/D_1 + AF_2/D_2]\lambda + E(F + G)(AF_2/D_2 + BF_1/D_1) \end{aligned} \quad (32)$$

This gives two cases, one with in-plane forces and one without. For the first case, the solutions to the characteristic equation are  $(\lambda_1, \lambda_2, \lambda_3, \lambda_4, 0, 0)$ . For the second case, the solutions are  $(\lambda_1, \lambda_2, \lambda_3, 0, 0, 0)$ .

### Case 1 (with In-Plane Force)

For this case,  $\bar{w}_1$  can be expressed as follows:

$$\begin{aligned} \bar{w}_1 &= C_1 e^{\mu_1 x} + C_2 e^{-\mu_1 x} + C_3 e^{\mu_2 x} + C_4 e^{-\mu_2 x} + C_5 e^{\mu_3 x} + C_6 e^{-\mu_3 x} \\ &+ C_7 e^{\mu_4 x} + C_8 e^{-\mu_4 x} + C_9 x^3 + C_{10} x^2 + C_{11} x + C_{12} \end{aligned} \quad (33)$$

where  $\mu_i = \sqrt{\lambda_i}$ .

Putting this expression into Equations (27) through (30), it can be shown that the  $x^3$  and  $x^2$  terms disappear and  $\bar{w}_1$ ,  $\bar{w}_2$ ,  $\bar{u}_1$ , and  $\bar{u}_2$  can be expressed as:

$$\begin{aligned} \bar{w}_1 &= C_1 e^{\mu_1 x} + C_2 e^{-\mu_1 x} + C_3 e^{\mu_2 x} + C_4 e^{-\mu_2 x} + C_5 e^{\mu_3 x} + C_6 e^{-\mu_3 x} \\ &+ C_7 e^{\mu_4 x} + C_8 e^{-\mu_4 x} + C_9 x + C_{10} \end{aligned} \quad (34)$$

$$\begin{aligned} \bar{w}_2 &= U_{21}(C_1 e^{\mu_1 x} + C_2 e^{-\mu_1 x}) + U_{22}(C_3 e^{\mu_2 x} + C_4 e^{-\mu_2 x}) \\ &+ U_{23}(C_5 e^{\mu_3 x} + C_6 e^{-\mu_3 x}) + U_{24}(C_7 e^{\mu_4 x} + C_8 e^{-\mu_4 x}) + A/B \cdot (C_9 x + C_{10}) \end{aligned} \quad (35)$$

$$\begin{aligned} \bar{u}_1 &= U_{51}(C_1 e^{\mu_1 x} - C_2 e^{-\mu_1 x})/\mu_1 + U_{52}(C_3 e^{\mu_2 x} - C_4 e^{-\mu_2 x})/\mu_2 \\ &+ U_{53}(C_5 e^{\mu_3 x} - C_6 e^{-\mu_3 x})/\mu_3 + U_{54}(C_7 e^{\mu_4 x} - C_8 e^{-\mu_4 x})/\mu_4 + C_{11} x + C_{13} \end{aligned} \quad (36)$$

$$\begin{aligned} \sigma_1 &= [U_{51}(C_1 e^{\mu_1 x} + C_2 e^{-\mu_1 x}) + U_{52}(C_3 e^{\mu_2 x} + C_4 e^{-\mu_2 x}) \\ &+ U_{53}(C_5 e^{\mu_3 x} + C_6 e^{-\mu_3 x}) + U_{54}(C_7 e^{\mu_4 x} + C_8 e^{-\mu_4 x})]/t_1 + C_{11} \end{aligned} \quad (37)$$

$$\bar{u}_2 = - \left[ U_{51}(C_1 e^{\mu_1 x} - C_2 e^{-\mu_1 x})/\mu_1 - U_{52}(C_3 e^{\mu_2 x} - C_4 e^{-\mu_2 x})/\mu_2 + U_{53}(C_5 e^{\mu_3 x} - C_6 e^{-\mu_3 x})/\mu_3 - U_{54}(C_7 e^{\mu_4 x} - C_8 e^{-\mu_4 x})/\mu_4 \right] + C_{12}x + C_{14} \quad (38)$$

$$\sigma_2 = - \left[ U_{51}(C_1 e^{\mu_1 x} + C_2 e^{-\mu_1 x}) - U_{52}(C_3 e^{\mu_2 x} + C_4 e^{-\mu_2 x}) + U_{53}(C_5 e^{\mu_3 x} + C_6 e^{-\mu_3 x}) - U_{54}(C_7 e^{\mu_4 x} + C_8 e^{-\mu_4 x}) \right] / t_2 + C_{12} \quad (39)$$

$$C_{12} = FC_{11}/G \text{ and } C_{14} = [(T_1 + T_2 A/B)C_9 + FC_{13}]/G \quad (40)$$

### Case 2 (without In-Plane Force)

For this case,  $\bar{w}_1$  can be expressed as follows:

$$\bar{w}_1 = C_1 e^{\mu_1 x} + C_2 e^{-\mu_1 x} + C_3 e^{\mu_2 x} + C_4 e^{-\mu_2 x} + C_5 e^{\mu_3 x} + C_6 e^{-\mu_3 x} + C_7 x^5 + C_8 x^4 + C_9 x^3 + C_{10} x^2 + C_{11} x + C_{12} \quad (41)$$

Putting this expression into Equations (27) through (30), it can be shown that the  $x^5$  and  $x^4$  terms disappear and  $w_1$ ,  $w_2$ ,  $u_1$ , and  $u_2$  can be expressed as:

$$\bar{w}_1 = C_1 e^{\mu_1 x} + C_2 e^{-\mu_1 x} + C_3 e^{\mu_2 x} + C_4 e^{-\mu_2 x} + C_5 e^{\mu_3 x} + C_6 e^{-\mu_3 x} + C_7 x^3 + C_8 x^2 + C_9 x + C_{10} \quad (42)$$

$$\bar{w}_2 = U_{21}(C_1 e^{\mu_1 x} + C_2 e^{-\mu_1 x}) + U_{22}(C_3 e^{\mu_2 x} + C_4 e^{-\mu_2 x}) + U_{23}(C_5 e^{\mu_3 x} + C_6 e^{-\mu_3 x}) + A/B \cdot (C_7 x^3 + C_8 x^2 + C_9 x + C_{10}) \quad (43)$$

$$\bar{u}_1 = U_{51}(C_1 e^{\mu_1 x} - C_2 e^{-\mu_1 x})/\mu_1 + U_{52}(C_3 e^{\mu_2 x} - C_4 e^{-\mu_2 x})/\mu_2 + U_{53}(C_5 e^{\mu_3 x} - C_6 e^{-\mu_3 x})/\mu_3 - 3(T_1 + T_2 A/B)C_7 x^2/(F + G) + C_{11}x + C_{13} \quad (44)$$

$$\sigma_1 = \left[ U_{51}(C_1 e^{\mu_1 x} + C_2 e^{-\mu_1 x}) + U_{52}(C_3 e^{\mu_2 x} + C_4 e^{-\mu_2 x}) + U_{53}(C_5 e^{\mu_3 x} - C_6 e^{-\mu_3 x}) - 6(T_1 + T_2 A/B)C_7 x/(F + G) + C_{11} \right] / t_1 \quad (45)$$

$$\bar{u}_2 = - U_{51}(C_1 e^{\mu_1 x} - C_2 e^{-\mu_1 x})/\mu_1 - U_{52}(C_3 e^{\mu_2 x} - C_4 e^{-\mu_2 x})/\mu_2 - U_{53}(C_5 e^{\mu_3 x} - C_6 e^{-\mu_3 x})/\mu_3 + 3(T_1 + T_2 A/B)C_7 x^2/(F + G) + C_{12}x + C_{14} \quad (46)$$

$$\sigma_2 = \left[ - U_{51}(C_1 e^{\mu_1 x} + C_2 e^{-\mu_1 x}) - U_{52}(C_3 e^{\mu_2 x} + C_4 e^{-\mu_2 x}) - U_{53}(C_5 e^{\mu_3 x} - C_6 e^{-\mu_3 x}) + 6(T_1 + T_2 A/B)C_7 x/(F + G) + C_{12} \right] / t_1 \quad (47)$$

$$C_{12} = [2(T_1 + T_2 A/B)C_8 + FC_{11}]/G \quad (48)$$

$$C_{14} = [6(T_1 + T_2 A/B)C_7/\{E(F + G)\} + (T_1 + T_2 A/B)C_9 + FC_{13}]/G \quad (49)$$

For both cases:

$$U_{2i} = [A(C + D) - D\lambda_i F_1/D_1 + \lambda_i^2 D]/[B(C + D) - C\lambda_i F_2/D_2 + \lambda_i^2 C] \quad (50)$$

$$U_{5i} = -E\lambda_i(T_1 + T_2 U_{2i})/(E(F + G) - \lambda_i) \quad (51)$$

Using these expressions for  $\bar{w}_1$ ,  $\bar{w}_2$ ,  $\bar{u}_1$ , and  $\bar{u}_2$  and the boundary conditions resulting from integrating the expression for  $\delta\pi$  by parts, the coefficients can be evaluated. Axial stresses in the skin ( $\sigma_1$ ) and stringer ( $\sigma_2$ ) and the peel stress ( $\sigma_p$ ) are determined using Equations (37), (39), (45), (47), and (52).

$$\sigma_p = E_c(w_1 - w_2)/t_c \quad (52)$$

#### 4.3.2 Results

A FORTRAN computer program, PSTRESS, has been written to evaluate the coefficients described above for various loading conditions. The deflections calculated by this program are within 3 to 5 percent of those calculated using a NASTRAN finite-element analysis of an equivalent structure (Reference 7). The results were further corroborated by correlating the experimental results of an impact investigation with peel stresses calculated by PSTRESS (Reference 10). The PSTRESS results in this case agreed closely with NASTRAN finite-element analyses in predicting skin/stringer deflections due to impact over the stringer blade.

Figures 40 through 46 show plots of various stresses and displacements for a typical case with a composite skin and stringer. The skin lay-up is  $[0/45/0/-45/0/45/0-45/90]_{25}$  and the lay-up of the flange is  $[0/45/0/-45/0/45/0/-45/90]_8$ . The properties and loading used are as follows:

$E_1 = 4,713 \text{ ksi}$	$E_2 = 4,594 \text{ ksi}$
$D_1 = 3,685 \text{ lb-in.}$	$D_2 = 4,764 \text{ lb-in.}$
$t_1 = 0.224 \text{ in.}$	$t_2 = 0.224 \text{ in.}$
$E_c = 500 \text{ ksi}$	$G_c = 45 \text{ ksi}$
$t_c = 0.005 \text{ in.}$	$L = 1.2 \text{ in.}$

Load Case 1:  $P_1 = 100 \text{ lb/in.}$

Load Case 2:  $M_1 = 80 \text{ lb-in./in.}$

Load Case 3:  $F_1 = 1,600 \text{ lb/in.}$

Load Case 4:  $P_1 = 100 \text{ lb/in.}$ ,  $M_1 = 80 \text{ lb-in./in.}$ ,  $F_1 = 1,600 \text{ lb-in./in.}$   
 $P_2 = F_2 = M_2 = 0$

Parametric studies using PSTRESS (Reference 1) have demonstrated the relationships between the adhesive and adherend properties and the peel and shear stresses in the adhesive. The peel stress at the flange free edge ( $x = L$ ) is largely dependent on the applied moment and in-plane load, while the stress under the stringer blade ( $x = 0$ ) is primarily the result of the applied shear. Peak peel stress at the free edge is generally considered the critical cause of failure. Peel stress can be reduced in a number of ways. Decreasing rigidity, modulus, or thickness of the flange relative to the skin will decrease peak peel stress at the free edge, but will also increase the stress under the blade in cases with applied shear. Choosing an

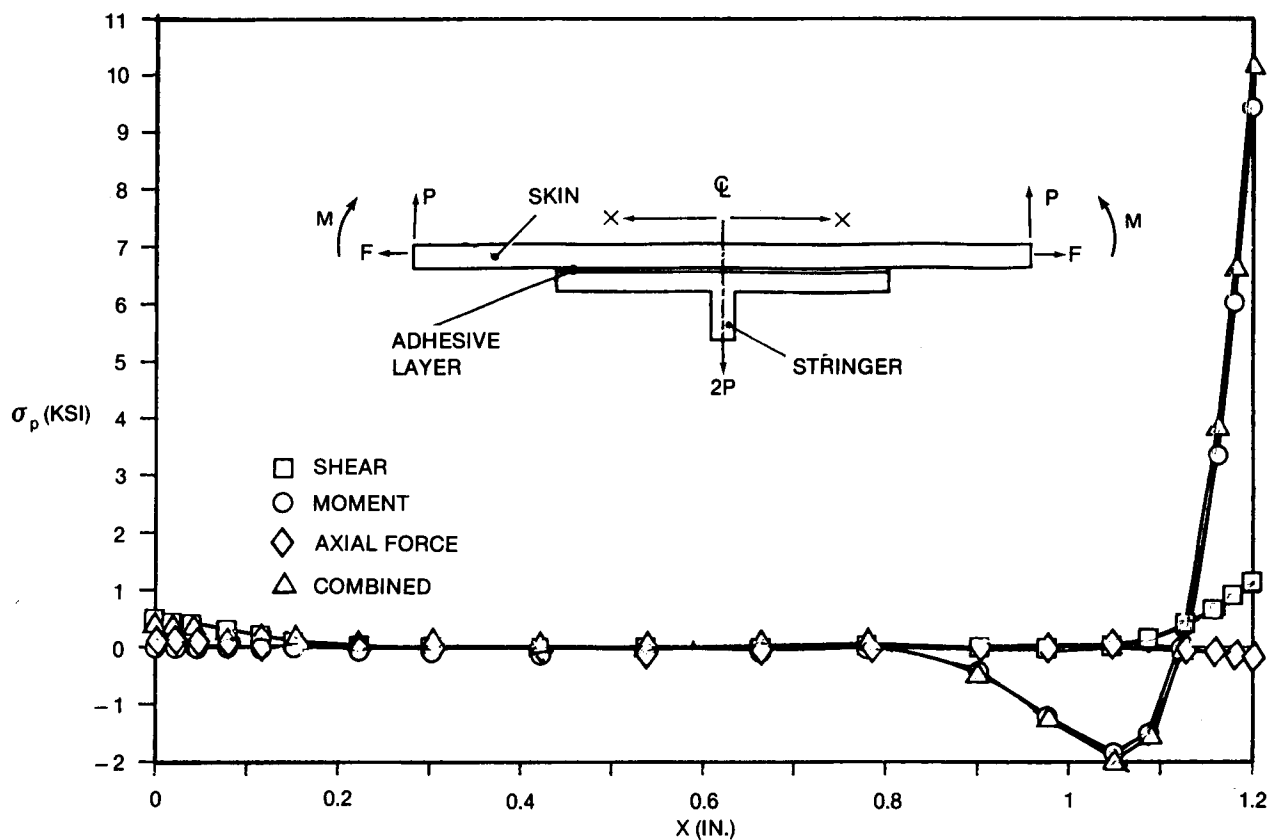


Figure 40. Peel Stress Distribution

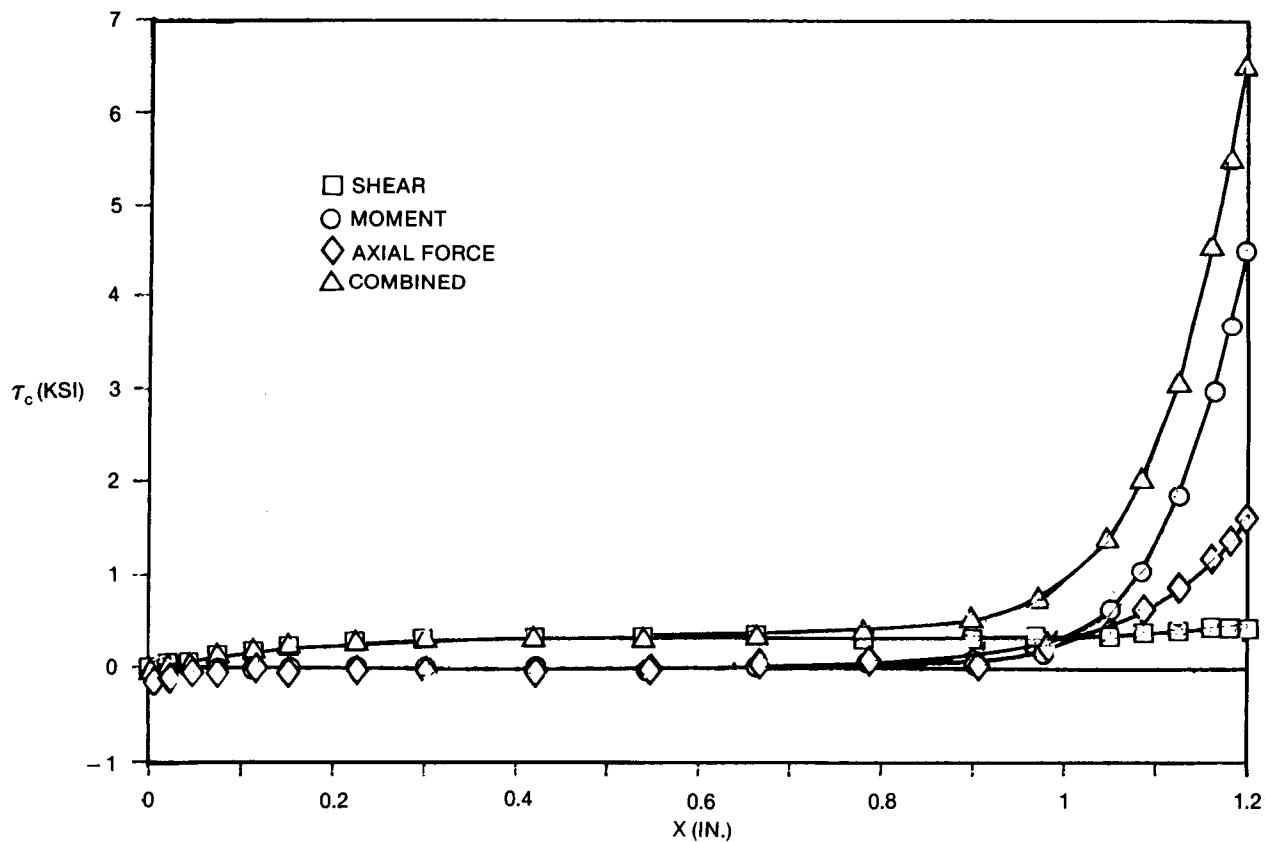


Figure 41. Shear Stress in Adhesive Layer

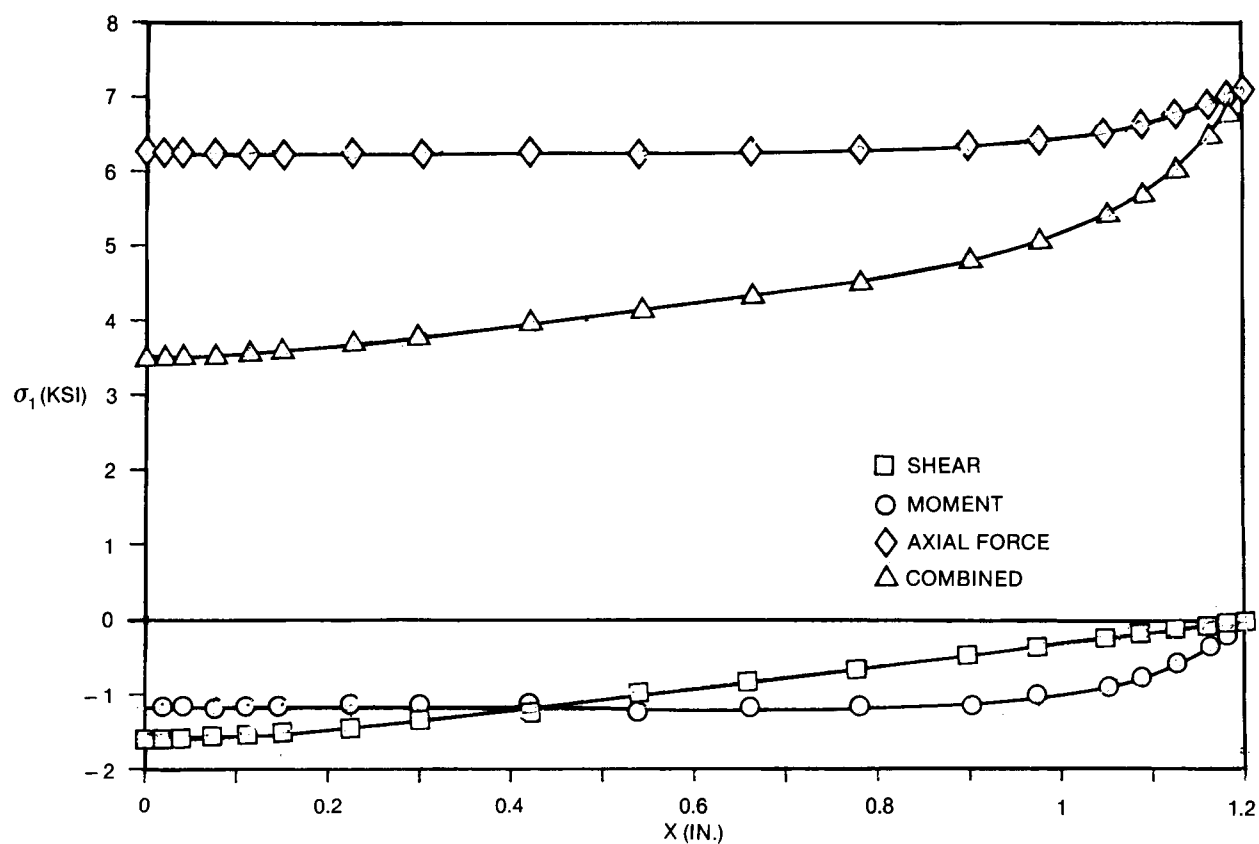


Figure 42. Axial Stress in Skin (Upper Plate)

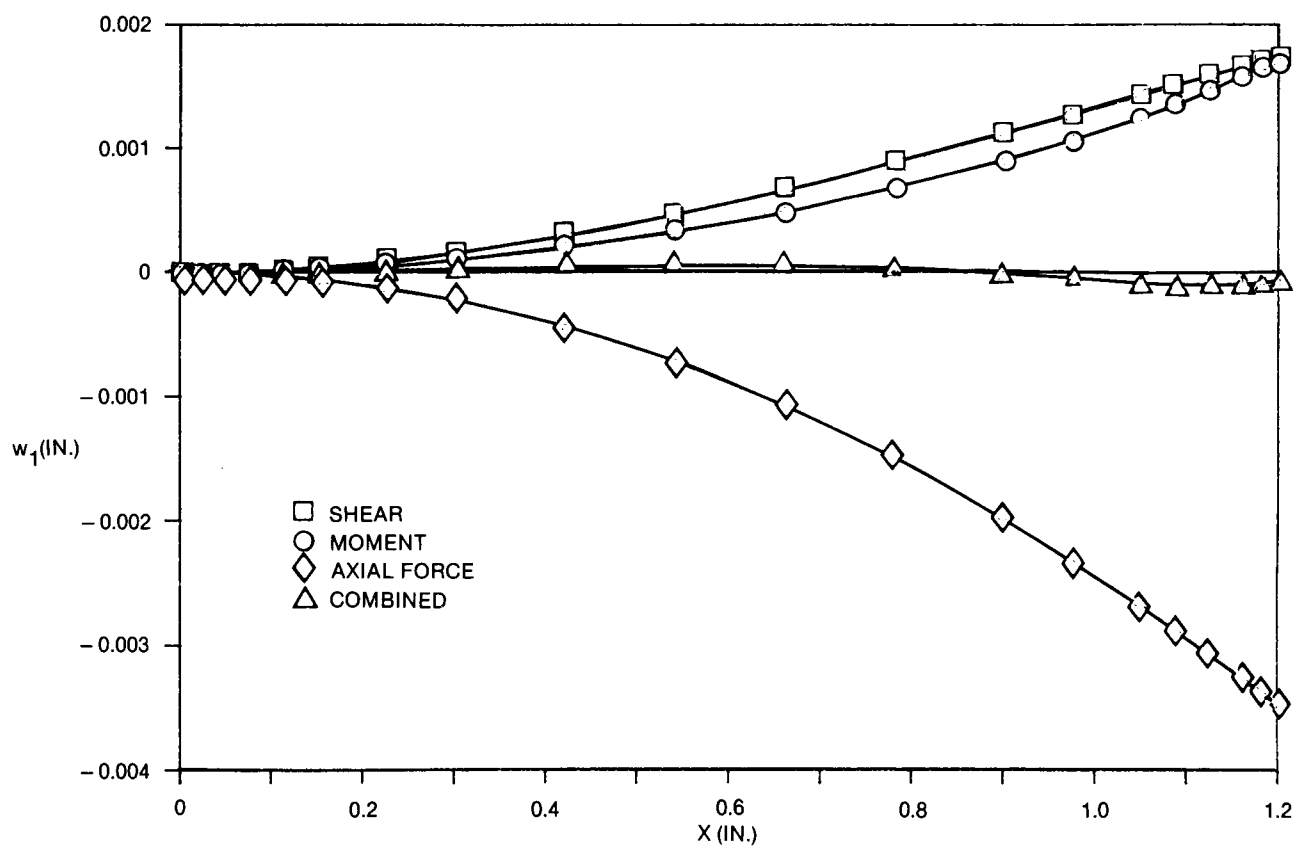


Figure 43. Out-of-Plane Deflection of Skin (Upper Plate)

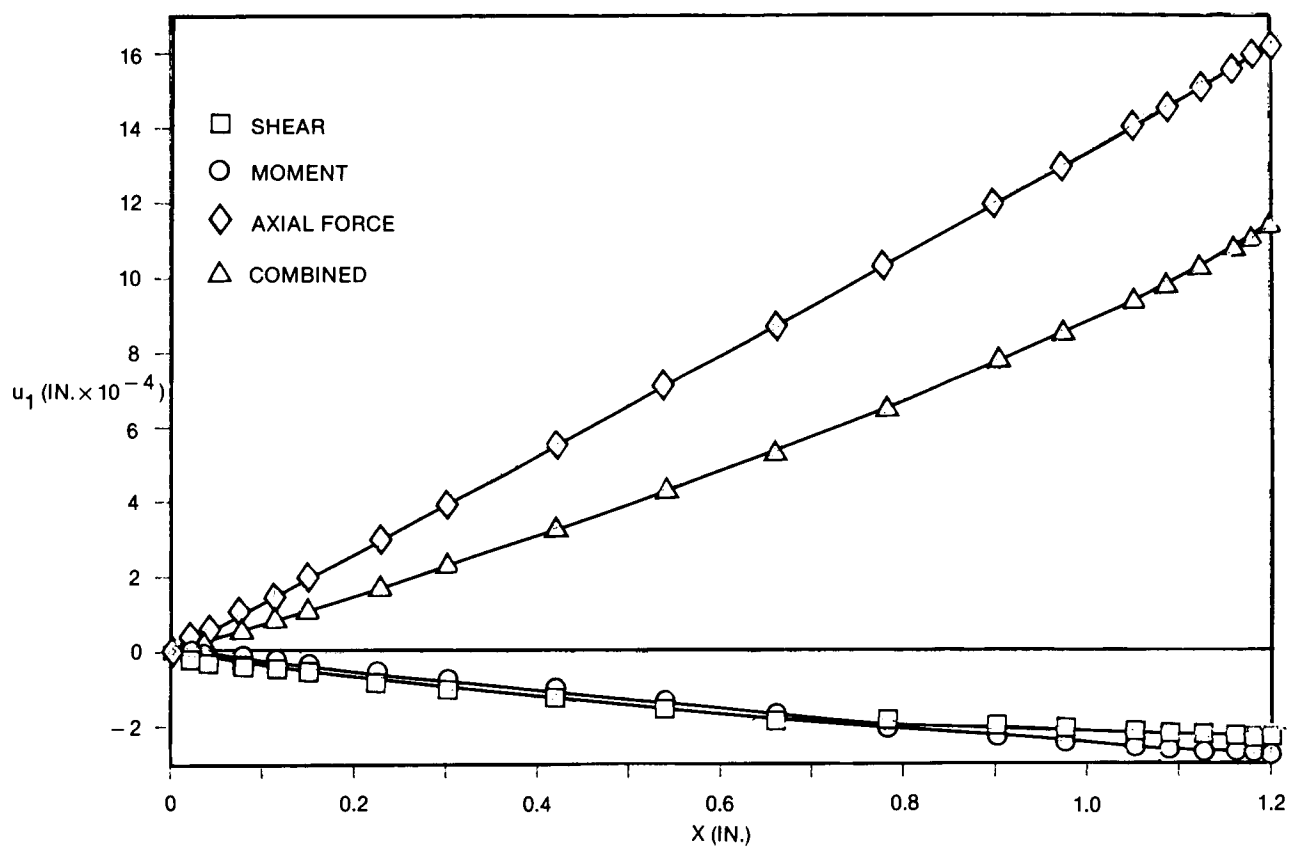


Figure 44. Axial Displacement of Skin (Upper Plate)

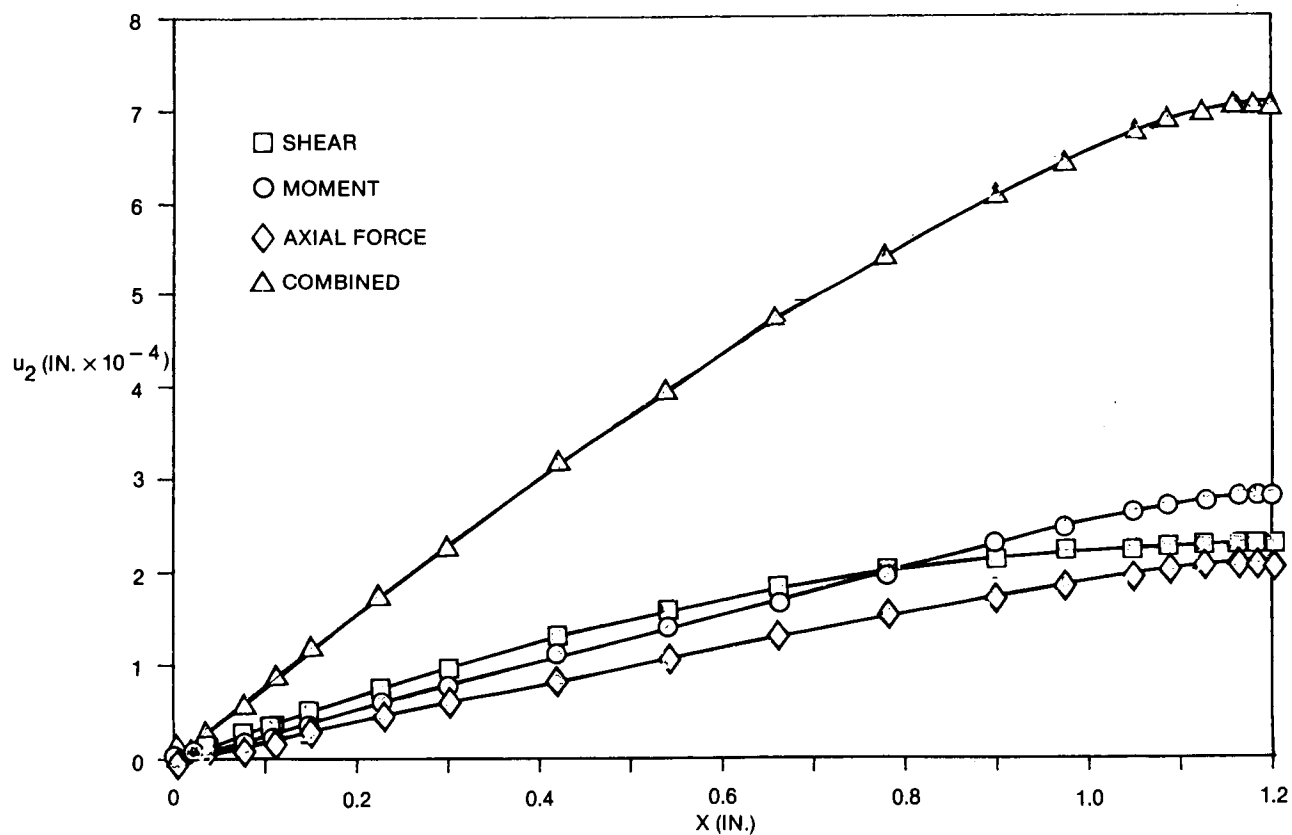


Figure 45. Axial Displacement of Flange (Lower Plate)



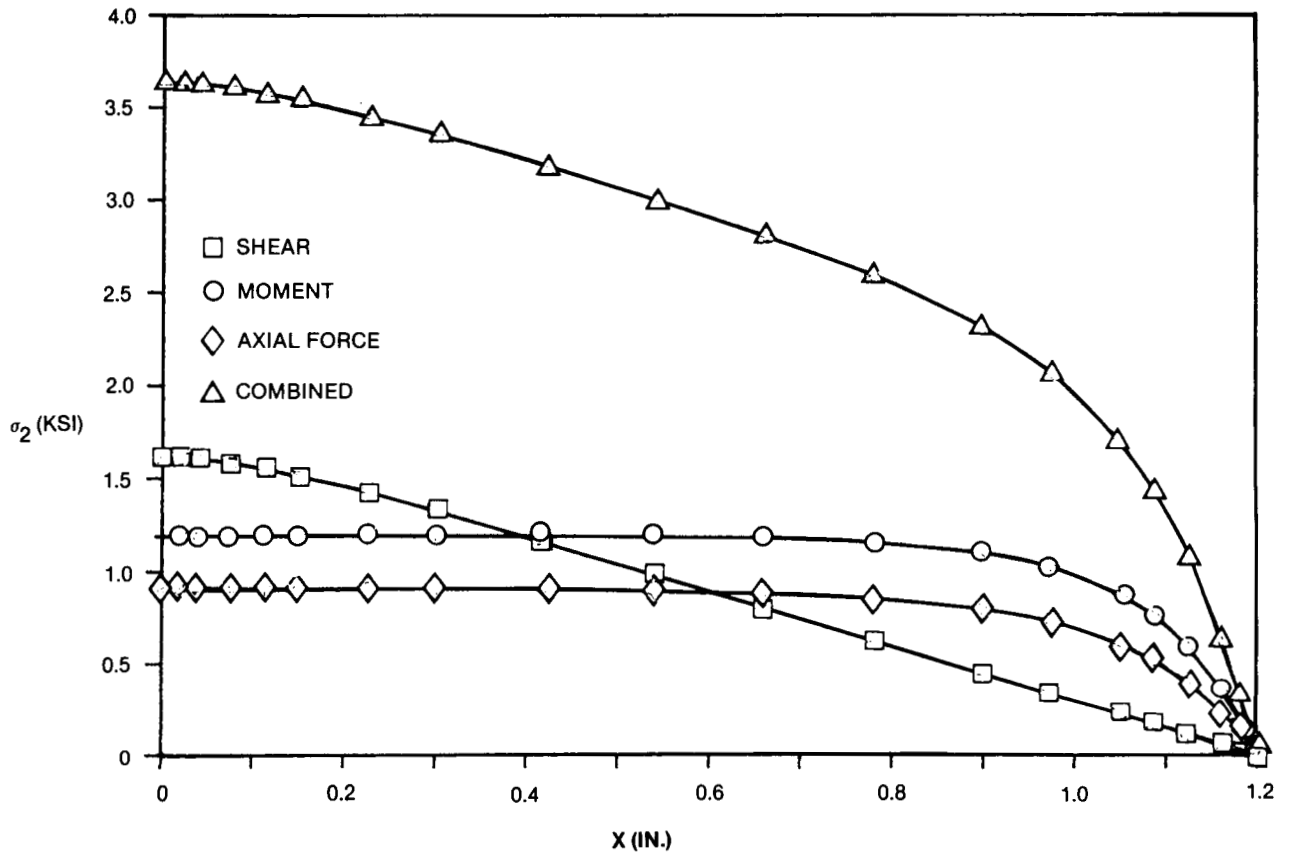


Figure 46. Axial Stress in Flange (Lower Plate)

adhesive with a lower Young's modulus ( $E_a$ ) will also decrease peak peel stress, but shear stress at the free edge will be increased. Adhesive shear modulus ( $G_a$ ), however, has relatively little impact on the peak peel stress. Increasing adhesive thickness ( $t_a$ ) is more effective than the above methods because it decreases peak peel stress at the free edge and at the blade and decreases shear stress.

#### 4.4 RESIDUAL STRENGTH ANALYSIS

The analysis method in this section predicts the initial static strength of panels containing single damage. The residual strength values obtained using this method may require adjustment to incorporate the effects of multiple-flaw interaction if dealing with very closely spaced damage and dynamic effects if the structure is loaded at the time of impact.

Many structural configurations provide multiple load paths and cannot be represented as monolithic sheets when assessing strength degradation from impact damage. Wing cover panels often consist of skin with mechanically fastened or integral stiffeners. The stiffeners can provide crack-arrestment capability because the stiffening member can accept load transferred from the skin and can resist crack opening displacement. In this way, it can significantly improve the residual strength of damaged structures.

Nuismer et al (References 11 and 12) suggested that the average stress criteria can be applied to both compression- and tension-loaded panels. The test results obtained by the authors showed that tension failure criteria can be replaced by substituting allowable compression stress for tensile stress. With the same reasoning, the point stress criteria are applied here for compression failure cases.

Point stress criterion (Reference 11) is applied to determine the failure mechanism of a damaged panel. The criterion can be expressed as:

$$\sigma_y(x,0)|_{x=c \pm d_o} = \sigma_o \quad (53)$$

where the characteristic distance ( $d_o$ ) is a material property, and the normal stress ( $\sigma_y$ ) at distance  $d_o$  from the edge of the hole equals the unnotched compressive strength of the material ( $\sigma_o$ ). Figure 47 shows the approximate distribution of  $\sigma_y$  in the region  $d_o$  for  $x > c$  (or  $R$ ), and Equation (54) is derived from Reference 13 by introducing the stress concentration factor ( $K_T$ ) of the laminate.

$$\sigma_y(x,0) = (2\sigma_o)[2 + p^2 + 3p^4 - (K_T - 3)(5p^6 - 7p^8)] - 1 \quad (54)$$

where  $p = c/x$  and  $c$  = half-length of a notch or radius of a hole. Substituting Equation (54) in Equation (50) gives

$$\sigma_o/\sigma_N = 0.5[2 + p^2 + 3p^4 - (K_T - 3)(5p^6 - 7p^8)] \quad (55)$$

where  $p = c/(c + d_o)$  and  $\sigma_N$  is the ultimate strength of the notched specimen.

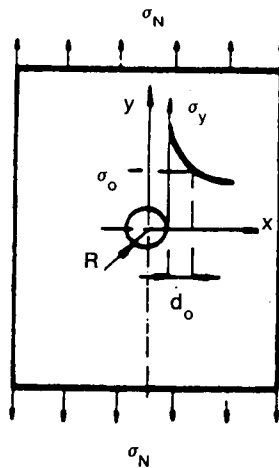
Reference 11 gives a relation between characteristic distances for point stress  $d_o$  and inherent flaw  $c_o$  criteria as

$$c_o = 2d_o \quad (56)$$

The characteristic distance  $c_o$  is constant (References 12, 14, and 15) for a given composite material system and is computed by the test results as follows:

$$c_o = c/((\sigma_o/\sigma_N)^2 - 1) \text{ and } K_Q = \sigma_N[\pi(c + c_o)]^{0.5} \quad (57)$$

Critical stress intensity factor,  $K_Q$ , and inherent flaw size,  $c_o$ , for different laminates for carbon-epoxy systems (Reference 15) are shown in Figure 48.



**Figure 47. Axial Stress Distribution for a Plate with a Hole and Characteristic Length,  $d_o$  (Point Stress Criterion)**

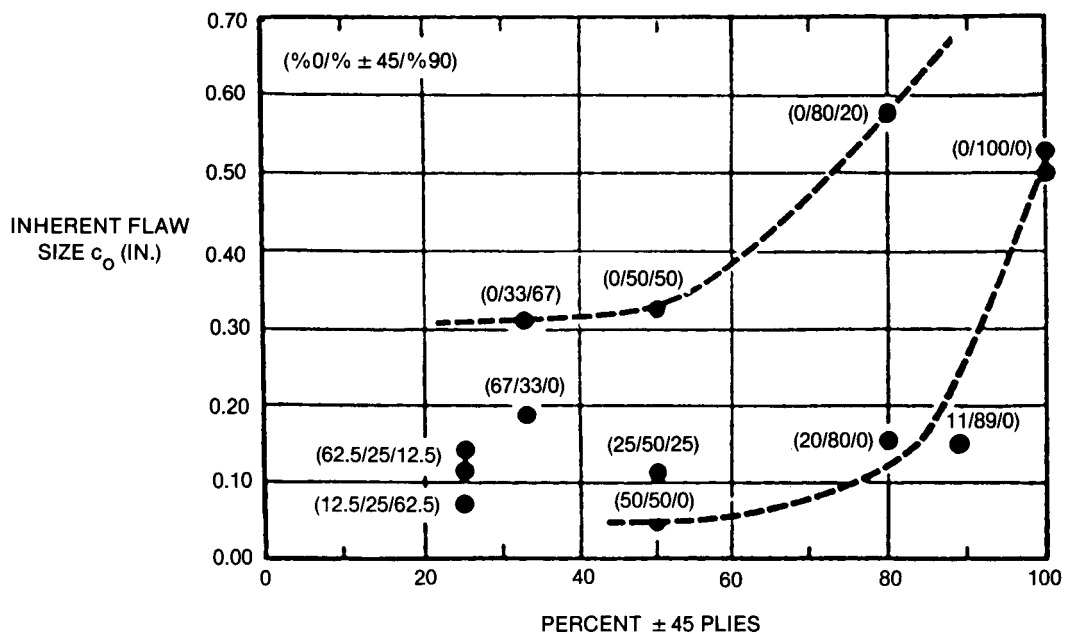
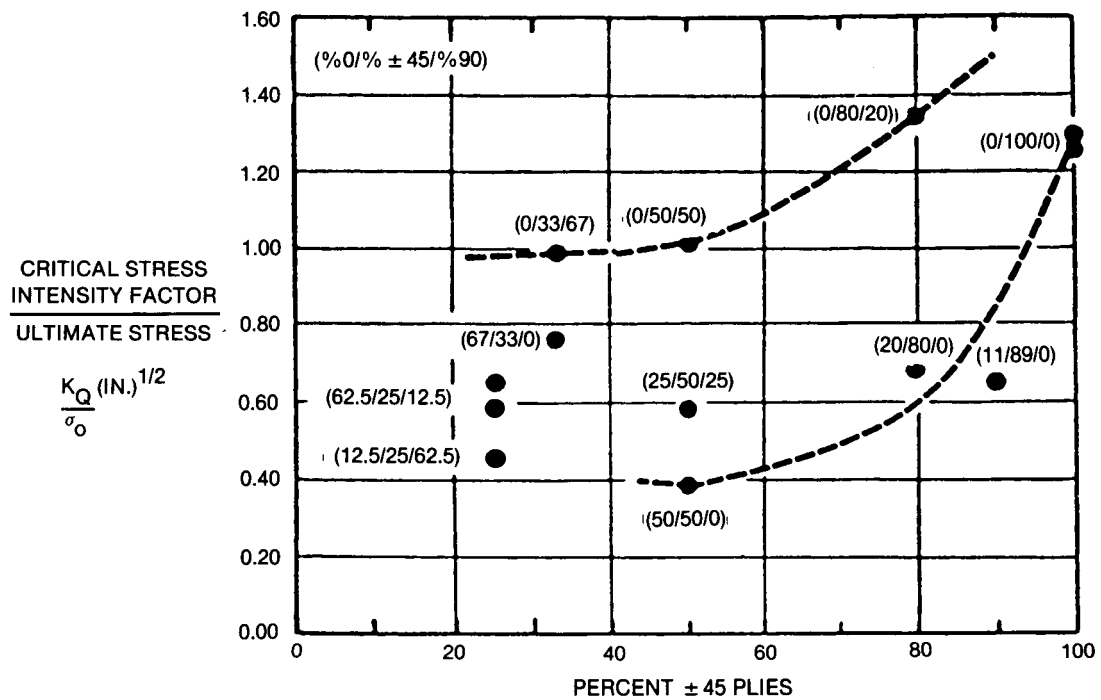


Figure 48. Critical Stress Intensity Factor and Inherent Flaw Size,  $c_o$ , for Different Laminates

#### 4.4.1 Effect of a Finite-Width Panel

##### Stress Concentration Factor

The effect of a finite-width panel on the stress concentration factor for hole damage is described in Reference 11.

For a hole, the finite-width factor  $Y$  is expressed as

$$Y = K_T/K_T^\infty = (2 + (1 - 2c/w)^3)/3(1 - 2c/w) \quad (58)$$

with radius  $c = 0.1875$  in. and  $w = 2$  in.,  $Y = 1.04$

For a notch, this factor is expressed as

$$Y = K_T/K_T^\infty = \sqrt{2/(\pi c) \tan(\pi c/w)} \quad (59)$$

with  $c = R = 0.1875$  in. and  $w = 2$  in.

$$Y = 1.02 \quad (60)$$

##### Stress Intensity Factor

The finite-width factor,  $Y$  for  $K_Q$  is given as

$$Y = \sec(\pi c/w) \quad (61)$$

with  $c = 0.1875$  in. and  $w = 2$  in.,  $Y = 1.022$

From Reference 14:

$$Y = (1 - 0.5p + 0.37p^2 - 0.044p^3)/(1 - p) \quad (62)$$

with  $p = c/w = 0.1875/2 = 0.09375$ ,  $Y = 1.005$

#### 4.4.2 Stress Concentration Factor

The  $K_T^\infty$  stress concentration factor (Reference 14) for an orthotropic infinite-width plate is given as

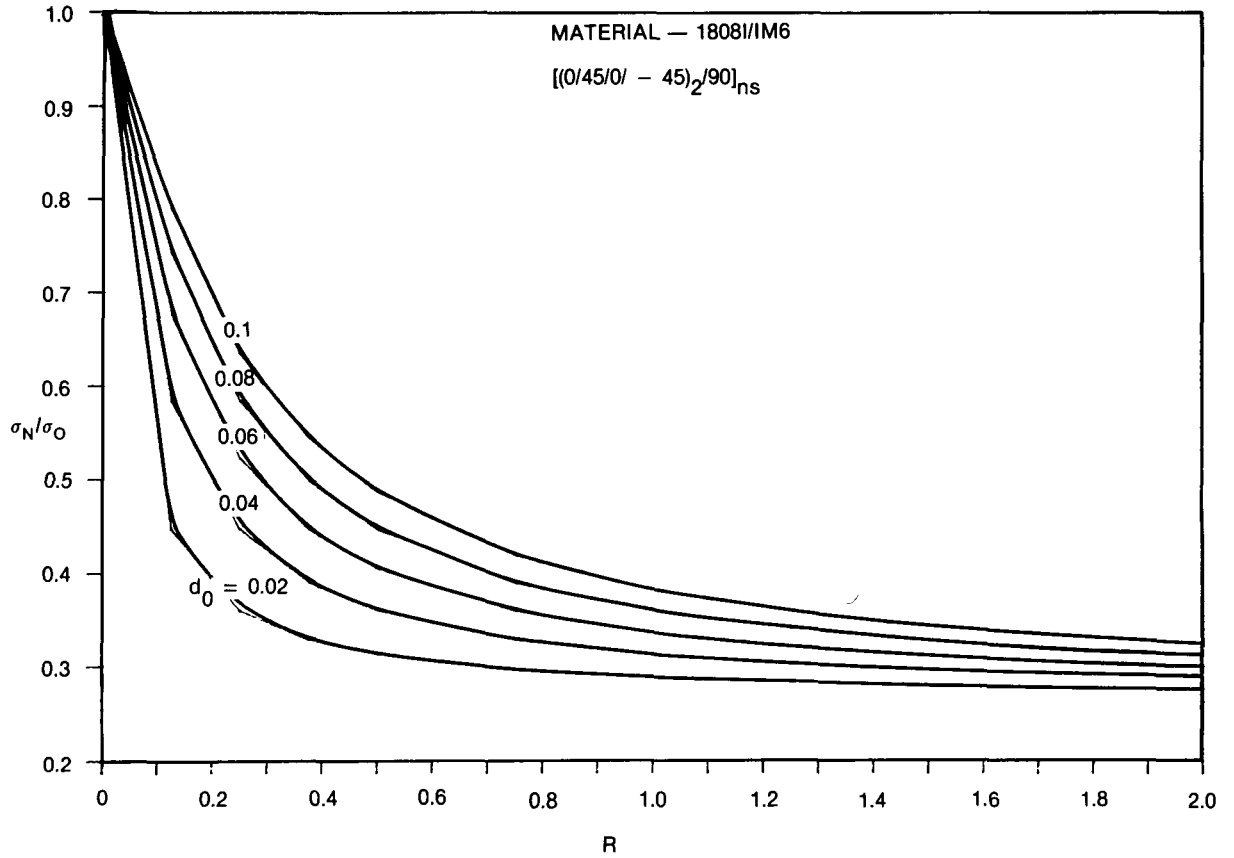
$$K_T^\infty = 1 + \sqrt{(2/A_{22}) [\sqrt{A_{11}A_{22} - A_{12}^2} + (A_{11}A_{22} - A_{12}^2)/2A_{66}]} \quad (63)$$

where the  $A_{ij}$  components are in-plane laminate stiffness determined from laminated plate theory. The subscript 1 denotes the direction parallel to the applied stress. The following values of  $A_{ij}$  are computed using an in-house program for 54-ply skin  $(0/45/0/-45/90/0/45/0/-45)_{3S}$  for the 1808I/IM6 material system.

$$\begin{aligned} A_{11} &= 3.397(10)^6 & A_{66} &= 0.7809(10)^6 \\ A_{12} &= 0.6678(10)^6 & E_L &= 10.07(10)^6 \\ A_{22} &= 1.609(10)^6 \end{aligned}$$

Using Equation (63),  $K_T^\infty = 3.464$  (64)

The residual strength of laminate  $(0/45/0/-45/90/0/45/0/-45)_{3S}$  is plotted in Figure 49 for material 1808I/IM6 with  $K_T$  equal to 3.5 for different  $d_o$  values.



**Figure 49. Residual Stress Distribution Versus Damage Size for Various Values of  $d_0$  (Point Stress Criteria) at  $K_T = 3.5$**

#### 4.4.3 Residual Strength

$\sigma_c$  = Residual strength of finite-width unstiffened panel in compression with damage

$\sigma_{cs} = \sigma_c$  for stiffened panel

$$C_{exp} = \sigma_c / \sigma_{cs} \quad (65)$$

$C_{exp}$  is determined by a method similar to that developed for metal structure by T.R. Porter (Reference 16).  $C_{exp}$  is related to stiffener area, skin gauge, stiffener spacing, and yield strengths of skin and stiffeners. The value of  $\sigma_c$  (unstiffened) is determined from fracture mechanics techniques for notched (damaged) panels by using the critical stress intensity factor in compression.

$$C_{exp} = \frac{\text{Failure Stress of Unstiffened Panel}}{\text{Failure Stress of Stiffened Panel}} \quad (66)$$

For metallic structures, an empirical relation has been plotted in Figure 50 for  $C_{exp}$  depending on  $R_{Fty}$  for riveted stiffened panels.

$$R_{Fty} = (EA_{Stif}/EA_{Skin})(F_{cystif}/F_{cyskin}) \quad (67)$$

where  $F_{cy}$  is yield strength of the material. It is assumed that bonded stiffened structure behaves similarly to riveted metallic structure in compression.

In the case of IM6/1808I material with (44/44/12) percentage of (0/45/90)-ply laminate used for stiffeners and skin structures,

$$F_{cyskin} = F_{cystif} \quad (68)$$

$$R_{Fty} = EA_{stif}/EA_{skin}$$

where  $EA_{stif}$  and  $EA_{skin}$  are the membrane stiffnesses of stiffener and skin.

#### 4.4.4 Analysis Method

The values of  $c_o$ ,  $\sigma_o$ , and  $K_Q$  for a given laminate are determined by conducting unnotched and open-hole compression tests using Equation (57).  $K_{\varphi}$  is determined using Equation (63), and Equation (56) is applied to determine  $d_o$ .  $K_T$  is found using Equation (58) or (59), depending on the type of damage, and Equation (67) is used to determine  $R_{Fty}$ .  $C_{exp}$  is determined from Figure 50, and, finally,  $\sigma_{cs}$  is determined from Equation (65). The application of this method is illustrated with actual cases in Section 5.

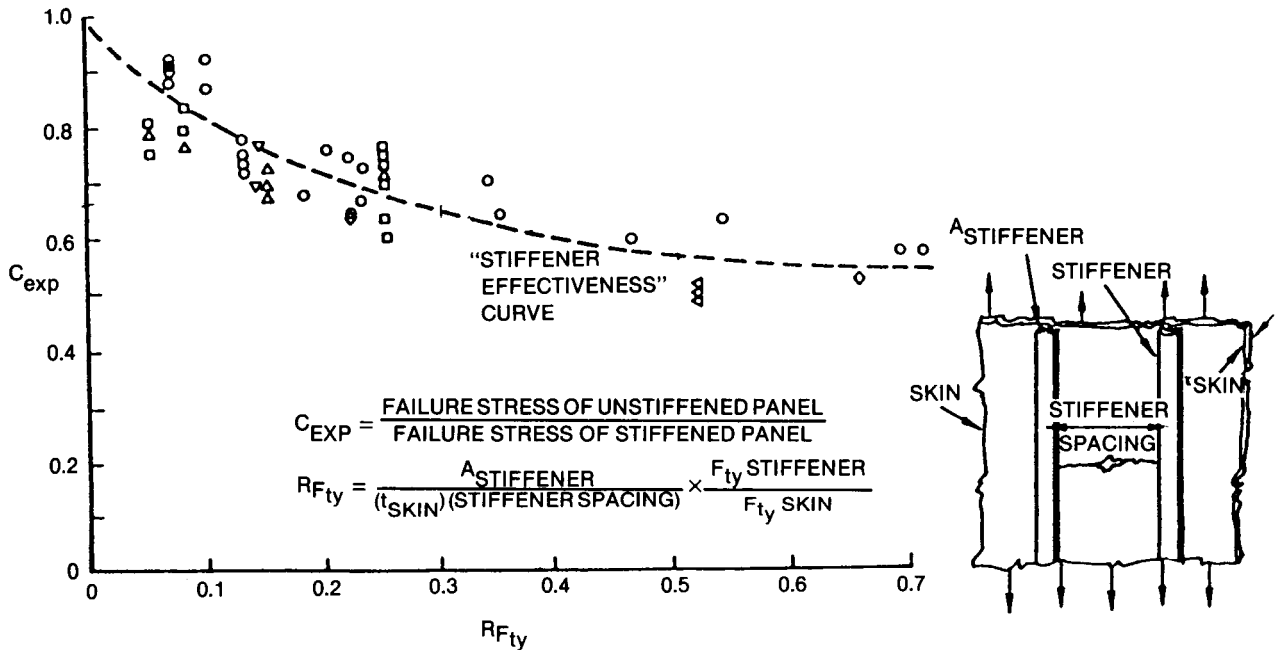


Figure 50. Stress Distribution for Stiffened Panel

## SECTION 5

### TEST RESULTS AND DISCUSSION

A summary of the tests for this program is presented in Tables 5 through 7. A series of ancillary tests (Table 5) to generate basic data required for the residual strength analysis of stiffened panel test specimens were conducted. Table 6 describes the development test program, also conducted at Douglas. These tests were included to assess the selected cover panel design concepts. Table 7 contains the large demonstration panel specimens to be tested at NASA Langley Research Center.

The trial impact specimen (Table 6) was used to determine the extent and visibility of damage at various locations on the cover panel structure for specific impact energy levels. Single-stringer specimens were tested to evaluate stringer pull-off strengths and static crushing/crippling strengths. Screening tests determined the residual strength of the selected cover panels after they sustained impact damage at critical locations. These tests also determined the most critical impact location for the Douglas cover panel concepts. These tests were essential to the concept evaluation process.

The large five-stringer panels shipped to the NASA facility for tests will demonstrate the damage tolerance capabilities of the selected concept for the most critical impact damage under compression loads. With five stringers and representative rib attach points, these tests will provide a realistic assessment of the final design.

#### 5.1 ANCILLARY TESTS

##### 5.1.1 Tension and Compression Tests

Test results for the unnotched tension and compression tests are shown in Table 12. The tension test results were reasonably consistent for both strength and stiffness. The average ultimate tensile stress for the  $[(0/45/0/-45)_2/90]_{ns}$  laminate was roughly 133,000 psi, with a modulus value of approximately 10,100,000 psi. Unfortunately, four of the five unnotched compression test specimens suffered premature failures at the ends. The only specimen that appeared to exhibit a true compression failure, with a failure stress of 107,030 psi, is listed in Table 12. The test setup used is shown in Figure 23. The premature failures were characterized by a brooming or crushing of the specimens at the load introduction end. It is suspected that these failures resulted from insufficient quality in the surface grinding of the specimen ends.

**Table 12**  
**Tension and Compression Test Results**

SPECIMEN	AREA (IN. <sup>2</sup> )	ULT LOAD (LB)	FAILURE STRAIN (IN.)	FAILURE STRESS (PSI)
UTB1	0.1150	15,020	0.0013	130,608
UTB2	0.1151	15,340	0.00133	133,275
UTB3	0.1145	15,460	0.00131	135,021
AVG		15,273	0.00133	132,968
UCB1		- 8,830		- 107,030

##### 5.1.2 Open-Hole Compression Tests

Tests of open-hole compression specimens were conducted in accordance with NASA standards (Reference 1). The results of the tests are presented in Table 13. The results were generally as expected. In

**Table 13**  
**Open-Hole Compression Test Results**

SPECIMEN NUMBER	WIDTH w (IN.)	DIAMETER d (IN.)	THICKNESS t (IN.)	w/d	FAILURE LOAD (LB)	GROSS STRESS (PSI)	FAILURE STRAIN μIN./IN.	K <sub>tc</sub> *
1	2.0	0.375	0.33	5.33	32,600	49,390	4,615	1.64
2	2.0	0.375	0.33	5.33	32,150	48,710	4,552	1.67
3	2.0	0.375	0.33	5.33	33,300	50,450	4,715	1.61

MATERIAL: 1808I/IM6  
LAMINATE PATTERN: (0/45/0/- 45/0/45/0/- 45/90)<sub>3S</sub>  
PLY THICKNESS: APPROXIMATELY 0.0062 IN./PLY

\*K<sub>tc</sub> VALUES BASED ON F<sub>cu</sub> = 100 KSI

Table 13, the stress concentration factors for the open-hole tests (based on an unnotched compression allowable of 100 ksi) are compared to the computed elastic-isotropic stress concentration factors. A comparison of these values shows that the results are similar to previous test programs, and the test results indicate that the notch sensitivity exhibited by these specimens is typical of most carbon-epoxy material systems. The material was found to be resistant to impact damage because of the presence of the interleaf adhesive layer.

#### 5.1.3 Compression-Bearing Tests

The compression-bearing tests were designed to provide bearing stress allowables for the design and analysis of the bolted repair panel. The results shown in Table 14 were fairly consistent with an average ultimate bearing stress of roughly 140 ksi and an average "yield" stress of about 118 ksi.

**Table 14**  
**Compression Bearing Test Results**

SPECIMEN NUMBER	WIDTH w (IN.)	DIAMETER d (IN.)	SPLICE THICKNESS (IN.)	ULTIMATE LOAD (LB)	YIELD* LOAD (LB)	ULTIMATE BEARING STRESS (PSI)	BEARING YIELD STRESS (PSI)	FAILURE STRAIN (PERCENT)
1	2.0	0.375	0.28	17,100	14,100	138,180	113,940	0.6135
2	2.0	0.375	0.28	17,400	14,400	140,610	116,360	0.6086
3	2.0	0.375	0.28	18,000	15,300	145,450	123,640	0.6239

MATERIAL: 1808I/IM6  
LAMINATE PATTERN: (0/45/0/- 45/0/45/0/- 45/90)<sub>3S</sub>, SKIN THICKNESS = 0.33 IN.  
PLY THICKNESS: APPROXIMATELY 0.0061 IN./PLY  
FAILURE MODE: BEARING FAILURE IN CENTRAL MEMBER

\*YIELD POINT DEFINED AS INITIAL POINT OF NONLINEARITY

#### 5.1.4 One-Dimensional Delamination Tests

Eighteen one-dimensional delamination compression specimens were tested. The load was supplied by two specially prepared ± 0.0005-inch oil-hardened stainless steel loading blocks approximately 0.380 inch thick. Each was fastened to 0.1- by 2- by 5.2-inch aluminum sheet stock with 0.005-inch double-backed tape. Finally, 0.020- by 2- by 3-inch aluminum shim stock was butted up to the loading blocks to provide a glide path for the specimen. This entire assembly was placed inside 0.85-inch-thick steel angle plates and bolted down (see Figure 22).



In each case, a strain gage was mounted on the laminate surface directly over the insert. It was assumed that, when the inserted delamination fractured, the outer plies at the delamination site would no longer carry load and the gage would indicate a sudden drop in strain level. This was the case in each test. It should be noted that these test results, shown in Table 15, were surprisingly consistent (free of scatter) compared to the results obtained by other researchers.

In each case, initial growth of the inserted delamination was observed and noted. It was not clearly evident at what load level so-called "fast fracture" occurred, since the delamination growth to the specimen ends was somewhat sporadic.

**Table 15**  
**One-Dimensional Compression Delamination Test Results**

ID NO.	SPECIMEN			DELAMINATION ONSET				ULTIMATE FAILURE		
	WIDTH (IN.)	THICK (IN.)	DEFECT DEPTH, SIZE	LOAD (LB)	STRAIN ( $\mu$ IN./IN.)	STRESS (PSI)	GAGE LENGTH (IN.)	LOAD (LB)	STRAIN ( $\mu$ IN./IN.)	STRESS (PSI)
507-1	1.00	0.34	PLIES 5,6	21,550	6,350	63,382	3.00	27,050	6,868	79,559
507-2			SIZE =	21,400	5,810	62,941		26,300	6,887	77,353
507-3			0.5 IN.	22,150	7,400	65,147	↓	27,300	8,868	80,294
509-1			PLIES 5,6	10,000	2,931	29,411	3.00	25,850	6,941	76,026
509-2			SIZE =	9,000	2,750	26,471	↓	26,150	7,007	76,912
509-3			1.0 IN.	9,000	2,701	26,471	↓	25,900	7,205	76,176
511-1*			PLIES 5,6	4,000	1,018	11,765	2.50	27,500	7,735	80,882
511-2			SIZE =	5,000	1,462	14,706	↓	28,650	9,179	84,265
511-3			1.5 IN.	4,000	1,053	11,765	↓	29,200	8,950	85,882
513-1			PLIES 3,4	12,000	3,662	35,294	3.00	29,350	8,358	86,324
513-2			SIZE =	11,000	3,443	32,353	↓	28,850	8,521	84,853
513-3			0.5 IN.	12,500	3,841	36,765	↓	28,450	8,683	83,676
515-1			PLIES 3,4	4,000	1,135	11,765	3.00	28,800	6,979	84,706
515-2			SIZE =	4,000	1,089	11,765	↓	26,150	7,602	76,912
515-3			1.0 IN.	4,000	1,234	11,765	↓	27,400	7,244	80,588
517-1*	↓	↓	PLIES 3,4	2,100	667	6,176	2.50	31,100	8,717	91,471
517-2			SIZE =	1,500	604	4,412	↓	26,650	8,207	78,382
517-3			1.5 IN.	2,000	552	5,882	↓	24,950	5,519	73,382

MATERIAL: 1808I/IM6 LAMINATE:  $[(0/+45/0/-45)_2/90]_{3S}$  LENGTH: 9 IN.  
ROOM TEMPERATURE, DRY

\*LENGTH OF SPECIMEN IS 8.5 IN.

### 5.1.5 Two-Dimensional Delamination Tests

Two-dimensional delamination tests were conducted on three specimens with circular inserts between plies 3 and 4. The panels failed in compression across the free section (approximately 0.25-inch gap) above the antibuckling plates. Some damage propagated around the insert to the ninth ply just prior to total compressive failure. The opposite surface also buckled along the ninth ply, and this delamination also propagated into the compression failure area. Fracture along the central plies was also evident.

The specimens were tested in the ST-1 (Reference 1) fixture with antibuckling plates. The insert buckled on the specimen surface at an average of about 40,000 pounds. The buckle was initially the same shape as the insert. As the load increased, the delamination grew laterally toward the antibuckling plates.

**Table 16**  
**Two-Dimensional Compression Delamination Test Results**

ID NO.	SPECIMEN DIMENSIONS			INITIAL DELAMINATION			ULTIMATE FAILURE			
	WIDTH (IN.)	THICK (IN.)	DEFECT SIZE, (IN.) LOCATION	LOAD (LB)	STRAIN ( $\mu$ IN./IN.)	STRESS (PSI)	GAGE LENGTH (IN.)	LOAD (LB)	STRAIN ( $\mu$ IN./IN.)	STRESS (PSI)
501-1	5.00	0.333	1-IN. DIA PLIES 3,4	45,000	2,850	24,024	9.00	125,840	8,431	75,504
501-2	5.00	0.333	1-IN. DIA PLIES 3,4	40,000	2,375	24,024	9.00	120,120	7,890	72,072
501-3	5.00	0.333	1-IN. DIA PLIES 3,4	40,000	2,198	24,024	9.00	124,300	7,650	74,580

MATERIAL: 1808I/IM6 LAMINATE:  $[(0/\pm 45/0/-45)_2/90]_{3S}$   
ROOM TEMPERATURE, DRY

Seconds before the ultimate compression failure occurred in the free section, the delamination grew under the antibuckling plates. Test results for the three successful two-dimensional delamination tests are shown in Table 15. Three tested coupons of two-dimensional delamination tests (see Table 16) showed consistent results, which were considered very good for 1-inch-diameter inserts between plies 3 and 4.

### 5.1.6 Edge Delamination Test

The results of the edge delamination tension tests (Reference 1) for the 1808I/IM6 material are shown in Table 17. The values for fracture toughness,  $G_c$ , are typical of most high-toughness material systems. The results, shown in Figure 51, were also consistent between the 8-ply and 11-ply tests.

### 5.1.7 Hinged Double Cantilever Beam Test

The hinged double cantilever beam test (Reference 1) results are presented in Table 18 and Figure 51. The average value for  $G_{IC}$  of 1.71 in.-lb./in.<sup>2</sup> is consistent with the results of the in-house material evaluation tests. The  $G_{IC}$  values were calculated using the energy-area integration method. Calculations using the modified direct beam equation method would give slightly higher  $G_{IC}$  values.

### 5.1.8 Compression-After-Impact Test

Compression-after-impact tests (Reference 1) were run on five panels. The results of these tests are shown in Table 19. One panel was impacted at 20 ft-lb and two panels were impacted at 50 ft-lb with a 1-inch hemispherical impactor.

Two remaining panels were impacted at an energy level of 26.4 ft-lb using a 10-pound weight with a 1/2-inch hemispherical impactor. The 26.4 ft-lb impacts left barely visible damage on the surface of the laminate, with no visible damage on the back surface. The 50 ft-lb impacts were slightly more visible on the impact surface, and a slight split in the 0-degree ply on the laminate back surface was visible. X-rays taken of each panel revealed minimal internal damage for the 26.4 ft-lb impacts, with a slight increase in damage area for the 50-ft-lb impacts.

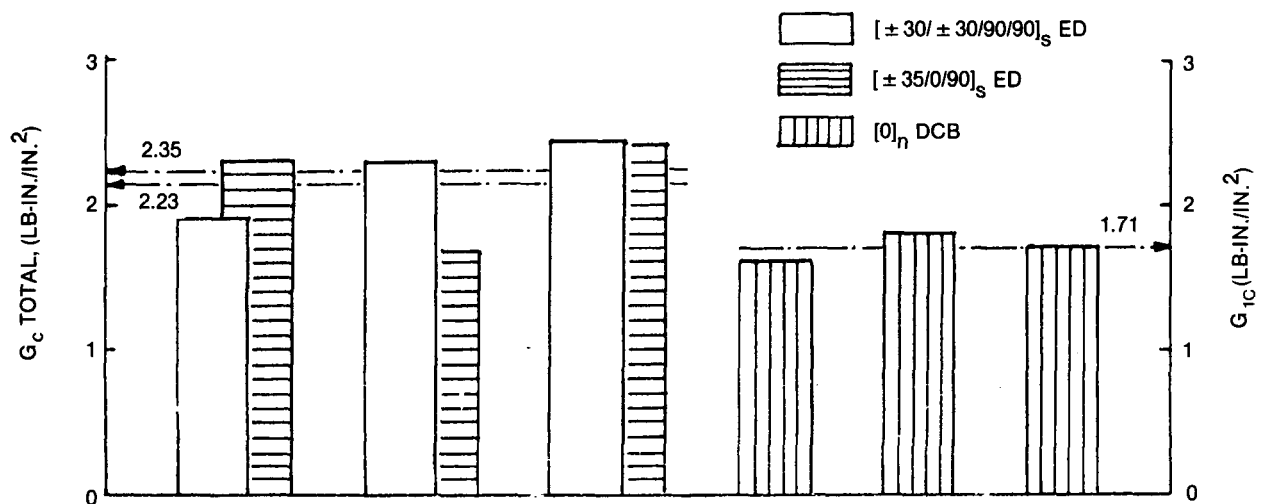
**Table 17**  
**ST-2 Edge Delamination Tension Test Data**

LAMINATE ORIENTATION: $(\pm 35/0/90)_S$			$E_{lam} = 9.97 \times 10^6 \text{ PSI}$			$E^* = 8.13 \times 10^6 \text{ PSI}$
TEST CONDITION: 75°F DRY						$E_{(\pm 35/0)_S} = 10.45 \times 10^6 \text{ PSI}$
SPECIMEN ID	THICKNESS (IN.)	WIDTH (IN.)	DELAMINATION ONSET STRAIN* (IN./IN.)	FAILURE STRAIN (IN./IN.)	TENSILE MODULUS (PSI)	INTERLAMINAR FRACTURE TOUGHNESS $G_c \left( \frac{\text{IN.-LB.}}{\text{IN.}^2} \right)$
ST-211	0.0509	1.495	0.0064	0.0077	$9.03 \times 10^6$	1.92
ST-212	0.0510	1.495	0.0070	0.0089	$9.06 \times 10^6$	2.30
ST-213	0.0515	1.497	0.0072	0.0074	$9.01 \times 10^6$	2.46
AVERAGE:	0.0511	1.496	0.0069	0.0080	$9.03 \times 10^6$	2.23

LAMINATE ORIENTATION: $(\pm 30/\pm 30/90/90)_S$			$E_{lam} = 8.38 \times 10^6 \text{ PSI}$			$E^* = 5.32 \times 10^6 \text{ PSI}$
TEST CONDITION: 75°F DRY						$E_{(\pm 30)_S} = 6.89 \times 10^6 \text{ PSI}$
SPECIMEN ID	THICKNESS (IN.)	WIDTH (IN.)	DELAMINATION ONSET STRAIN* (IN./IN.)	FAILURE STRAIN (IN./IN.)	TENSILE MODULUS (PSI)	INTERLAMINAR FRACTURE TOUGHNESS $G_c \left( \frac{\text{IN.-LB.}}{\text{IN.}^2} \right)$
ST-221	0.0689	1.500	0.0047	0.0057	$7.60 \times 10^6$	2.32
ST-222	0.0690	1.499	0.0040	0.0058	$7.59 \times 10^6$	1.69
ST-223	0.0690	1.498	0.0048	0.0056	$7.62 \times 10^6$	2.43
AVERAGE:	0.0690	1.499	0.0045	0.0057	$7.60 \times 10^6$	2.15

\*STRAIN AT FIRST DEVIATION FROM LINEAR STRESS-STRAIN CURVE  
MATERIAL: 1808I/IM6



**Figure 51. 1808I/IM6 Fracture Toughness**

**Table 18**  
**ST-5 Hinged Double Cantilever Beam Test Data**

LAMINATE ORIENTATION: (0) <sub>n</sub> TEST CONDITION: 75°F DRY MATERIAL: 1808I/IM6 h = 0.00625 IN./PLY										
COUPON ID	a <sub>1</sub> (IN.)	δ <sub>1</sub> (IN.)	P <sub>1</sub> (IN.)	a <sub>2</sub> (IN.)	δ <sub>2</sub> (IN.)	P <sub>2</sub> (IN.)	a <sub>3</sub> (IN.)	δ <sub>3</sub> (IN.)	P <sub>3</sub> (IN.)	G <sub>IC</sub> * ( $\frac{\text{IN.-LB}}{\text{IN.}^2}$ )
ST5-1	1.00	0.14	21	2.03	0.19	14	3.05	0.32	7	1.62
ST5-2	0.98	0.13	22	2.00	0.20	14	2.97	0.33	6	1.91
ST5-3	0.98	0.12	21	2.09	0.22	14	3.00	0.34	5	1.73
										1.71 AVG

\*G<sub>IC</sub> VALUES CALCULATED BY ENERGY-AREA INTEGRATION METHOD

**Table 19**  
**Compression After Impact Test Data**

LAMINATE ORIENTATION: (+45/0/-45/90) <sub>NS</sub> TEST CONDITION: 75°F DRY MATERIAL: 1808I/IM6 h = 0.00625 IN./PLY											
SPECIMEN ID	THICKNESS (IN.)	WIDTH (IN.)	IMPACT ENERGY (FT-LB)	MAXIMUM WIDTH OF IMPACT DAMAGE (IN.)	VISUAL IMPACT DAMAGE		IMPACT AREA (IN. <sup>2</sup> )	FAILURE LOAD (KIPS)	FAILURE STRESS (KSI)	FAILURE STRAIN (μIN./IN.)	COMPRESSION MODULUS (PSI)
					FRONT SURFACE	BACK SURFACE					
CAI-1	0.3297	5.002	26.4	1.5	YES	NO	2.84	80.41	48.76	4,920	9.91 × 10 <sup>6</sup>
CAI-2	0.3309	4.962	20.0	0.5	YES	NO	0.196	105.16	64.05	6,731	9.52 × 10 <sup>6</sup>
CAI-3	0.3312	5.095	26.4	1.48	YES	NO	2.47	90.42	53.58	5,522	9.70 × 10 <sup>6</sup>
CAI-4	0.3303	5.096	50.0	2.25	YES	YES*	5.13	76.89	45.68	4,625	9.88 × 10 <sup>6</sup>
CAI-5	0.3310	5.93	50.0	2.28	YES	YES*	7.7	79.97	47.44	4,843	9.80 × 10 <sup>6</sup>

\*SLIGHT SPLIT IN 0-DEGREE PLY ON BACK SURFACE

## 5.2 DEVELOPMENT TEST SPECIMENS

There were two groups of panels — B-group and C-group. The panels were designated as B1 and B2, and as C1, C2, C3, and C4. The B-group stiffeners had 36-ply flanges, while the C-group stiffeners had 18-ply flanges. During test, both groups of panels behaved quite differently. Panels B1 and B2 separated at the skin/stringer bond line before reaching failure load. The skin panel alone reached the buckling stage and finally fractured in bending, leaving the stringer undamaged. This type of behavior was expected as the impact test on the B1 panel had caused the skin to separate extensively from the stringers. Panels C1, C2, and C3 were fractured along the centerline of the panels, without any sign of separation of skin from stringers. It appears that the crack started from the impact damage area and propagated across the width of the panel, simultaneously fracturing both skin and stringer. Complete details of the test, results, and the analysis are presented below.

### 5.2.1 Experimental Results

The strain gage readings for all locations of the six panels for compression tests at various load levels are summarized in Tables 20 through 25. Photographs of two panels following the compression tests are shown in Figures 52 and 53. Table 26 summarizes the results of the compression tests in terms of failure stress and strain. The average strain is computed by dividing the crosshead displacement ( $\Delta$ ) by the length of the panel ( $\ell$ ). The stresses are computed on the basis of the gross cross-sectional area of the panel with nominal dimensions. In the test column of the above table,  $\Delta i-j$  defines the difference in failure strains at locations i and j in  $\mu\text{in.}/\text{in.}$

**Table 20**  
**Strain Gage Readings for Panel B1**

LOAD (KIPS)	STRAIN GAGE READING ( $-\mu\text{IN.}/\text{IN.}$ )										
	1	2	3	4	5	6	7	8	9	10	11
0	-2	3	1	0	-2	-1	-3	1	-1	2	1
50	419	465	421	442	445	550	416	475	521	536	462
100	873	911	861	884	871	985	812	905	927	945	898
150	1,347	1,381	1,334	1,360	1,332	1,443	1,242	1,373	1,379	1,394	1,375
200	1,815	1,850	1,804	1,833	1,793	1,898	1,660	1,837	1,835	1,851	1,874
250	2,292	2,326	2,285	2,317	2,268	2,363	2,068	2,297	2,307	2,319	2,419
300	2,773	2,811	2,769	2,807	2,751	2,830	2,462	2,744	2,787	2,787	3,007
320	2,964	3,002	2,960	3,001	2,946	3,015	2,612	2,913	2,978	2,972	3,253
340	3,157	3,199	3,152	3,201	3,145	3,198	2,730	3,079	3,175	3,158	3,558
360	3,369	3,418	3,351	3,430	3,389	3,373	2,683	3,195	3,435	3,331	4,255
363*	3,401	3,451	3,381	3,464	3,426	3,399	2,676	3,212	3,474	3,357	4,360

\*LINEARLY EXTRAPOLATED TO FAILURE LOAD

**Table 21**  
**Strain Gage Readings for Panel B2**

LOAD (KIPS)	STRAIN GAGE READING ( $-\mu\text{IN./IN.}$ )											
	1	2	3	4	5	6	7	8	9	10	11	12
0	-1	3	3	-2	-1	-2	-1	0	-1	-2	-3	0
100	839	870	806	878	879	960	898	935	973	1,041	862	941
200	1,758	1,812	1,740	1,874	1,906	1,934	1,874	1,935	1,919	2,065	1,836	1,911
300	2,635	2,724	2,633	2,831	2,947	2,891	2,825	2,893	2,849	3,068	2,803	2,853
350	3,094	3,205	3,094	3,340	3,478	3,405	3,327	3,388	3,333	3,593	3,327	3,346
400	3,550	3,686	3,540	3,853	3,999	3,926	3,831	3,878	3,817	4,120	3,859	3,833
432*	3,842	3,994	3,825	4,181	4,332	4,259	4,154	4,192	4,127	4,457	4,199	4,145

\*LINEARLY EXTRAPOLATED TO FAILURE LOAD

**Table 22**  
**Strain Gage Readings for Panel C1'**

LOAD (KIPS)	STRAIN GAGE READING ( $-\mu\text{IN./IN.}$ )											
	1	2	3	4	5	6	7	8	9	10	11	12
0	3	4	3	3	2	2	3	2	3	0	0	1
50	505	574	521	537	523	612	451	494	549	562	554	581
100	980	1,069	1,025	1,036	1,020	1,107	913	961	1,041	1,071	1,048	1,093
150	1,461	1,581	1,547	1,550	1,537	1,623	1,398	1,453	1,561	1,613	1,577	1,650
200	1,962	2,102	2,077	2,074	2,062	2,150	1,891	1,950	2,090	2,174	2,124	2,246
250	2,459	2,634	2,608	2,603	2,593	2,675	2,353	2,442	2,623	2,729	2,729	2,883
275*	2,708	2,900	2,874	2,868	2,859	2,938	2,584	2,688	2,890	3,007	3,032	3,202

\*LINEARLY EXTRAPOLATED TO FAILURE LOAD

**Table 23**  
**Strain Gage Readings for Panel C2**

LOAD (KIPS)	STRAIN GAGE READING ( $-\mu$ IN./IN.)											
	1	2	3	4	5	6	7	8	9	10	11	12
0	0	5	3	3	0	-2	-3	-1	-1	-2	0	-3
50	444	475	469	472	481	537	444	496	517	545	501	521
100	947	979	994	988	997	1,027	930	1,014	1,009	1,036	1,031	1,050
150	1,434	1,476	1,507	1,489	1,498	1,499	1,404	1,519	1,491	1,521	1,552	1,576
200	1,935	1,985	2,035	2,010	2,019	1,985	1,883	2,043	1,992	2,020	2,098	2,126
250	2,433	2,495	2,562	2,526	2,539	2,471	2,357	2,564	2,489	2,519	2,653	2,692
300	2,937	3,015	3,100	3,050	3,071	2,965	2,823	3,101	3,000	3,031	3,247	3,304
320	3,139	3,224	3,317	3,261	3,285	3,161	3,005	3,321	3,210	3,234	3,501	3,571
360	3,543	3,643	3,744	3,683	3,725	3,541	3,322	3,765	3,635	3,629	4,094	4,233
370	3,647	3,753	3,852	3,797	3,849	3,633	3,376	3,883	3,753	3,730	4,306	4,468
380	3,757	3,871	3,968	3,917	3,975	3,731	3,442	4,008	3,877	3,832	4,508	4,734
390	3,859	3,980	4,070	4,030	4,095	3,816	3,480	4,123	3,991	3,924	4,747	5,003
399*	3,951	4,078	4,162	4,132	4,203	3,892	3,514	4,227	4,094	4,007	4,962	5,245

\*LINEARLY EXTRAPOLATED TO FAILURE LOAD

**Table 24**  
**Strain Gage Readings for Panel C3**

LOAD (KIPS)	STRAIN GAGE READING ( $-\mu$ IN./IN.)											
	1	2	3	4	5	6	7	8	9	10	11	12
0	1	3	4	6	3	2	-1	2	1	-1	-1	0
50	417	457	426	455	461	540	495	514	531	547	506	517
100	953	997	969	1,021	1,001	1,061	1,035	1,057	1,044	1,060	1,092	1,050
150	1,444	1,494	1,462	1,541	1,500	1,536	1,535	1,556	1,520	1,544	1,648	1,546
200	1,934	1,993	1,959	2,063	2,004	2,012	2,045	2,060	2,006	2,035	2,233	2,048
250	2,433	2,507	2,465	2,597	2,522	2,501	2,569	2,577	2,507	2,543	2,860	2,567
300	2,939	3,028	2,979	3,142	3,052	2,995	3,109	3,101	3,018	3,057	3,528	3,098
340	3,339	3,443	3,383	3,575	3,481	3,386	3,540	3,513	3,423	3,466	4,099	3,519
360	3,539	3,650	3,586	3,794	3,698	3,581	3,758	3,718	3,625	3,672	4,411	3,730
400	3,940	4,078	3,999	4,243	4,158	3,978	4,215	4,135	4,041	4,095	5,118	4,169
460	4,564	4,732	4,621	4,933	4,912	4,561	4,950	4,736	4,677	4,737	6,555	4,850
480	4,773	4,954	4,827	5,173	5,222	4,746	5,227	4,912	4,888	4,950	7,283	5,084
484*	4,796	4,979	4,863	5,200	5,255	4,767	5,258	4,932	4,912	4,974	7,358	5,110

\*LINEARLY EXTRAPOLATED TO FAILURE LOAD

**Table 25**  
**Strain Gage Readings for Panel C4**

LOAD (KIPS)	STRAIN GAGE READING ( $-\mu$ IN./IN.)											
	1	2	3	4	5	6	7	8	9	10	11	12
0	0	1	4	-3	1	0	2	-3	1	-1	2	-1
50	450	581	477	565	510	612	544	491	569	527	530	565
100	939	1,099	989	1,097	1,020	1,116	1,063	1,005	1,071	1,011	1,050	1,082
150	1,427	1,641	1,510	1,647	1,543	1,627	1,600	1,526	1,596	1,493	1,579	1,622
200	1,923	2,194	2,040	2,204	2,073	2,148	2,146	2,055	2,130	1,984	2,120	2,169
300	2,094	3,312	3,105	3,322	3,134	3,195	3,244	3,107	3,196	2,963	3,203	3,268
400	3,912	4,467	4,219	4,472	4,233	4,275	4,386	4,174	4,295	3,972	4,328	4,406
500	4,950	5,657	5,407	5,637	5,365	5,380	5,573	5,240	5,417	5,008	5,492	5,579
550	5,485	6,279	6,058	6,234	5,958	5,952	6,193	5,752	5,991	5,536	6,096	6,182
600	6,034	6,931	6,811	6,859	6,565	6,534	6,799	6,177	6,568	6,057	6,692	6,777
610	6,143	7,070	6,994	7,010	6,690	6,652	6,895	6,224	6,678	6,151	6,794	6,881
620	6,265	7,223	7,217	7,198	6,817	6,773	6,953	6,233	6,789	6,242	6,877	6,967
637*	6,472	7,483	7,596	7,518	7,033	6,979	7,052	6,248	6,978	6,397	7,018	7,113

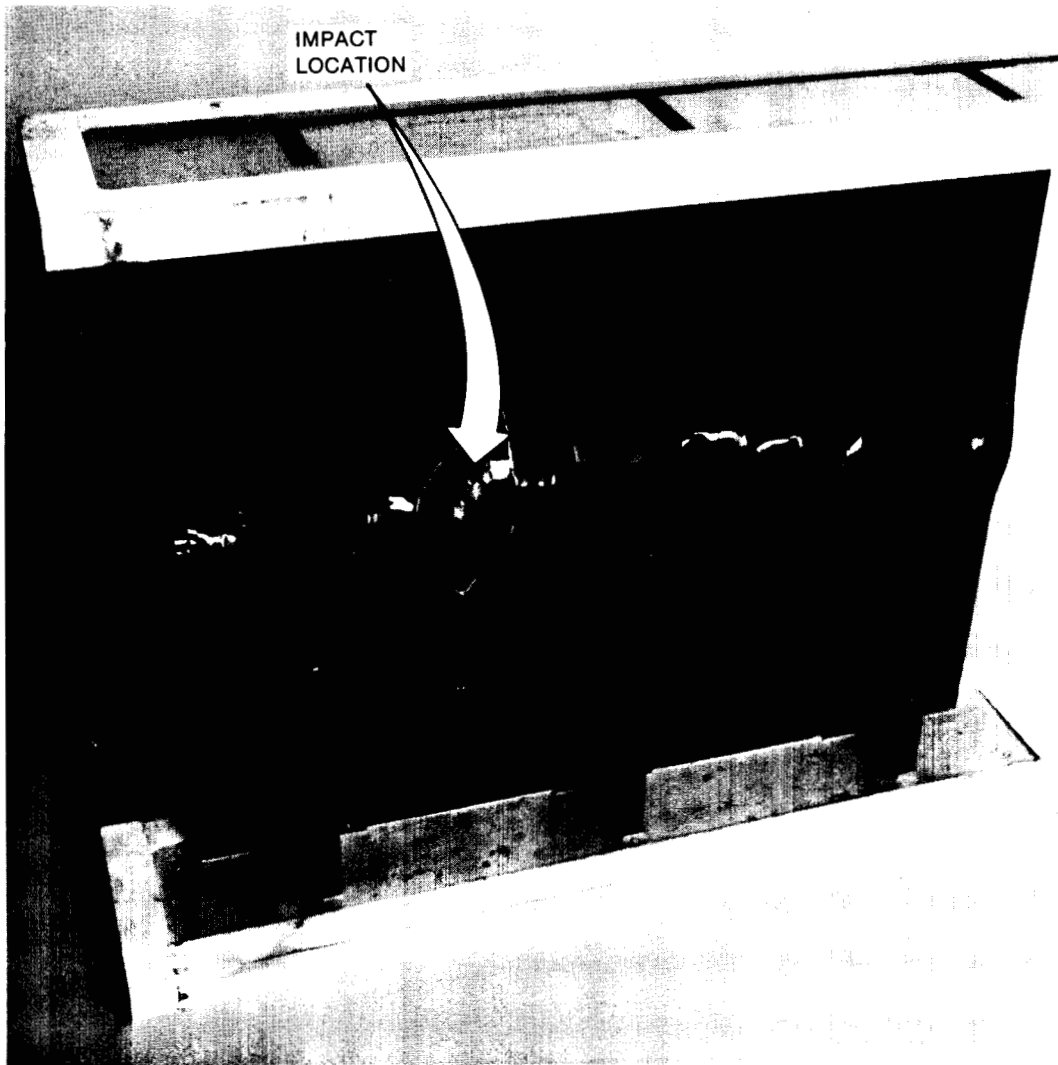
\*LINEARLY EXTRAPOLATED TO FAILURE LOAD



**Figure 52. Three-Stringer Panel B1 After Compression Test (Midbay Impact)**



ORIGINAL PAGE  
BLACK AND WHITE PHOTOGRAPH



**Figure 53. Three-Stringer Panel C1 After Compression Test (Midbay 200 ft-lb, 1/4-Inch Impactor)**

**Table 26**  
**Summary of Compression-After-Impact Test**  
**for Three-Stringer Panels**

PANEL	IMPACT LOCATION	DAMAGE LOCATION	DAMAGE SIZE	FAILURE LOAD (KIPS)	FAILURE STRESS (KSI)	GLOBAL STRAIN ( $\Delta \ell / \ell$ ) $\mu$ IN./IN.	$\Delta \epsilon - \epsilon = \epsilon_i - \epsilon_j$ ( $\mu$ IN./IN.) STRAIN DIFF
B1	MIDBAY	DISBOND AND LOCAL DELAM	4 IN. <sup>2</sup>	363	32.56 51.86 SKIN	4,333	7-8 = 536 5-6 = 9-10 = 0
B2	MIDSTRINGER	DISBOND OF SKIN-STRINGER	LENGTH OF STRINGER	432	38.69 61.71 SKIN	4,000	3-4 = 656 5-6 = 73 9-10 = 330
C1	MIDSTRINGER	NO DAMAGE		480 (NOT FAILED)	46.48	5,000	1-2 = 280 9-10 = 250 5-6 = 170
C2	MIDBAY	DELAM AND LOCAL DISBOND	2 IN. <sup>2</sup>	399	38.63	N/A	5-6 = 390 7-8 = 700 11-12 = 280
C3	EDGE OF BLADE	DELAM AND DISBOND SKIN-STRINGER	1.5 IN. LONG	484	46.86	4,444	5-6 = 500 3-4 = 340 7-8 = 280
C4	SIDE OF BLADE	DELAM AND DISBOND SKIN-STRINGER	3.5 IN. LONG 1.5 IN. INSIDE DISBOND	637	61.68	6,888	1-2 = 1,000 7-8 = 800 5-6 = 0
C1'	MIDBAY (VISIBLE DAMAGE)	PENETRATION DELAM	4.5 IN. <sup>2</sup> DELAM	275	26.63	3,333	$\Delta$ 1-2 = 200 9-10 = 120 3-4 = 0

**Panel B1** — The impact separated the skin of the panel from the stringer at the damage location. In this panel, the maximum strain occurred close to the impact-damaged location. From  $\Delta 7-8$  ( $536 \mu\text{in./in.}$ ), it can be seen that the plate failed in the flexural buckling mode. While  $\Delta 5-6$  is very small, it was observed that plate and stiffener failed separately in bending. In this case, the skin side of the panel was bent outward before failure, while the blade was bent inward, as they were no longer bonded together. Moreover, just before failure, the plate was observed to be buckled near strain gage No. 7, and the damage initiated by impact had propagated across its width. Two computed values of stress are therefore shown in Table 26, one for the skin/stringer assembly and the second for the skin only. This type of failure sequence (stiffener disbonding, skin buckling, and catastrophic failure) has been found in cases with thick (36-ply) flanges. The failure stress for the impact-damaged skin panel is given in Table 26.

**Panel B2** — As in the above panel, the impact damage separated the skin from the stringer at mid-stringer, as shown in Figure 52.  $\Delta 3-4$  shows the difference in strain at the two opposite surfaces of the skin, which indicates plate bending. Again, the small values of  $\Delta 5-6$  show that skin and stringers are bending separately and away from each other. The effect of the impact damage to the skin panel in this case was less severe than in panel B1. Figure 52 shows that the stringers did not fail with the skin. The failure strength of 61.71 ksi was computed for the skin with this type of damage.

**Panel C1** — This panel was impacted with 100 ft-lb at midstringer without any apparent damage. The panel was loaded to 480 kips and was unloaded for later investigation. Table 26 shows that the compression loading induced bending in the panel, as is obvious from the values of  $\Delta 3-4$  and  $\Delta 9-10$ . At a load of 480 kips, the panel was stressed to 46.48 ksi with a maximum strain level of  $5,289 \mu\text{in./in.}$  at the impact location.

**Panel C1'** — To demonstrate the effect of visible (front surface) impact damage on compressive strength, Panel C1' was subsequently impacted with 200 ft-lb of energy using a 1/4-inch-diameter impactor. The impact with this impactor at midbay caused the desired visible damage, penetrating into the skin.

The strain gage locations on Panel C1' were similar to those shown for Panel C2. The strain gage readings for all locations of the panel for compression tests at various load levels are summarized in Table 22. As described earlier, C-type panels failed with skin and stringer as an integral structure in compression, as shown in Figure 53. Just before failure, the panel was observed to be in a flexural mode — buckled with a mode shape characterized by a single half-wave along the length and across the width (see readings of gages No. 7, 8, 11, and 12). Then the crack propagated across the width from the initial damaged location, normal to the direction of the applied load. In general, the C-group panels' failure sequence was panel buckling followed by catastrophic failure, except for panel C4, where crippling occurred at midstringer before the panel buckled.

**Panel C2** — This panel had nonvisible impact damage. The impact produced a 2-square-inch delamination in this panel at the far surface. It failed in a flexural buckling mode at a load of 399 kips, which produced a 38.63-ksi stress and  $5,003 \mu\text{in./in.}$  maximum strain. The strain difference values of  $390 \mu\text{in./in.}$  and  $700 \mu\text{in./in.}$  at midbay (Table 26) indicate obvious bending of skin and stringer together. The crack propagated from the impact site at midbay, across the width of the panel. The damage analysis of the panel is presented in Section 5.2.2.

**Panel C3** — The impact at the edge of the flange produced a 1.5-inch-long delamination and disbond along the bond line. There was no damage in skin or blade, only in the bonding area. Although the skin and stringer were not acting together in the disbanded area, the structure failed in a flexural buckling mode similar to Panel C1'. This is verified by the values of the strain difference on the two sides at midstringer,  $\Delta 5-6 = 500 \mu\text{in./in.}$  The compression failure strength of 46.86 ksi with a maximum strain of

7,283  $\mu\text{in./in.}$  near the damaged area shows the improved damage tolerance of the panel under this impact condition.

**Panel C4** — This panel was impacted with 200 ft-lb at a 45-degree angle. The impact disbonded the stringer for a distance of 3.5 inches along the bond line and created a 1.5-square-inch delamination in the skin. The panel was compressed to a load of 637 kips, which resulted in a 61.68-ksi stress and a maximum strain of 7,223  $\mu\text{in./in.}$  A  $\Delta 1-2$  of 1,000  $\mu\text{in./in.}$  and a  $\Delta 7-8$  of 800  $\mu\text{in./in.}$  indicate a flexural behavior of the panel except at the midstringer location. At this location, skin and stringer are separated from each other, as shown by the small value of  $\Delta 5-6$ . A C-scan before impact showed a slight disbond inside the skin at the lower end, close to midstringer, which induced crippling prior to flexural buckling. Thus, the panel failure initiated with local buckling before its final failure.

### 5.2.2 Predicted Strengths

The residual stress analysis given in Section 4.4 has been employed to determine the damaged strength of stiffened panels that have been impact-tested. The criteria were based on the size of the damage through-the-thickness, lateral to the compressive loading, without taking into account the effects of velocity, weight, size, and drop distance of the impactor. The correction factor is applied in calculations where the panel was impacted with high-energy (Panel C1'). The analysis is strictly applicable for damages due to fiber breakage. The results may be erroneous if the analysis is conducted on the panels with matrix cracks and delaminations. It is assumed that the damages resulting from impact at midbay are equivalent to a sharp-edged through-the-thickness crack.

#### Case 1 — Panel B1

Since in this case the midstringer was debonded under impact damage, the stiffener distance is 14 inches.

Flange	36-Ply [(0/45/0/-45) <sub>2</sub> /90] <sub>2S</sub>	$t_f = 0.234 \text{ in.}$	$l_f = 2.4 \text{ in.}$	$A_f = 0.54 \text{ in.}^2$
Skin	Same laminate as in Case 1	$t_s = 0.34 \text{ in.}$	$l_s = 19 \text{ in.}$	$A_s = 6.41 \text{ in.}^2$
Blade	Same laminate as in Case 1	$t_b = 0.45 \text{ in.}$	$l_b = 1.77 \text{ in.}$	$A_b = 0.798 \text{ in.}^2$

where subscripts f, s, and b stand for flange, skin, and blade, respectively.

$$A_{\text{stif}} = A_b + A_f = 1.34 \text{ in.}^2 \quad R_{\text{Fly}} = 1.34/(14 \times 0.34) = 0.28$$

$$A_{\text{TOT}} = A_{\text{stif}} + A_s = 7.75 \text{ in.}^2 \text{ (assuming only one stringer is intact with skin)}$$

$$\text{From Section 4.4, } C_{\text{exp}} = 0.695$$

Lateral damage normal to compression loading,  $2c = 2.2 \text{ in.}$

$$c = 1.1 \text{ in.} \quad d_o = 0.025 \text{ in.} \quad K_T^\infty = 3.464 \quad \sigma_o = 107.03 \text{ ksi}$$

Using Equation (58),  $K_T = 3.56$

From Equation (55),  $\sigma_N/\sigma_o = 0.30$ ,  $\sigma_N = 32.1 \text{ ksi}$

Equation (65) gives  $\sigma_{cs} = \sigma_N/C_{\text{exp}} = 46.2 \text{ ksi}$

$$\text{Average strain } \epsilon_{\text{avg}} = \sigma_{cs}/E_L = 46.2/(10.07 \times 10^3) = 4,588 \mu\text{in./in.}$$

where  $E_L$  is the longitudinal modulus of the laminate.

Experimental results:

$$P = 363 \text{ kips}, \sigma_{cs} = P/A_{TOT} = 46.84 \text{ ksi.}$$

$$\text{Average strain } \epsilon_{avg} = \Delta/\ell = \frac{0.065}{15} = 4333 \mu\text{in./in.}$$

where  $\Delta$  = global displacement  $\ell$  = length of the panel

Percentage difference between analytical and experimental results in terms of  $\sigma_{cs}$

$$= (46.2 - 46.84)/46.2 = -1.3\%$$

## Case 2 — Panels C1', C2

$$\text{Flange} \quad 18\text{-ply } [(0/45/0/-45)_2/90]_S \quad t_f = 0.117 \text{ in.} \quad l_f = 2.4 \text{ in.} \quad A_f = 0.27 \text{ in.}^2$$

$$\text{Blade} \quad 72\text{-ply } [(0/45/0/-45)_2/90]_{4S} \quad t_b = 0.45 \text{ in.} \quad l_b = 1.88 \text{ in.} \quad A_b = 0.85 \text{ in.}^2$$

$$\text{Skin} \quad 54\text{-ply } [(0/45/0/-45)_2/90]_{3S} \quad t_s = 0.34 \text{ in.} \quad l_s = 19 \text{ in.} \quad A_s = 6.41 \text{ in.}^2$$

$$A_{stif} = A_f + A_b = 1.12 \text{ in.}^2 \quad A_{TOT} = 3 A_{stif} + 19 \times 0.34 = 9.77 \text{ in.}^2$$

From Equation (55)

$$R_{Fty} = 1.12/(7 \times 0.34) = 0.474$$

From Section 4.4,  $C_{exp} = 0.58$

### Panel C1'

Lateral damage normal to compression loading,  $2c = 3.7 \text{ in.}$

$$d_o = 0.025 \text{ in.} \quad c = 1.85 \text{ in.} \quad K_T^\infty = 3.464$$

Using Equation (58),  $K_T = 5.13$

$$\text{From Equation (55), } \sigma_N/\sigma_o = 0.213 \quad \sigma_o = 107.03 \text{ ksi} \quad \sigma_N = 22.8 \text{ ksi}$$

$$\text{From Equation (65), } \sigma_{cs} = \sigma_N/C_{exp} = 39.3 \text{ ksi}$$

$$\text{Average strain } \epsilon_{avg} = \sigma_{cs}/E_L = 39.3/(10.07 \times 10^3) = 3,902 \mu\text{in./in.}$$

where  $E_L$ , laminate modulus in longitudinal direction ( $10.07 \times 10^6 \text{ psi}$ )

Since the panel was impacted with 200 ft-lb of energy with a 1/4-inch-diameter impactor, it is assumed that the damage corresponds to the limit load condition with a factor of 1.5. Thus, for this panel residual strength,  $\sigma_{cs} = 39.3/1.5 = 26.2 \text{ ksi.}$

Experimental results:

$$P = 275 \text{ kips} \quad A_{TOT} = 9.77 \text{ in.}^2$$

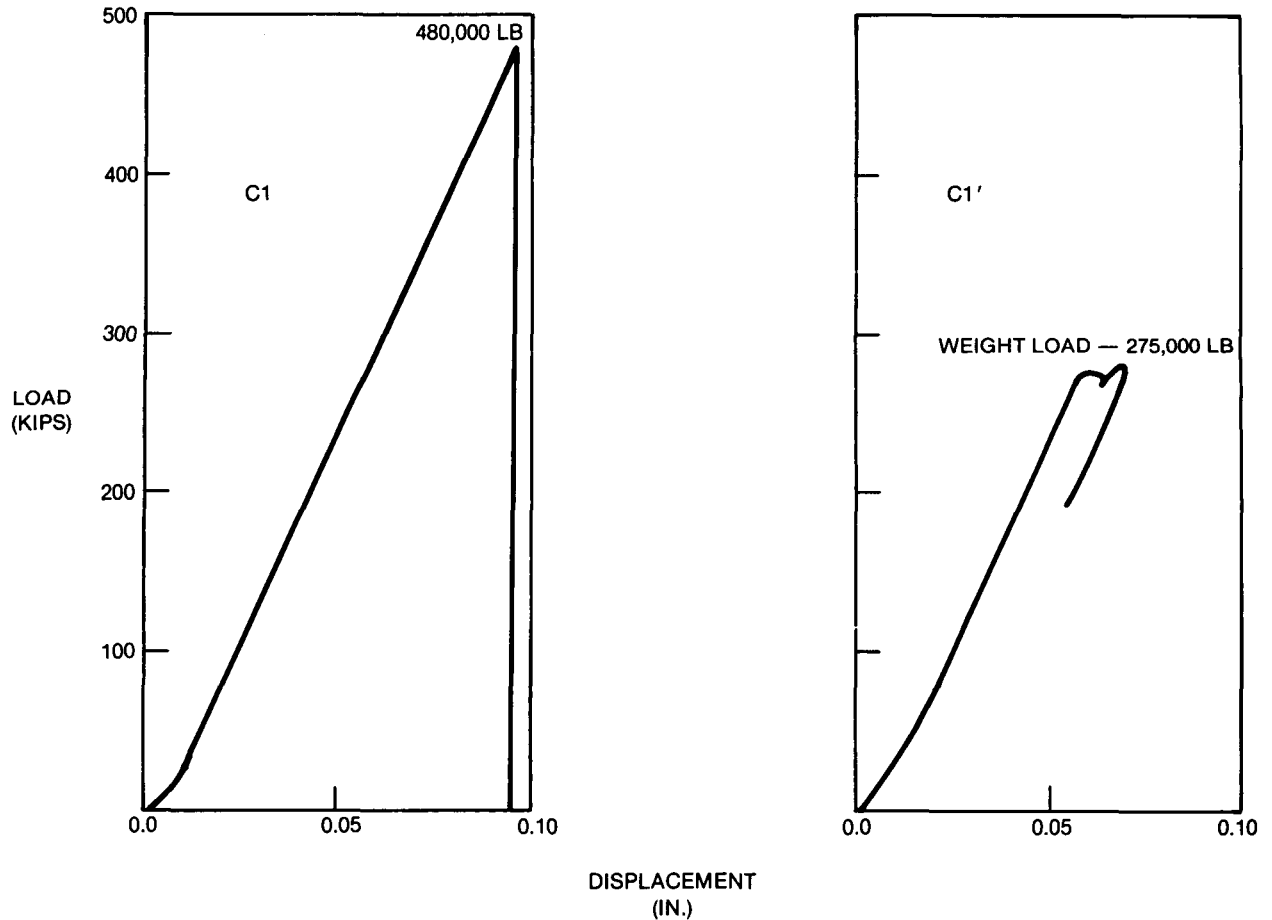
$$\sigma_{cs} = 275/9.77 = 28.15 \text{ ksi}$$

Percentage difference between analytical and experimental results in terms of  $\sigma_{cs}$

$$= (26.2 - 28.15)/26.2 = 7.4\%$$

Figure 54 shows typical load versus displacement curves for Panels C1 and C1', where  $\Delta$  is the displacement of the panel.

$$\text{Global Strain } \epsilon_{\text{avg}} = \Delta/\ell = 0.06/18 = 3,333 \mu\text{in./in.}$$



**Figure 54. Compression-After-Impact Test — Three-Stringer Panels C1 and C1'**

### Panel C2

Lateral damage size normal to compression loading,  $2c = 2.5$  in.

$$c = 1.25 \text{ in.} \quad d_o = 0.025 \text{ in.} \quad K_T^\infty = 3.464$$

Using Equation (58),  $K_T = 4.05$

From Equation (55),  $\sigma_N/\sigma_o = 0.27 \quad \sigma_N = 28.9 \text{ ksi}$

From Equation (65), the residual strength of the stiffened panels,  $\sigma_{cs}$ , is

$$\sigma_{cs} = \sigma_N / C_{exp} = 28.9 / 0.58 = 49.8 \text{ ksi}$$

$$\text{Average strain, } \epsilon_{avg} = \sigma_{cs} / E_L = 49.8 / (10.07 \times 10^3) = 4,945 \text{ } \mu\text{in./in.}$$

where  $E_L$  is longitudinal modulus of laminate.

Experimental results:

$$P = 399 \text{ kips } A_{TOT} = 9.77 \text{ in.}^2$$

$$\sigma_{cs} = 399 / 9.77 = 40.84 \text{ ksi}$$

Percentage difference between analytical and experimental results in terms of  $\sigma_{cs} = (49.8 - 44.73) / 49.8 = 10.1 \text{ percent.}$

### 5.3 DEMONSTRATION PANELS

Two five-stringer panels with 17-inch center support spans (designated D1 and D2) were fabricated as described in Section 3. These large panels were impact-damaged at Douglas and subsequently compression-tested at NASA Langley. Panel D1 had discrete source impact damage at midbay. To achieve visible damage, several trial impact tests were conducted on several undamaged parts of already impacted two-stringer panels. No NDI-detectable damage was produced when the first panel was impacted with a 1-inch-diameter impactor. The second panel was impacted with a 1/4-inch impactor, and visible damage resulted. Two aluminum ribs were fabricated from angle sections for each panel and attached to the skin with bolts at 37-inch center spans (see Figure 21). Figure 55 is a photograph of the panel that was compression-tested at NASA.

The residual strength analysis technique developed in Section 4.4 has been employed to predict the ultimate compression stress for both impact-damaged five-stringer panels. This analysis has not considered the effects of two ribs on each panel or the effect of the difference in per-ply thickness of the skin panels on mechanical properties of the material.

#### Panels D1 and D2

$$\text{Flange } 18\text{-ply } [(0/45/0/-45)_2/90]_S \quad t_f = 0.110 \text{ in. } l_f = 2.4 \text{ in. } A_f = 0.264 \text{ in.}^2$$

$$\text{Blade } 72\text{-ply } [(0/45/0/-45)_2/90]_{4S} \quad t_b = 0.438 \text{ in. } l_b = 1.89 \text{ in. } A_b = 0.828 \text{ in.}^2$$

$$\text{Skin } 54\text{-ply } [(0/45/0/-45)_2/90]_{3S} \quad t_s = 0.439 \text{ in. } l_s = 33 \text{ in. } A_s = 14.487 \text{ in.}^2$$

$$A_{stif} = t_f l_f + t_b l_b = 1.09 \text{ in.}^2 \quad R_{Fty} = 1.09 / (7 \times 0.439) = 0.355$$

$$A_{TOT} = 5 A_{stif} + A_s = 20.16$$

From Section 4.4  $C_{exp} = 0.62$

#### Panel D1

The panel showed no apparent damage. A lateral damage normal to compression loading (assumed),  $2c = 0.8 \text{ in.}$

$$d_o = 0.025, \quad K_T^\infty = 3.464, \text{ and } \sigma_o = 107.03 \text{ ksi}$$

ORIGINAL PAGE  
BLACK AND WHITE PHOTOGRAPH

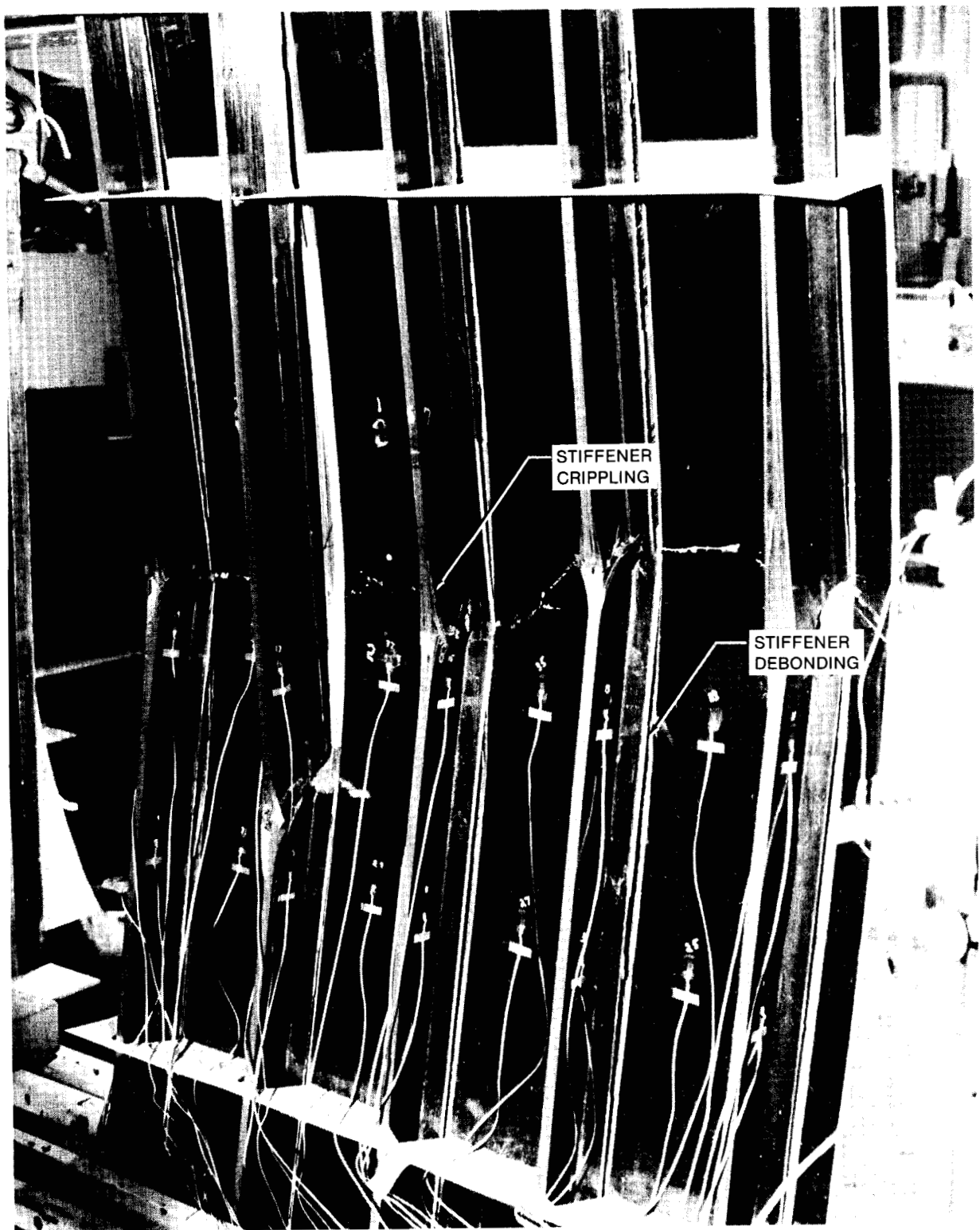


Figure 55. Five-Stringer Panel 5D-1 Compression-After-Impact Test



Using Equation (58),  $K_T = 3.51$

From Equation (55),  $\sigma_N/\sigma_o = 0.353$  and  $\sigma_N = 37.78$  ksi

Equation (65),  $\sigma_{cs} = \sigma_N/C_{exp} = 60.93$  ksi

Average strain  $\epsilon_{avg} = \sigma_{cs}/E_L = 5,695 \mu\text{in.}/\text{in.}$

where  $E_L$  is longitudinal modulus of the laminate ( $10.07 \times 10^6$  psi)

Experimental results:

It is assumed that three stringers were disbonded at the time of panel failure. The failure compressive stress,  $\sigma_{cs} = P/(A_{TOT} - 3 A_{stif})$  where  $P = 741$  kips.

$$\sigma_{cs} = 741/16.89 = 43.87 \text{ ksi}$$

$$\epsilon_{avg} = \Delta/\ell = 0.23/56 = 4,100 \mu\text{in.}/\text{in.}$$

Percentage difference between analytical and experimental results in terms of  $\sigma_{cs}$

$$= (60.93 - 43.87)/60.93 = 28 \text{ percent.}$$

In this case, as mentioned earlier, there was no apparent damage on the panel due to 100 ft-lb impact at midbay. The comparison of the predicted and experimental failure stresses of the panel showed that the assumed lateral damage of 0.8 inch was very small. The impact might have caused matrix crack damage near the skin/stringer bond line, which resulted in low residual strength. Moreover, the residual strength analysis is not accurate for small damages in the panel.

## Panel D2

Lateral damage normal to compression loading,  $2c = 2.5$  in.

$$d_o = 0.025 \text{ in.} \quad K_T^\infty = 3.464 \quad \sigma_o = 107.03 \text{ ksi}$$

Using Equation (58),  $K_T = 4.05$

From Equation (55),  $\sigma_N/\sigma_o = 0.272$   $\sigma_N = 28.9$  ksi

Equation (65),  $\sigma_{cs} = \sigma_N/C_{exp} = 47.07$  ksi

Average strain  $\epsilon_{avg} = \sigma_{cs}/E_L = 4,674 \mu\text{in.}/\text{in.}$

where  $E_L$  is longitudinal modulus of the laminate ( $10.07 \times 10^6$  psi).

Experimental results:

It is assumed that only two stiffeners were effective at the time of panel failure as the stiffeners were disbonded before failure. The compressive failure stress,  $\sigma_{cs}$

$$= P/(A_{TOT} - 3A_{stif})$$

where P is the failure compression load (755 kips)

$$\sigma_{cs} = 755 / (20.16 - 3 \times 1.09) = 44.7 \text{ ksi}$$

$$\epsilon_{avg} = \Delta / \ell = \frac{0.238}{56} = 4,240 \text{ } \mu\text{in./in.}$$

Percentage difference of failure stress from analytical and experimental results

$$= (47.07 - 44.7) / 47.07 = 5\%$$

Of the damages predicted, the poor correlation is with the midbay impact, Panels C2 and D1. The damage in these cases is much less representative of a through-the-skin crack than the other damage, which involves broken fibers. However, analysis approaches that model the damage as a circular cutout yield unconservative results with even greater error. The method proposed here is accurate for damage that results in broken fibers, and conservative for nonvisible damage that only involves matrix damage.

A summary of all of the above results is given in Table 27.

**Table 27**  
**Residual Strength Analysis**

PANEL ID	LATERAL DAMAGE SIZE IN.	$R_{Fly}$	$K_T$	$\sigma_N / \sigma_0$	$C_{exp}$	$\sigma_{cs}$ (KSI)	$\epsilon_{AVG}$ ( $\mu\text{IN./IN.}$ )	
							ANALYSIS	TEST
3-B1	2.2	0.28	3.56	0.30	0.695	46.2	4,588	4,333
3-C1'	3.7	0.474	5.13	0.213	0.58	39.3	3,902	3,333
3-C2	2.5	0.474	4.05	0.27	0.58	49.8	4,945	N/A
5-D1	0.80	0.355	3.51	0.353	0.62	60.93	5,695	4,100
5-D2	2.50	0.355	4.05	0.27	0.62	47.07	4,674	4,240

## **SECTION 6**

### **CONCLUSIONS**

The objective of the Composite Transport Wing Technology Development program was to design, fabricate, and test composite panels representative of commercial transport aircraft wing cover panels and capable of meeting all strength, aeroelastic, and damage tolerance requirements at the lowest possible cost.

The design goals were accomplished by adopting the load intensity, stiffness, and damage tolerance requirements of an in-house technology-driver development aircraft as a baseline. A cover panel configuration was evolved that satisfied the aeroelastic requirements through the use of a high-modules "hard skin" approach. The damage tolerance and durability criteria were satisfied through the use of a unique combination of high-strength, high-modulus carbon fibers and a two-phase matrix material, which effectively controlled the amount of damage resulting from foreign object damage, while retaining excellent postdamage strength. The synergistic interaction of the aeroelastic requirement for high torsional and extensional stiffness in the covers, combined with the loading intensities and geometry of the substructure, led to a design that made use of simple compact prismatic reinforcing elements adhesively bonded to a homogeneous skin panel. This configuration was judged to be the most producible arrangement possible with existing composite fabrication techniques capable of exploiting the benefits of automated tape lay-up for large skin panels, pultrusion for constant section stiffeners, and the manual labor cost of adhesively bonded assemblies.

Test panels were manufactured using conventional fabrication methods to minimize tooling costs, and excellent part quality was achieved.

Preliminary tests to determine the susceptibility of the design to impact damage revealed the existence of complex peeling failure modes in the baseline design. Analysis tools were developed that allowed an understanding of the basic failure mechanism. This in turn led to a simple redesign of the structure, which eliminated the peeling defect sensitivity without compromising the producibility of the design.

Panel compression tests performed on three- and five-stringer damaged specimens demonstrated that the design configuration met the damage tolerance requirements. Analysis methods were developed to allow prediction of the postdamage strength of the panels. These methods gave good correlation for the most critical types of damage (broken fibers) and conservative results for less critical damage cases.

The program thus accomplished all of its major goals in demonstrating a practical, low-cost, structurally acceptable composite wing cover panel concept for commercial aircraft usage.

## ACKNOWLEDGMENT

The work described in this report was supported by NASA under contract NAS1-17970. The authors wish to thank Dr. Mark J. Shuart, the technical program manager of this project, Dr. John G. Davis, Jr., and the technical staff at NASA-LRC for their cooperation and support throughout the program.

## REFERENCES

1. Standard Tests for Toughened Resin Composites, NASA Reference Publication 1092, July 1983.
2. McCarty, J., and Whitehead, R. C., Damage Tolerance of Composites, AFWAL Contract F33615-82-C3213, 5th Interim Report for the Period September 1984 to February 1985.
3. Roark, R. J., Formulas for Stress and Strain, McGraw Hill Book Company, fourth edition, New York, 1954 (Chapter 15).
4. Hart-Smith, L. J., Induced Peel Stresses in Adhesive-Bonded Joints, McDonnell Douglas Report MDC J9422A, August 1982.
5. Barkey, D., Madan, R. C., and Sutton, J. O., Analytical Approach to Peel Stresses in Bonded Composite Stiffened Panels, Douglas Paper 7907, 1987.
6. Dickson, J. N., Biggers, S. B., and Starnes, J. H., Stiffener Attachment Concepts for Graphite-Epoxy Panels Designed for Postbuckling Strength, presented at the Seventh DoD/NASA Conference on Fibrous Composites in Structural Design, Denver, 1985.
7. Madan, R. C., Walker, K. A., Hanson, B. A., and Murphy, M. F., Impact Damage Analysis for Composite Multistringer Bonded Panels, Douglas Paper 7908, presented to 3rd Annual ASM/ESD Advanced Composites Conference/Exhibition, Detroit, Michigan, September 1987.
8. Wang, J.T.S., and Biggers, S. B., Skin/Stiffener Interface Stresses in Composite Stiffened Panels, NASA CR-172261, January 1984.
9. Lekhnitskii, S. G., Anisotropic Plates, translated from the second Russian Edition by S. W. Tsai and T. Cheron, Gordon and Breach, Science Publishers, Inc., New York, 1968.
10. Barkey, D. A., and Madan, R. C., Manual for Program PSTRESS: Peel Stress Computation, NASA CR-178408, Contract NAS1-17970, December 1987.
11. Nuismer, R. J., and Whitney, J. M., Uniaxial Failure of Composite Laminates Containing Stress Concentration, Fracture Mechanics of Composites, ASTM STP593, 1975, pp 117-142.
12. Nuismer, R. J., and Labor, J. D., Application of the Average Stress Failure Criterion Part II — Compression, Journal of Composite Materials, Volume 13, 1979, pp 49-60.
13. Whitney, J. M., and Nuismer, R. J., Stress Fracture Criteria for Laminated Composites Containing Stress Concentrations, Journal of Composite Materials, Vol. 8, July 1974, p 253.
14. Madan, R. C., Crack-Arrestment in Composite Panels State-of-the-Art Review, Douglas Aircraft Company, Report MDC J3787, September 1985.
15. Avery, J. G., Design Manual for Impact Damage-Tolerant Aircraft Structure, AGARD-AG-238 North Atlantic Treaty Organization, October 1981.
16. Avery, J. G., and Porter, T. R., Survivable Combat Aircraft Structure Design Criteria and Guidelines, Final Report, Contract AFFDL-TR-74-49, 1974.

PRECEDING PAGE BLANK NOT FILMED

## Report Documentation Page

1. Report No.  NASA CR 178409		2. Government Accession No.		3. Recipient's Catalog No.	
4. Title and Subtitle  Composite Transport Wing Technology Development				5. Report Date  February 1988	
				6. Performing Organization Code	
7. Author(s)  Dr. Ram C. Madan				8. Performing Organization Report No.	
				10. Work Unit No.	
9. Performing Organization Name and Address  Douglas Aircraft Company McDonnell Douglas Corporation 3855 Lakewood Blvd Long Beach, California 90846				11. Contract or Grant No.  NAS1-17970	
				13. Type of Report and Period Covered	
12. Sponsoring Agency Name and Address  National Aeronautics and Space Administration Langley Research Center Hampton, Virginia 23665-5225				14. Sponsoring Agency Code	
15. Supplementary Notes  Langley Technical Monitor: Dr. Mark J. Shuart  Final Report					
16. Abstract  This report deals with design, fabrication, testing, and analysis of stiffened wing cover panels to assess damage tolerance criteria. The damage tolerance improvements were demonstrated in a test program using full-sized cover panel subcomponents. The panels utilized a "hard" skin concept with identical laminates of 44-percent 0-degree, 44-percent $\pm 45$ -degree, and 12-percent 90-degree plies in the skins and stiffeners. The panel skins were impacted at midbay between the stiffeners, directly over the stiffener, and over the stiffener flange edge. The stiffener blades were impacted laterally. Impact energy levels of 100 ft-lb and 200 ft-lb were used. NASTRAN finite-element analyses were performed to simulate the nonvisible damage that was detected in the panels by nondestructive inspection. A closed-form solution for generalized loading was developed to evaluate the peel stresses in the bonded structure. Two-dimensional delamination growth analysis was developed using the principle of minimum potential energy in terms of closed-form solution for critical strain. An analysis was conducted to determine the residual compressive stress in the panels after impact damage, and the analytical predictions were verified by compression testing of the damaged panels.					
17. Key Words (Suggested by Author(s))  Damage tolerance, aeroelastic tailoring, residual strength, blade-stiffened bonded panel, delamination, peel stress				18. Distribution Statement  Unclassified - Unlimited	
19. Security Classif. (of this report)  Unclassified		20. Security Classif. (of this page)  Unclassified		21. No. of pages  92	
				22. Price	